Rubidium fluoride post deposition treatment of CIGS for perovskite-CIGS tandem applications

J.C. Cortes Chitiva

RUBIDIUM FLUORIDE POST DEPOSITION TREATMENT OF CIGS FOR PEROVSKITE-CIGS TANDEM APPLICATIONS

by

Juan Camilo Cortes Chitiva

to obtain the degree of MSc in Sustainable Energy Technology
at the Delft University of Technology,
to be defended publicly on Thursday November 18, 2021 at 02:00 PM.

Student number:	5116163	
Project duration:	March 1, 2021 – November 18, 2021	
Thesis committee:	Prof. dr. ir. O. Isabella,	TU Delft, supervisor
	Dr. I. Buijnsters,	TU Delft
	Dr. M. Simor,	TNO partner in Solliance
	MSc. M. van der Vleuten,	TNO partner in Solliance

An electronic version of this thesis is available at http://repository.tudelft.nl/.

TU Delft Delft University of Technology

TNO innovation for life

SOLAR RESEARCH SOLLIANCE

If you can't explain it to a six year old,
you don't understand it yourself.

Albert Einstein

CONTENTS

Summary v

1 Introduction 1
- 1.1 Research objectives . . . 2
- 1.2 Outline of the project . . . 3
- References . . . 4

2 Literature Review 5
- 2.1 CIGS solar cells . . . 6
  - 2.1.1 State of the art high efficient CIGS solar cells . . . 7
  - 2.1.2 Gallium grading and band-gap . . . 10
  - 2.1.3 Alkali post deposition treatments (PDT) . . . 14
  - 2.1.4 Importance of different variables for PDT solar cells . . . 20
- 2.2 Perovskite solar cells . . . 27
- 2.3 Double junction tandem devices . . . 30
  - 2.3.1 2T perovskite-CIGS tandem devices . . . 32
  - 2.3.2 4T perovskite-CIGS tandem devices . . . 35
  - 2.3.3 State of the art high efficiency 4T and 2T tandem devices . . . 36
- References . . . 37

3 Experimental Methods 49
- 3.1 Device fabrication . . . 50
  - 3.1.1 Substrate . . . 50
  - 3.1.2 Absorber growth . . . 51
  - 3.1.3 Buffer layer . . . 52
  - 3.1.4 Front contact . . . 53
- 3.2 Device compositional characterization . . . 54
  - 3.2.1 X-ray fluorescence (XRF) . . . 54
  - 3.2.2 Glow discharge optical emission spectroscopy (GD-OES): . . . 54
  - 3.2.3 Raman spectroscopy . . . 55
- 3.3 Device electrical characterization . . . 57
  - 3.3.1 Current-Voltage measurements (I-V) . . . 57
  - 3.3.2 External quantum efficiency . . . 59
  - 3.3.3 Variable irradiance measurements (VIM) . . . 60
  - 3.3.4 Light dependence measurements . . . 61
- References . . . 63

4 RbF post deposition treatment optimization **65**
4.1 3-stage Rubidium Fluoride post deposition treatment . . . 66
4.2 Material characterization . . . 68
4.2.1 Temperature series . . . 68
4.2.2 Capping layer variation . . . 73
4.2.3 CGI variation . . . 75
4.2.4 Buffer layer variations . . . 80
4.2.5 Conclusions . . . 84
4.3 Electrical performance of the Solar cells . . . 86
4.3.1 Temperature series . . . 86
4.3.2 CGI variations . . . 95
4.3.3 Buffer layer variations . . . 98
4.3.4 Conclusions . . . 105
4.4 Schematics of the PDT . . . 105
References . . . 108

5 Conclusions **109**

6 Recommendations **113**

Acknowledgements **115**

A Previous internship results **117**

B PDT of air exposed absorbers **121**
B.1 preconditioning for air exposed absorbers . . . 121
B.1.1 Se atmosphere before starting PDT . . . 122
B.1.2 Cleaning procedure before staring PDT . . . 129
B.2 Conclusions . . . 134
References . . . 136

C Correlation between electrical parameters and material composition **137**
C.0.1 Temperature series . . . 137
C.0.2 CGI variations . . . 138
C.0.3 Buffer layer variations . . . 139

D Raman Baseline subtraction and fitting procedure **141**
D.1 Raman baseline removal . . . 141
D.2 Raman fitting procedure . . . 142

E Variable irradiance measurements data processing **145**
E.1 VIM V_{OC} loss quantification . . . 145
E.2 VIM FF slope quantification . . . 146

F Capping layer thickness **147**

G RbF deposition rate calibration **149**

H XRF maps of the different samples **151**

SUMMARY

During the last years, large improvements in the efficiency on the CIGS technology have been achieved, making them excellent candidates as bottom cells for double junction tandem devices. This improvement is a result of the implementation of post deposition treatments (PDT) using alkali-metal fluorides. These alkalies prove to enhance the performance of the solar cells by passivating defects in the bulk of the CIGS, and also allow to use of thinner buffer layers. Therefore, understanding the role of the different variables of the PDT, and finding the optimal combination of them is essential to improve the performance of the device.

In this work, the identification of the optimum combination of the most relevant variables of RbF PDT on 3-stage co-evaporation low band-gap (1.00-1.01 eV) CIGS absorbers is performed by carefully examining the impact of the preselected variables such as substrate temperature, material flux, and stage duration on the performance of the solar cell. Similarly, an optimization of the buffer layer is conducted to enable proper deposition and enhanced absorption in the NIR. To interpret the impact of the PDT variables, the different sets of samples are evaluated electronically and compositionally with multiple characterization techniques.

It was determined that the concentration of Cu present in the surface of the absorber prior starting the PDT, together with the substrate temperature plays the most important role in the effectiveness of the PDT. This is mainly due to facilitating optimally Rb absorption and diffusion. Next to this, appropriate rinsing of the excess of alkali present on the surface of the absorber must be performed before the deposition of the buffer layer, in order to prevent the formation of a detrimental photoactive barrier at the CdS/CIGS interface.

1

INTRODUCTION

THE yearly increasing energy demand presents one of the most important challenges for the future. Moreover, the implementation of technologies that are able to fulfill the demand and produce none or low CO_2 emissions is paramount to achieve a sustainable future. Therefore, technologies that use renewable resources such as sun or wind, and contribute stopping climate change are vital to shape the coming future. Some of these technologies are: solar photovoltaic (PV), wind energy or hydroelectric. Currently, solar PV contributes close to 2% of the total electricity demand, however, due to its good performance and decreasing levelized cost of electricity (LCOE) [1], solar PV is expected to become one of the leading technologies in the electricity sector and produce almost one quarter of the total electricity demand by 2050 [2].

PV technologies transform the solar radiation (photons) into electrical energy by using the well known photovoltaic effect. Essentially, the incident light strikes the solar cell which is made up of an absorber and a p-n junction. Inside the absorber, part of the incident light is absorbed and transformed into an electron-hole pair which is then separated by the p-n junction and collected in an external circuit [3]. The part of the light that can be absorbed depends on the absorber material band-gap. Generally, band-gaps of semiconductor materials used for the absorber layer are in the range from 1.00-2.50 eV. Ideally, the optimum band-gap for the AM1.5 spectrum is around 1.34 eV [4]. The maximum conversion efficiency that can be achieved is between 30-33% [5] due to multiple thermodynamic and non-absorption losses.

Currently, one of the most attractive semiconductor materials to produce solar cell absorbers is the $Cu(In,Ga)Se_2$ (CIGS). CIGS, is one of the most promising thin-film technologies, has a direct band-gap of 1.10 eV that can be modified by adjusting the Ga content. Moreover, thanks to its high absorption coefficient the total thickness of the device can be reduced to a few micrometers reducing costs and enabling flexible PV modules when deposited on flexible substrates. In the past years, the implementation of post deposition treatments (PDT) with alkali metal fluorides enables the production of solar cells with efficiencies above 20% [6], getting one step closer to the theoretical maximum limit. All of the above, in combination with the high performance at a relatively low cost,

excellent durability and low weight [7], widens the possible applications of CIGS solar cells.

Evidently, CIGS solar cells show remarkable properties and performance, but due to their low band-gap, a big part of the incident high energy photons is transformed in both electricity and heat. According to the Shockley-Queisser limit (SQL), almost 70% of the energy coming from high energy photons is lost into heat [4]. One way to overcome this issue is the implementation of tandem devices in which a higher band-gap absorber material is stacked on top of the low band-gap one. Thus, the top sub-cell absorbs these high energy photons, and the bottom one the low energy ones. By implementing these types of technologies the theoretical maximum conversion efficiency that can be achieved is up to 46% for double junction and 52% for triple junction devices [8].

Depending on the type of tandem architecture, 2-terminal (2T) or 4-terminal (4T), there is an optimum combination of band-gaps for both sub-cells. Considering that the top sub-cell has the largest impact on the total efficiency of the device, the band-gap of the top sub-cell defines the bottom one. Generally, double junction devices are built using perovskite and CIGS absorbers first thanks to the possibility to modify the band-gap of both of them. On one hand, perovskite materials can be tuned between 1.50 and 2.50 eV, while CIGS can be modified to obtain band-gaps between 1.00-1.70 eV. Multiple studies show that for double junction tandem devices to produce the highest conversion efficiency, the band-gaps should be of 1.60 eV and 1.00 eV for the perovskite and CIGS respectively [9].

As perovskite materials are easy to process and are inexpensive [10]. Perovskite-CIGS devices with the expected high performance and relatively easy and cheap processing are potential candidates for future high performance thin film photovoltaic devices.

It is important to remark that to achieve this, the performance of both (bottom and top) sub-cells must be optimal. Consequently, the optimization of PDT for the CIGS bottom cell plays a key role in obtaining a high efficiency device capable of producing good electrical and surface characteristics, enabling a suitable coupling with a perovskite top sub-cell to create an ideal perovskite-CIGS tandem device.

1.1. RESEARCH OBJECTIVES

THE need for highly efficient technologies for energy production is one of the most important goals for the future. PV technologies have shown the potential to achieve this goal by improving its efficiency in developing new materials and processes.

The project has focused on the optimization of rubidium fluoride (RbF) post deposition treatment (PDT) of CIGS solar cells. RbF PTD was expected to boost the electrical performance of both open circuit voltage (V_{OC}) and fill factor (FF), intended for perovskite-CIGS tandem applications. In the fabrication of a tandem device, for its high performance, the optimum band-gaps of both sub-cells need to be taken into consideration. The band-gap of the bottom CIGS cell should be in a range of 1.00-1.10 eV with an anticipated band-gap of the top perovskite cell of 1.60-1.70 eV.

Through optimization of RbF PDT, coupled with a band-gap tuning of CIGS solar cells for the mentioned lower band-gap (compared to the band-gap of single junction CIGS devices) and front window (CdS + TCO) optimization, a high response in the NIR region shall be acquired. The project has been an inherent part of TNO's activities within

SOLAR-ERA.NET project SUCCESS and H2020 project PERCISTAND, both being in their second year during this project.

To be able to optimize the RbF PDT on low band-gap devices two different questions need to be addressed:

- What are the most important parameters related to RbF PDT process?
- What is the role of these parameters on achieving optimal material properties resulting in high performance?

1.2. OUTLINE OF THE PROJECT

The optimization of RbF PDT for low band-gap CIGS absorbers to be used in double junction perovskite-CIGS tandem devices is presented in this report by modifying experimentally the different variables used to perform the PDT and analyzing the impact on material properties and electrical performance. In Chapter 2, the state of the art of CIGS and perovskite devices is presented, as well as the essential aspects of PDT. Next, Chapter 3 first describes the process of fabrication of the CIGS absorber as well as the additional layers used to finalize the solar cell. In the second part, the characterization techniques used to evaluate the electrical performance and material properties of the solar cells are explained. Then, Chapter 4 explains in detail the different stages of the PDT and shows the results obtained for the different set of experiments performed. Finally, Chapter 5 and 6 the final conclusions and recommendations are presented respectively, together with the combination of variables for the PDT that result in the best electrically performing sample.

1

REFERENCES

[1] E. I. Administration, *Levelized costs of new generation resources in the annual energy outlook 2021,* .

[2] I. R. E. Agency, *Future of solar photovoltaic - irena,* .

[3] *Chapter 7 - high efficiency plants and building integrated renewable energy systems,* in *Handbook of Energy Efficiency in Buildings*, edited by F. Asdrubali and U. Desideri (Butterworth-Heinemann, 2019) pp. 441–595.

[4] A. Smets, K. Jäger, O. Isabella, R. van Swaaij, and M. Zeman, *Solar Energy: The Physics and Engineering of Photovoltaic Conversion, Technologies and Systems* (UIT Cambridge, 2016).

[5] S. Rühle, *Tabulated values of the shockley–queisser limit for single junction solar cells,* Solar Energy **130**, 139 (2016).

[6] M. Nakamura, K. Yamaguchi, Y. Kimoto, Y. Yasaki, T. Kato, and H. Sugimoto, *Cd-free Cu(In,Ga)(Se,S)$_2$ thin-film solar cell with record efficiency of 23.35%,* IEEE Journal of Photovoltaics **9**, 1863–1867 (2019).

[7] M. W. Bouabdelli, F. Rogti, M. Maache, and A. Rabehi, *Performance enhancement of CIGS thin-film solar cell,* Optik **216**, 164948 (2020).

[8] A. D. Vos, *Detailed balance limit of the efficiency of tandem solar cells,* Journal of Physics D: Applied Physics **13**, 839 (1980).

[9] W. Shockley and H. J. Queisser, *Detailed balance limit of efficiency of p-n junction solar cells,* Journal of Applied Physics **32**, 510 (1961), https://doi.org/10.1063/1.1736034 .

[10] D. N. Weiss, *Tandem solar cells beyond perovskite-silicon,* Joule **5**, 2247 (2021).

2

LITERATURE REVIEW

In this chapter, the current status of two of the most important photovoltaic technologies is presented. First, in Section 2.1 thin film CIGS solar cells are described, along with the importance of Gallium grading to obtain low band-gap solar cells that can be used in tandem devices. The implementation of post depositions treatments with alkali metal fluorides in the past years has resulted in improvements in CIGS PV module efficiencies and new world records for CIGS have been obtained. Therefore the key aspects and elements that can be used to perform them are discussed and reviewed. In the next section, 2.2, an overview of perovskite solar cells structure, electrical properties, architectures, manufacturing techniques, and common issues (like degradation) are shown. Next, Section 2.3, two cell tandem devices are described and explained, with the different configurations that can be used (two terminal and four terminal), the important characteristics of the multiple layers that compose them, and the current status of the electrical performance of perovskite-CIGS tandem devices is reviewed.

2.1. CIGS SOLAR CELLS

As mentioned before, one of the trending PV technologies used nowadays is the thin film one. One of the most important thin film technologies is the Cu(In,Ga)Se_2 (CIGS) one. This kind of technology can be produced using multiple deposition processes such as, co-evaporation or selenization followed by sulfurization of precursors which can be deposited by printing, electrodeposition, or sputtering. Figure 2.1 shows the two most used production techniques to manufacture CIGS. While most of the time co-evaporation is used for lab scale solar cells, sputtering selenization or selenization and/or sulfurization on precursors already containing Cu, Ga, and In at high temperatures is performed. The last two are often used to process large scale module size devices.

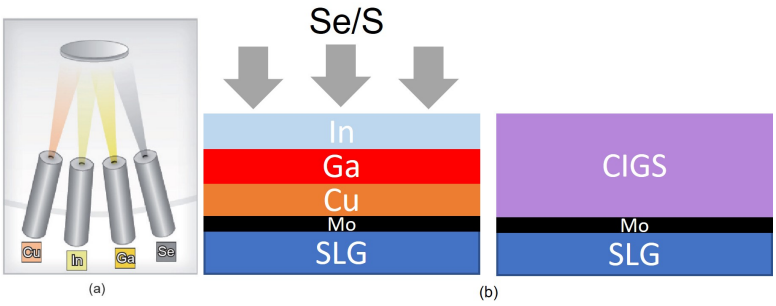

Figure 2.1: Comparison of the deposition techniques. **a.** Co-evaporation. Adapted from [1], **b.** Selenization/-sulfurization on precursors wiht Cu, In and Ga.

The device structure can be seen in Figure 2.2. First, the type of substrate needs to be chosen, usually, two of the most common substrates that can be used are, soda lime glass (SLG) and polymeric films (PI). However, metal foils such as steel or ceramics materials can also be used. On top, the substrate is covered first by a conductive Molybdenum layer, which is used as the back contact electrode. This layer is generally sputtered into the substrate. Then, the p-type absorber deposition takes place using one of the previously mentioned methods. Following the absorber deposition, an n-type buffer layer is used. Similar to the substrate, there are different materials that can be used for this layer. Some of them are CdS or a combination of Zn(O,S,OH), although CdS is the most used one due to its relatively low band-gap. This buffer layer is commonly deposited by chemical bath deposition (CBD). The last three steps consist of the deposition of the second buffer layer generally i-ZnO mainly to prevent current leakage in case of local inhomogeneities or incomplete CdS buffer coverage, [2] [3], next the transparent conductive oxide (TCO) is used as the front contact which is commonly made out of aluminum doped ZnO and finally the grids are deposited generally made out of copper.

Currently, there are different techniques that can be used in order to boost the performance of CIGS absorber layer. Some of the most used ones are, post deposition treatments (PDT) with alkali metal fluorides mainly used to passivate defects, band-gap tuning introduced with different Ga grading profiles in order to absorb more light or creation of tandem devices, with double junction cells like perovskites (discussed in more

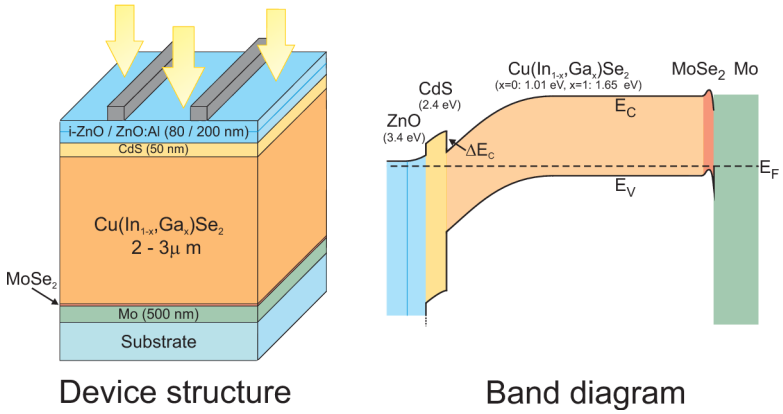

Figure 2.2: **Left**, Cross section of CIGS device structure with the different layers. **Right**, Schematic CIGS energy band diagram at forward bias. Adapted from [4].

detail in the next sections). Other techniques such as the use of anti-reflective coating or scribe-less cells can be implemented in order to increase light absorption.

2.1.1. STATE OF THE ART HIGH EFFICIENT CIGS SOLAR CELLS

As it can be seen in Figure 2.3, the conversion efficiency of CIGS solar cells has been in constant improvement throughout the years. However, from 2014 onwards the introduction of alkali metal fluorides from PDT into the CIGS solar cells made it possible to achieve efficiencies above 20% [5]. Table 2.1 present a short compilation of the best efficiencies achieved with PDT treated CIGS solar cells.

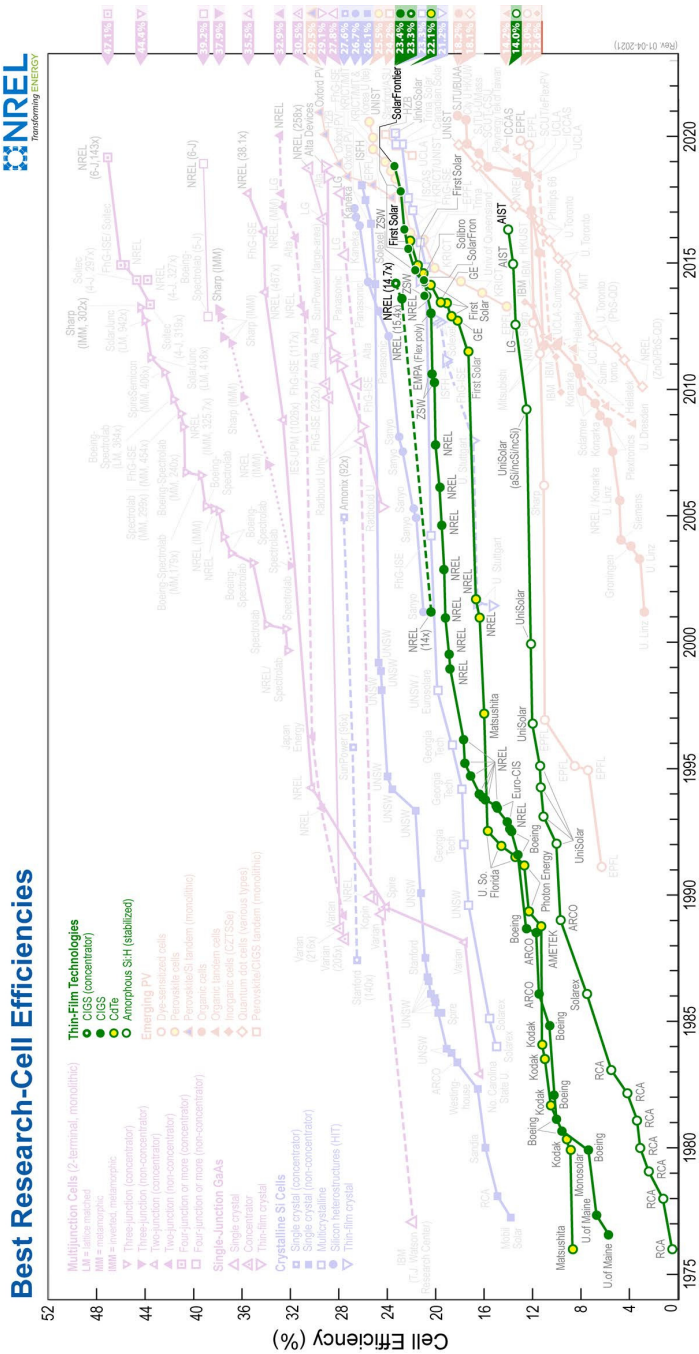

Figure 2.3: Best research thin film cell efficiencies. Adapted from [6].

Table 2.1: Different combination of PDT's and its solar cell parameters.

Reference	Company	Year	Author	Production method	Substrate	Substrate Preparation
[7]	Solar Frontier	2019	Motoshi Nakamura	Sputtering Selenization	Glass	Mo sputtered and CuGa/In with Na additive
[8]	Solar Frontier	2018	Takuya Kato	Sputtering Selenization	Glass	Mo sputtered
[9]	ZSW	2016	Philip Jackson	Co-evap	Alkali-aluminosilicate glass no Na diffusion barrier	Cleaned and sputtered Mo (500-900 nm)
[10]	ZSW	2016	-	Co-evap	-	-
[5]	ZSW	2014	Philip Jackson	Co-evap	SLG no Na Barrier	Cleaned and sputtered Mo (500-900 nm)
[11]	ZSW	2019	Mohit Raghuwanshi	Co-evap	SLG no Na Barrier	Mo-coated + alkali containing glass substrate
[12]	HZB	2019	Tim Kodalle	Co-evap	SLG no Na Barrier	-
[13]	ZSW	2014	Philip Jackson	Co-evap	SLG no Na Barrier	Mo sputtered (500-900 nm)
[14]	EMPA	2013	Adrian Chirila	Co-evap	PI film	PI film
[15]	AIST	2018	Shogo Ishizuka	Co-evap	SLG no Na Barrier	Mo-coated

Reference	Temperature of the substrate	Element(s) used in PDT	CGI	GGI	Eg [eV]	V_{OC} Deficit [mV]	V_{OC} [mV]	J_{SC} [mA/cm^2]	FF [%]	η [%]	Annealing atmosphere
[7]	350	CsF	0.93	0.3	1.08	346	734	39.6	80.4	23.35	S
[8]	-	CsF	-	-	1.13	414	746	38.5	79.7	22.92	-
[9]	350	RbF	0.88<x<0.92	0.3<x<0.33	-	-	741	37.8	80.6	22.6	Se
[10]	-	RbF	-	-	-	-	744	36.7	80.5	22	-
[5]	-	RbF	0.91	0.32	-	-	746	36.6	79.3	21.7	*Additional annealing step at a temperature much lower than for the RbF PDT
[11]	-	RbF	-	-	-	-	745	36.23	78.2	21.1	Air
[12]	530	RIS	0.95	0.24	1.08	416	687	38.4	79	20.9	-
[13]	350	KF	0.91	0.32	1.11	353	757	34.8	79.1	20.8	No anneal
[14]	350	NaF+KF	0.78<x<0.82	0.33<x<0.38	-	-	736	35.1	78.9	20.4	Se
[15]	350	RbF	0.9	0.2<x<0.3	-	-	717	36.35	77.3	20.14	Se

2.1.2. GALLIUM GRADING AND BAND-GAP

ONE of the most important aspects of thin film technology especially in CIGS, is the possibility to tune the band-gap of the device. This can be achieved by modifying the Ga content in the absorber layer which directly modifies the position of the conduction band, and devices with band-gaps ranging from 1.00 eV to 1.70 eV can be obtained by using pure $CuInSe_2$ or $CuGaSe_2$ respectively [16]. Therefore, for perovskite-CIGS tandem application, it is important to bear in mind the desired band-gap of the CIGS (bottom) sub-cell which directly depends on the band-gap of the perovskite (top) sub-cell, discussed in more detail in Section 2.3.

As previously mentioned, the band-gap of the solar cell depends on the Ga content, however it is often preferred to use the GGI eg. $GGI = [Ga]/([Ga] + [In])$ content of the absorber since it can be directly correlated with the band-gap of the solar cell. Extensive research has been done and multiple equations have been established. At the moment, the most recent one is Equation 2.1 [17] which takes into account different bowing factors and best describes the relation between band-gap and GGI concentration.

$$E_g[eV] = 1.004 \cdot (1 - GGI) + 1.663 \cdot GGI - 0.033 \cdot GGI \cdot (1 - GGI) \tag{2.1}$$

Generally, a so-called double Ga grading profile is implemented on regular 3-stage co-evaporation process as it can be seen on Figure 2.4, the profile is characterized by containing higher Ga concentration towards the front and back of the absorber, while in the middle-front part (around 0.4 and 0.5 µm) a lower content is desired. By achieving this kind of V-shaped profile, 3 important aspects have been identified. First, the position of the conduction band maximum (CBM) towards the back electrode is increased (Figure 2.7), and therefore an assisted drifting of photogenerated electrons towards the space charge region (SCR) in the p-n junction is created. Second, the absorption of low energy photons in the edge of the SCR is enhanced due to the lower band-gap obtained in the middle front part of the absorber, and finally, the steep increase of Ga in the front part of the absorber increases the band-gap and therefore the open circuit voltage. Furthermore the alignment between the CBM of the buffer layer and the absorber is enhanced [18]. In order to obtain this kind of profile, commonly the 3-stage deposition described in Figure 2.5 is followed, where In and Ga fluxes are kept the same during the first and third stages of the deposition while during the 2-stage the fluxes are stopped and there is no deposition of Ga and In.

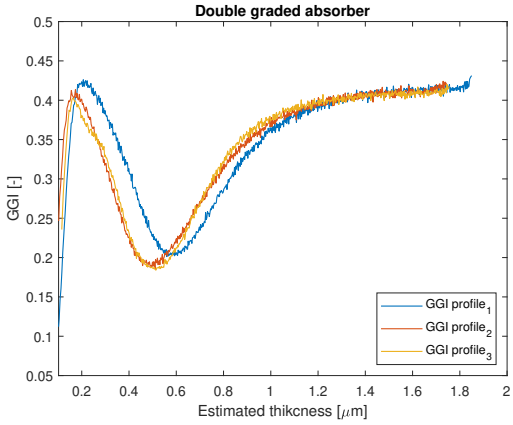

Figure 2.4: Double grading in 3-stage co-evaporation samples.

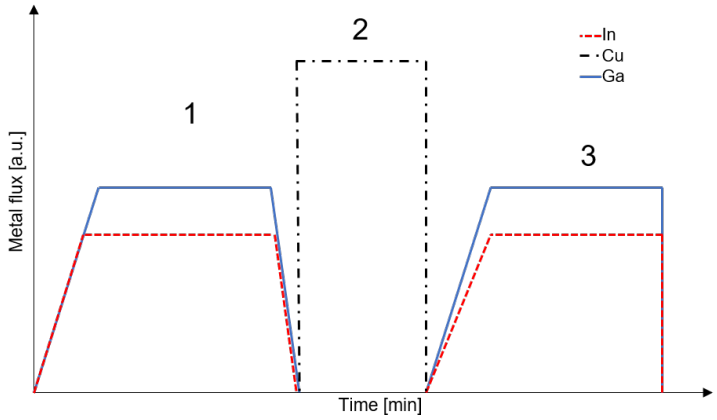

Figure 2.5: Schematic of 3-stage co-evaporation CIGS deposition. The Se pressure and flux is kept constant during all the stages.

However, most of the time double graded CIGS absorbers tend to have higher band-gaps (>1.10 eV) and therefore are not suitable for tandem devices where band-gaps close to 1.00 eV or GGI below 0.07 are needed. In order to overcome this issue, the use of single back or front (Figure 2.6) Ga grading has been studied by Feurer et al. [19]. The results showed that the use of front graded solar cells leads to lower electrical performance. Thanks to an increased extended SCR, which leads to recombination of holes that are generated in the front part of the absorber. Therefore, a lower response in the EQE for wavelengths close to the infrared region (NIR) is expected, which directly leads to a decrease in short circuit current. Moreover, the fill factor (FF) of single front graded solar cells is reduced due to the crystallization of smaller grains in the front of the solar cell.

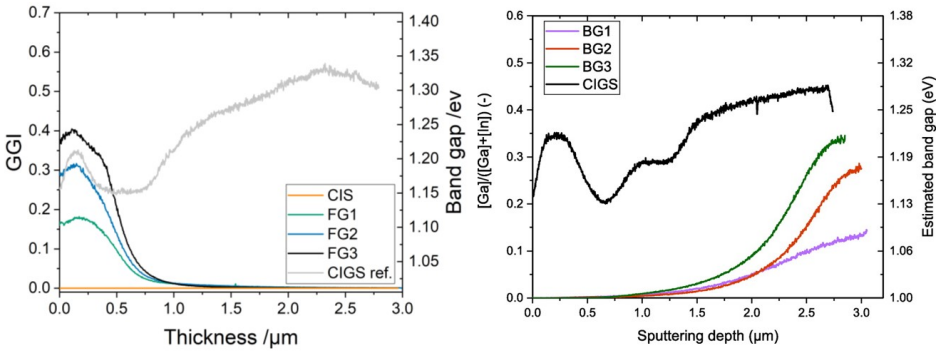

Figure 2.6: **Left**, front graded CIGS solar cell. Adapted from [19]. **Right**, back graded CIGS solar cell. Adapted from [20].

In contrast, back graded solar cells show better performance in electrical parameters by showing better response in the NIR, FF and open circuit voltage. The improved response in the NIR of back graded solar cells can be attributed to an increase in the CBM leading to an additional field for the back part photogenerated electrons towards the SCR, where they can be extracted and collected. Moreover, time resolved photoluminescence results show improved lifetimes indicating better bulk absorber quality and reduced back surface recombination leading to higher open circuit voltages [20]. To obtain this type of solar cells, generally, the profile described in Figure 2.8 is followed, where In is ramped up while Ga is ramped down during the first stage of the deposition, and after the first stage Ga flux is stopped for the 2- and 3-stage of the deposition, while In is reduced to prevent deposition during the 2-stage and then is ramped back up for the 3-stage.

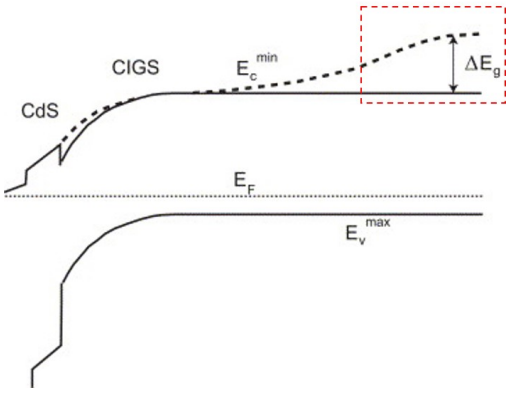

Figure 2.7: Change in the conduction band maximum (CBM) due to the effect of the Ga grading. Adapted from [21].

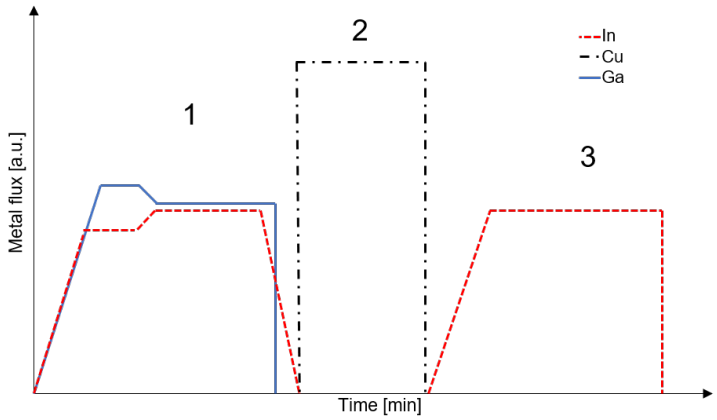

Figure 2.8: Schematic of 3-stage co-evaporation CIGS deposition implementing Ga-grading and achieving low band-gap, the Se pressure and flux is kept constant during all the stages. Notice the reduced Ga flux used and the increased In flux during the first stage and the stop of Ga deposition for the second and third stage.

Over the last years, multiple research has been done in order to elucidate the role that Ga distribution plays on the electrical performance of the device ([21]-[22]). Understand the diffusion of Ga throughout the absorber growth and its influence on other elements, such as Cu content [23], alkali metal fluorides ([24], [25]) or even the role that the substrate growth temperature [26] plays for Ga grading. Although, the presence of alkali metal fluorides hinder the In/Ga interdiffusion, in combination with higher substrate temperatures the In/Ga interdiffusion can be enhanced thereby easing the Ga grading. Consequently, Ga grading can be achieved in spite of many influencing factors [18].

2.1.3. ALKALI POST DEPOSITION TREATMENTS (PDT)

THREE different methods can be used to incorporate alkali metal fluorides into CIGS absorbers: pre-deposition, co-evaporation, and post-deposition. The first uses the alkali metal fluoride in the substrate and diffuses it into the absorber, the second one incorporates the alkali metal fluoride into the absorber while it is being deposited, and finally, PDT incorporates the alkali metal fluoride by annealing after the absorber has been deposited [27]. Among these three methods, PDT has been shown to make the biggest progress in increasing the efficiency of CIGS solar cells.

In this section, the different methods and variables to perform PDT will be discussed. First, the different alkali metal fluorides that can be used to perform PDT will be described and evaluated, after that is important to understand the diffusion of alkali metal fluorides in the CIGS layer, next to the CGI and GGI concentrations and its impact on PDT will be discussed. Section 2.1.4 discuss the different variables that can be modified during the annealing process such as time and temperature, Table 2.1 present up to date efficiencies for different PDT and its relevant variables.

ALKALI METAL FLUORIDES FOR PDT

In this section, the most important alkali metal fluorides that have been used for PDT are going to be discussed and how they impact the electrical performance of solar cells. Generally, they are divided into two different groups: light and heavy alkali metal fluorides.

1. **Light alkali metal fluorides**

    - Sodium: Na is a soft metal that has an ionic radius of 0.095 nm and weights 22.98 gr.mol^{-1} [28], is present (in abundance) in soda lime glass substrates. In early years Na was found to be beneficial by increasing the hole concentration by almost two orders of magnitude and therefore increasing solar cell V_{OC} and FF [29].
    - Potassium: After Na was discovered, another element was needed that could be used to improve the electrical properties of Na-free substrates, K weights 39.09 gr.mol^{-1} and has an ionic radius of 0.133 nm [28]. It has been shown that K has a similar impact on solar cell performance as Na by increasing V_{OC} and FF [30]. This performance enhancement is attributed to a reduction in the diode quality factor and reverse saturation current density (J_0) [9].

2. **Heavy alkali metal fluorides**

    - Rubidium: Thanks to the huge impact that K made after it was added to CIGS, Jackson et al. [9] investigated the use of heavier elements and found that Rb could potentially boost even more the electrical performance of solar cells. Rb weights 85.46 gr.mol^{-1} and it has a 0.149 nm atomic radius [28]. With the use of Rb higher η could be achieved thanks to an increase in FF and J_{SC} compared to Na and K, however, the increase in FF depends drastically on the CGI content [12] [31] (explained in 2.1.3). Generally, it boosts the electrical parameters compared to reference samples.

- Caesium: Cs is the heavier and bigger of the aforementioned elements, it weights 132.9 gr.mol^{-1} and its radius is 0.167 nm [28]. Just like Rb, Cs also show the ability to enhance the electrical properties of solar cells. It has been shown by Jackson et al. [9] that the FF and J_{SC} increase compared to Na and K nevertheless, the FF is slightly lower when compared to Rb. However, Tzu-Ying et al. [32] found that by modifying the absorber by adding band-gap grading near the front surface and applying a CsF PDT, the FF, V_{OC} and η were improved. Currently, the use of Cs-PDT along with double Zn buffer layer has generated the wolrd record efficiency of a CIGS solar cell of 23.35% [7].

DIFFUSION OF ALKALI METALS

Multiple studies have been carried out to understand the diffusion mechanism of alkali metals into the different layers of the CIGS solar cell. The diffusion is highly dependent on temperature, concentration, and grain size among others [33]. The key aspects of how this process occurs can help explain why certain elements produce the best performance solar cells.

As it has been described by Wuerz et al. [33], Chirila et al. [14] and Jackson et al. [9] the heavier the alkali metal that is introduced by the PDT in the already grown CIGS absorber, tend to push out the lighter alkalies already present in the material. This phenomenon is named ion-exchange mechanism. With the use of characterization techniques such as secondary ion mass spectroscopy (SIMS) and glow discharge optical emission spectroscopy (GD-OES) is possible to verify this. Figure 2.9 show the results of SIMS profile in which the smaller elements, in this case, sodium, are displaced by the addition of KF PDT on one hand, and on the other hand, both Na and K are displaced with the addition of CsF PDT.

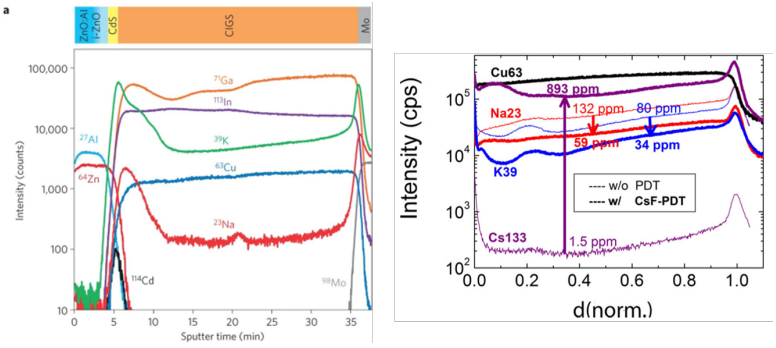

Figure 2.9: SIMS depth profile for KF and CsF PDT treated samples. Adapted from [14] and [9].

Along with the above, it is also important to understand which mechanism the different elements use to diffuse from the CIGS top layer since they can diffuse along grain boundaries (GB) or in the bulk of the grain. This was studied in deep by Wuerz et al. [33], they focused on applying an RbF PDT followed by a NaF PDT and vise versa. For each experiment, they used 2 sets of samples in which one was left Na (Rb) free and no NaF

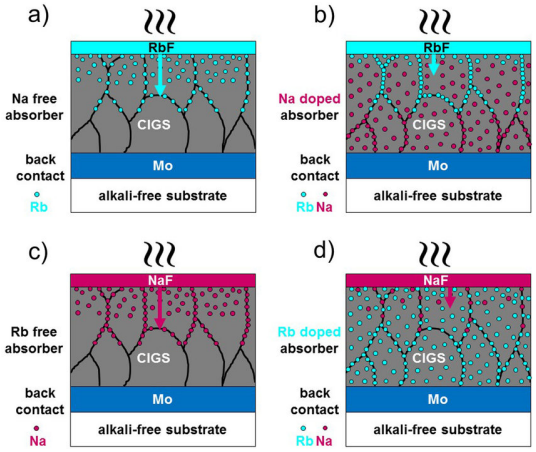

Figure 2.10: **a)** Diffusion of Rb into Na-free CIGS; here, Rb diffuses into the grain bulk as well as into GBs, **b)** diffusion of Rb into Na-doped CIGS; here, diffusion of Rb into the grain bulk is reduced and diffusion into GBs is enhanced compared to (a). In **c)**, diffusion of Na into Rb-free CIGS is shown, Na diffuses into the grain bulk as well as into the GBs; **d)** diffusion of Na into Rb-doped CIGS, where diffusion into the grain bulk is strongly hindered and diffusion into the GBs is hindered compared to (c). Adapted from [33].

PDT (RbF PDT) while the other one Na (Rb) doped by the PDT. They concluded that if Na is not present in the CIGS layer, Rb could diffuse into the GBs and into the bulk. In case Na is already present in the sample, Rb diffusion through GBs is enhanced, and into the grain, interior is hindered but still takes place. In contrast, in the other experiment, if Rb is already present in the sample, Na diffusion takes place along the GB and into the grain is strongly hindered, Figure 2.10 shows in more detail the results of the mentioned experiment.

The mechanisms of diffusion for the different alkali metals and their correlation with the solar cell electrical parameters are generally understood as follows:

1. **Light alkali metals**

   - Sodium: As mentioned before, by applying Na it is possible to increase the carrier concentration and thus increase the V_{OC} of the solar cell. Besides, since Na can diffuse through the GBs as well as inside them, it has been shown by Rudmann et al.[34] that it can help to passivate the defects present in those areas and therefore increase the V_{OC}.
   - Potassium: It has been demonstrated by Chirila et al. [14] that the KF PDT induces a chemical modification in the surface of the CIGS absorber, depleting Cu and Ga. By making this, the buffer (CdS) layer can be easily deposited with a shorter time and smaller thickness due to an enhancement in the diffusion of Cd through the CIGS. All of the above generates enhancement in J_{SC}, V_{OC} and FF. It is important to mention that K mainly diffuses through GBs and not in the grain interior [35].

2. **Heavy alkali metals**

   - Rubidium: According to Schöppe et al. [36], Rb diffuses along the GBs through the entire absorber layer and agglomerate in high angle GBs, dislocation cores and in the back contact interface. Is believed that the excellent electrical performance of RbF PDT samples is due to an increased size of the element facilitating the passivation of large size defects at GBs or dislocation cores producing higher V_{OC} and FF. In another study, Kodalle et al. [37] showed that like with KF PDT the buffer layer growth is affected. However, the RbF PDT takes longer to passivate the surface for the deposition of the buffer layer, nevertheless the J_{SC} is enhanced. Recently, other studies by Kodalle et al. [12] and Taguchi et al. [38], show that a formation of a secondary surface phase called RIS ($RbInSe_2$) by the implementation of RbF-PDT can also help to enhance the electrical properties of RbF treated solar cells. In contrast to K and Na, Rb tends to diffuse through Cu vacancies, therefore the high concentration of Rb generally produce a Cu depletion which indicates an improvement of the hole-barrier thus, a reduction in recombination and higher V_{OC} are obtained [39].
   - Caesium: Recent studies by Tzu-Ying et al. [32] revealed that Cs increase the carrier lifetime at the buffer/absorber interface and in the space charge region due to diffusion of Cs along the GBs. Consequently, a huge increase in V_{OC} and FF can be achieved. Moreover, Kato et al. [8] showed that Cs-PDT has similar results to K-PDT but higher V_{OC} can be achieved since it increases heavily the minority carrier density and lifetime by reducing the defect density. Like with Rb, high agglomeration of Cs concentration tend to be accompanied by a Cu depletion and increased In and Se concentrations, moreover the presence of Cs passivate highly disordered GBs and therefore is beneficial for solar cell electrical parameters [40].

In Table 2.2 different methods to introduce alkali metals into the CIGS layer are compared together with its highest cell efficiency. It should be noted that this table is from 2014, and therefore in Table 2.1 up to date efficiency values can be found. Notice, that the highest efficiencies can be achieved by diffusion of Na from soda lime glass (SLG) or using a bigger alkali metal fluoride for the PDT after Na diffusion.

Table 2.2: Different methods for incorporating alkali metal fluorides into the CIGS layer and efficiency achieved. Adapted from [41].

Method for incorporating alkali metal fluorides into the CIGS layer	Highest efficiency (%)
Diffusion from SLG substrate + PDT with KF	20.8*
Diffusion from Na containing Mo back electrode on borosilicate glass	15.8
Na and K diffusion from enamel coating of steel foil	17.6*
NaF precursor layer onto Mo before CIGS deposition on alkali-free glass	17.7
SLG thin film on Ti foil	17.4
Co-evaporation from NaF source	16.4
PDT with NaF on polyimide foil	18.7*
PDT with KF on alumina substrate	14.2
Sequential PDT with NaF and KF on polyimide foil	20.4*

*** Independently certified value.**

CGI AND GGI INFLUENCE ON PDT

Two important variables that have been studied by multiple authors are the CGI and GGI content of the absorber layer. It was noted, that notable differences can be achieved in the electrical parameters by changing these variables, in general parameters like V_{OC} and FF are affected. Different studies have been carried out for variable CGI and afterward, the use of RbF and NaF PDT. In contrast, not many of them have been made varying the GGI concentration.

On one hand, regarding GGI concentration according to Zahedi-Azad et al. [42], for the solar cells with $GGI > 0.33$ the improvement in V_{OC} provided by the PDT ceases. Therefore all the research regarding the use of PDT in CIGS solar cells has been presented using GGI concentrations between 0.24 and 0.33.

On the other hand, the main reason to study the CGI content on CIGS solar cells is due to the fact that an optimum empirical concentration of Cu should be in the range of 0.80 to 0.90. Thanks to the non-stoichiometric concentration, a high quantity of defects are present in the absorber layer [31]. In order to reduce the number of defects, concentrations near stoichiometric Cu have shown to be beneficial by increasing the absorber crystallinity [43], reduce defect density [44] [43], mobility [31] and doping density [45]. Nevertheless, the maximum efficiency achieved with Cu stoichiometric content has never been above 13.5% [46] due to its reduced V_{OC}, FF and J_{SC}.

As it was previously described, the CGI concentration and a PDT have only been studied with NaF and RbF elements. The results obtained are given below:

- Sodium PDT: Carron et al. [47] applied a NaF-PDT using 3 different CGI concentrations (0.85, 0.90 and 0.95). The results show, that for higher CGI concentrations the efficiency (η) of the cell decreased mainly by a reduction in the V_{OC}

and FF. The biggest loss is achieved with $CGI > 0.90$, therefore concentrations of $0.85 < CGI < 0.9$ should be the optimum value. It is important to note, that they use a low temperature process of 450°C that can affect the results of the PDT (due to the substrate material). However, according to Sun et al. [27] in literature, the commonly adopted temperature for Na-PDT is between 350°C and 400°C.

- Rubidium PDT: One important study made by Kodalle et al. [12] investigate the effects of RbF PDT on different CGI concentrations ranging from $0.45 < CGI < 0.95$. The obtained results, demonstrate that the RbF-PDT is more effective with higher CGI, showing that for $CGI > 0.80$ the V_{OC} is increased. However, the RbF-PDT only leads to an improved FF for samples with $CGI = 0.95$, samples with concentration lower than 0.95 the FF decreases. This can be attributed to formation of secondary phases like $RbInSe_2$ in the surface of the absorber and is explained in further detail in [12] and Section 2.1.4.

2.1.4. IMPORTANCE OF DIFFERENT VARIABLES FOR PDT SOLAR CELLS

MANY variables can be modified during the PDT deposition, some of the most studied ones are: temperature of the substrate, temperature of the source, duration of the PDT, CGI and GGI content, type of annealing atmosphere and thickness of the buffer layer (the study of the buffer layer can be extremely extensive and it is not discussed here). Is essential to notice, that the type of substrate and deposition method used will probably implicate huge differences in the temperatures and times of PDT applied on CIGS absorbers. Also, as previously mentioned, up to date research is done using co-evaporation deposition, thus the described variables will reflect only on the obtained results by this deposition method.

SUBSTRATE AND SOURCE TEMPERATURE

Although most of the authors only report the use of one substrate temperature for the PDT deposition mainly in the region of 330°C to 380°C, Feurer et al.[48] performed one study in which they deposited RbF PDT under different substrates and source temperatures (Figures 2.11 and 2.12). They concluded that finding the optimum substrate temperature is more important than the source temperature since a significant detrimental effect is obtained when the optimum temperature is not used.

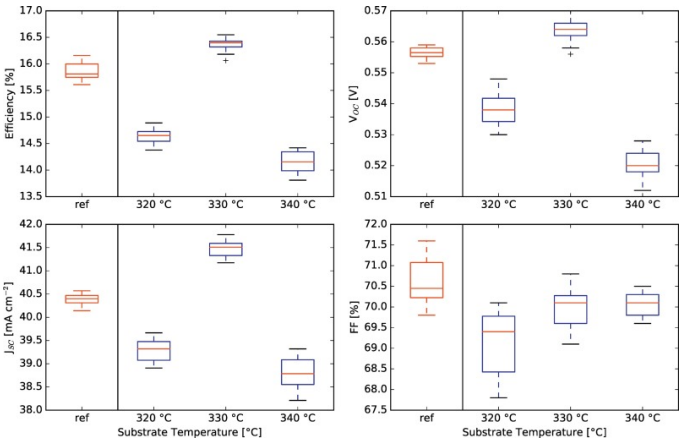

Figure 2.11: Effect of the substrate temperature for RbF PDT. Adapted from [48].

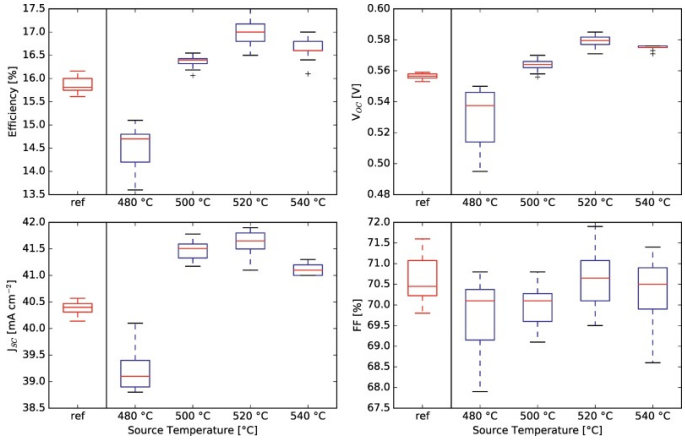

Figure 2.12: Effect of the source temperature for RbF PDT. Adapted from [48].

TYPE OF SUBSTRATE

The type of substrate plays an important role in the temperature and PDT treatment to implement. Taking into account the temperature, some polymeric (PI) substrates can not withstand temperatures higher than 400°C. Another important variable that plays a key role in the type of substrate is the Na content, as has been mentioned in Section 2.1.3, the presence of Na (found in SLG substrates) enhances the diffusion of heavy alkali metals into GBs and not into the bulk. Moreover, the highest efficiencies achieved show the presence of Na in the back part of the absorber (Table 2.1). The presence of Na is directly proportional to the temperature of the substrate, therefore by increasing the temperature more Na can diffuse and be present in the absorber layer. Hence, in case Na is not present in the absorber layer a PDT inducing Na before RbF should be carried out.

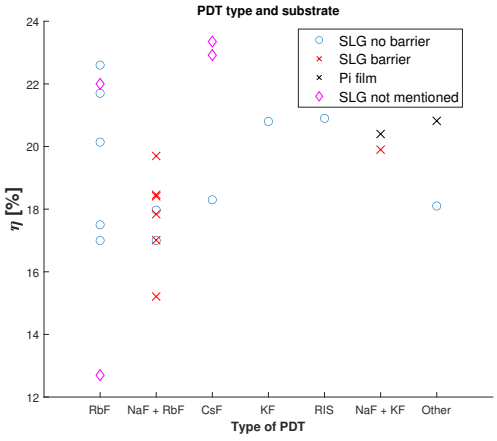

Figure 2.13: Different PDT on multiple substrates [5]-[9],[11]-[15], [49].

GALLIUM GRADING PROFILE AND CONCENTRATION

As discussed by Feurer et al. [50], different types of Ga grading can be achieved in CIGS solar cells. However, the ones that had lead to the highest efficiencies are double graded (notch profile, Figure 2.14) and back graded solar cells. While double graded solar cells provide band-gaps above 1.10 eV, back graded ones provide band-gaps from 1.00-1.10 eV. It is important to mention, that the double grading via sequential deposition is harder to obtain than the back graded one, nevertheless double graded solar cells have achieved the highest efficiencies [9]. Now, considering the GGI content as it can be seen in Table 2.1 highest efficiencies have been achieved with GGI concentrations between 0.20 and 0.33. Nevertheless, this work is based on low band-gap absorber eg. band-gaps between 1.00-1.10 eV, which correspond to average GGI concentrations below 0.33.

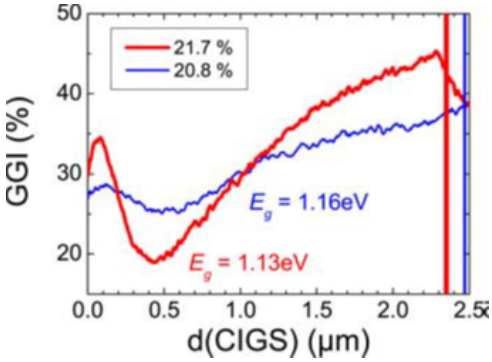

Figure 2.14: Notch Profile of a 21.7% efficient CIGS solar cell (red line) and non graded 20.8% efficient solar cell (blue line). Adapted from [9].

COPPER CONCENTRATION

As it was discussed in Section 2.1.3, CGI content on the absorber layer plays a major role in the efficiency of CIGS solar cells. It has been shown that high CGI contents (> 0.90, Figure 2.15) in addition to PDT of heavy alkali metal fluorides produce high efficiency solar cells by increasing its V_{OC} and FF; however, if the CGI concentration is lower than 0.80 the V_{OC} and FF do not improve. Consequently, as shown in Table 2.1 the best solar cells have been achieved with CGI contents greater than 0.80.

Notice, that the reduction of the FF in samples with low CGI concentration is attributed to a first ordered defect compound (ODC) that tends to form secondary phases such as RIS [12]. Despite that, in the same publication, the formation of a RIS layer in the surface of the absorber can improve more the carrier lifetime and obtain higher V_{OC} in comparison with PDT.

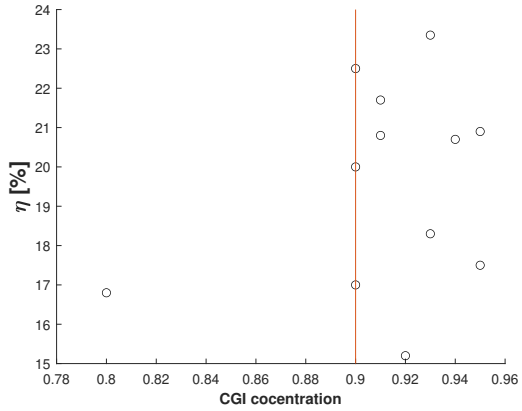

Figure 2.15: Different CGI content samples treated with PDT and efficiency obtained (using only one element for the PDT, eg. RbF or KF) [5]-[9],[11]-[15],[49].

DURATION OF THE PDT

Duration of the PTD is a crucial aspect since it is directly proportional to the concentration of the introduced alkali metal fluoride. According to Kodalle et al. [51], the optimum time to perform a PDT using heavy alkali metal fluorides is 10 minutes, after that time samples show poor performance in electrical parameters (Figure 2.16). However, it is important to take into account that this variable directly correlates and depends on the substrate temperature (Section 2.1.4) and therefore the optimum deposition time varies with the corresponding substrate temperature.

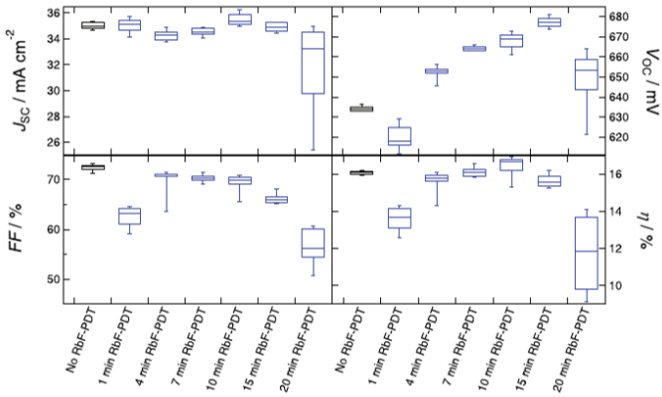

Figure 2.16: Different RbF PDT times. It can be seen that the 10 minute sample shows the best performance among the others (The samples are grown on 2 mm SLG with no Na diffusion barrier). Adapted from [51].

ANNEALING ATMOSPHERE IN PDT

Generally, the annealing process is done after the PDT to enhance the homogeneity and electrical parameters of the samples by promoting the diffusion of the applied alkali metal fluoride. In recent publications, it has been found that the PDT can also be implemented while using Se atmosphere to obtain even better electrical parameters [5]. Other studies perform additional annealing under S or Se atmosphere to boost the properties and to obtain a notch e.g. Ga profile as discussed before. Finally, according to Feurer et al. [48] the optimum time to perform the annealing process under Se atmosphere is 20 minutes, however other studies perform the annealing step for shorter periods between 5 and 20 minutes sometimes with or without S or Se atmosphere [11]. One significant aspect to mention is that by preventing the samples to be exposed to air after the PDT, better electrical parameters can be obtained.

BUFFER LAYER THICKNESS AND MATERIAL

The buffer layer plays an important role in the J_{SC}, since depending on its thickness and material, the solar cell will be able to absorb a wider spectral wavelength of photons and thus have a higher J_{SC}. Considering that, the buffer layer is deposited after performing the PDT the characteristics of the PDT treated absorber surface are important in the selection of the buffer layer material and estimation of the correct thickness needed. Multiple studies have been done to obtain the optimum thickness of the buffer layer, and thereby obtain high J_{SC}. It has been found that using PDT generally lower thickness of buffer layer can be deposited [8], [14], [52]. Moreover, the use of different materials such as ZnO buffer layer leads to higher efficiency solar cells [7]. However, due to simplicity and reproducibility, most of the time CdS buffer layers are used. Figure 2.17 compiles the different thicknesses of buffer layers that have been used for different PDT, and the performance obtained.

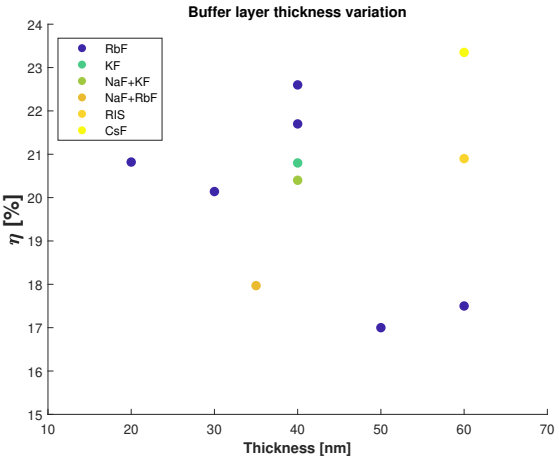

Figure 2.17: Compilation of different buffer layer thicknesses (± 10 nm) and PDT. The CsF PDT uses a double buffer layer with no specified thickness [7]. Adapted from [5],[9] and [13].

SECONDARY PHASES (RIS, KIS)

After performing PDT with Rb or K, the surface of the absorber is generally covered with granular particles that form a new layer. This particles generally correspond to secondary phases of $RbInSe_2$ or $KInSe_2$ [53]. According to Kodalle et al. [12], Ishizuka et al. [15] and Weiss et al. [53], the thickness of this layer directly improves or deteriorates the electrical characteristics of the solar cell, e.g the thicker the layer lower FF and thus lower η. As stated by Kodalle et a. [12] and Ishuzuka et al. [15], the adhesion and thickness of this layer depend on the CGI composition of the surface of the absorber; the lower the CGI a thicker layer will be formed due to a high number of Cu vacancies (defects). Furhtermore, Taguchi et al. [38] found that In plays a key role in the formation of this layer and thus in the improvement in performance of the solar cell. It was concluded that, if there is In present in the surface of the absorber the V_{OC} and FF are increased, however, if there is no In present a detrimental effect is expected. Finally, it is important to mention that the thickness of this layer can be reduced by applying a KCN or HCl risning to the sample [53] [38].

Figure 2.18 left shows the SEM image of the nanopatterned surface, characteristic of a secondary phase layer. In Figure 2.18 right, the Raman shift of a RIS layer can be seen at different laser wavelengths, the principal peaks of the RIS layer are 113.05, 175.8, and 237.9cm^{-1} in Section 3.2.3 a more detailed explanation of these peaks is given. It is important to mention that the formation of this secondary phase is accompanied by the depletion of Cu and Ga along with an enrichment of In and Se concentration [54], [11].

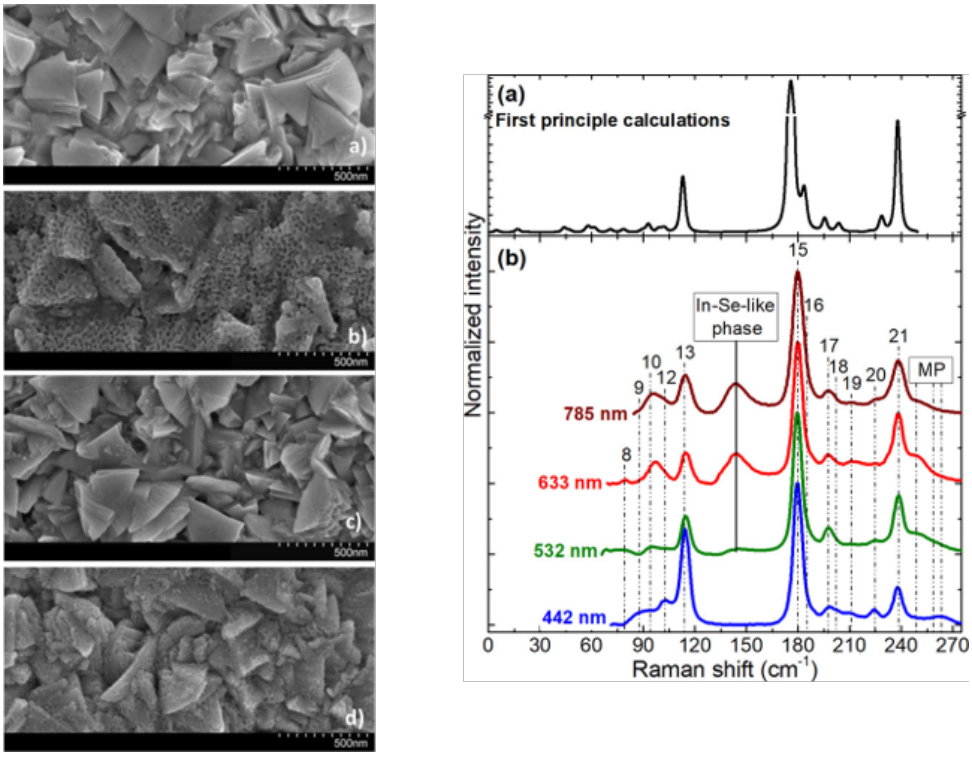

Figure 2.18: **Right** SEM images of differently treated Cu(In, Ga)Se2 (CIGSe) absorbers. Images **a)** and **c)** show the topography of the alkali-free absorbers and image **b)** and **d)** show the respective NaF/KF-PDT CIGSe samples that got an alkali-rich **b)** and an alkali-poor PDT **d)**, respectively. Adapted from [55] **Left a)** Calculated Raman scattering spectra of RbInSe2. A break was made in the Y-axis to elucidate the low-intensity peaks. **b)** Raman scattering spectra of RbInSe2 thin films deposited on an SLG substrate measured under different excitation wavelengths. MP denotes the multiphonon peaks. Adapted from [56].

2.2. PEROVSKITE SOLAR CELLS

ONE of the most promising photovoltaic technologies for the future is the perovskite one. They show high performance at lab scale devices, they are easy to process and the materials used are inexpensive [57]. Moreover, it is possible to modify the opto-electronic properties such as band-gap (1.50-2.50 eV) and absorption coefficient of the solar cell by controlling the shape and size of the materials that are used to produce them [58]. However, this technology also shows some drawbacks such as fast degradation of electrical performance under certain environments, use of toxic materials, and difficulty of scaling up keeping the same performance as on lab scale. Next, the most relevant devices structures, fabrication techniques and, issues of perovskite solar cells are going to be reviewed in order to have a look at this technology and its potential for tandem devices.

Perovskites are materials that form similar structures to Calcium Titanate ($CaTiO_3$) or the formula ABX_3 (Figure 2.19). In the case of solar cells, this structure can be obtained in two different systems. First, alkali-halide perovskites can be formed by the combination of an alkali cation (A) usually Cs, Rb, Na, K, and Li, with a divalent cation (B) which can be Pb, Sn, or Ge and a halogen anion (X) such as Cl, Be, I or F. Or secondly, an organic-inorganic halide based perovskite can be formed with the use of organic structures. As it name suggest, some of the most used organic structures are NH_2CHNH_2, CH_3NH_3 (MA) or $CH_3CH_2NH_3$ [59] in the position of A. In the position of the inorganic cation and anion, one of the divalent cations and halogen anions mentioned before is used. Currently, the combinations that had lead to the best performance and stability are $FAPbI_3$ and $MAPbI_3$ structures [58].

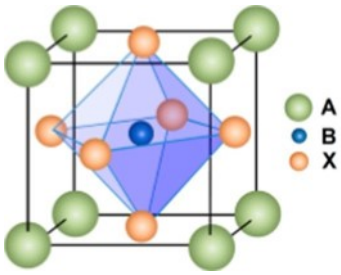

Figure 2.19: ABX_3 perovskite crystal structure. Adapted from [59].

In Figure 2.20 the device structure of a solid-state perovskite cell together with the energy band diagram can be observed. The solar cell is mainly formed by five components: (i) an electron transport layer (ETL) (ii) absorber layer (perovskite) (iii) hole transport layer (HTL) (iv) metal contact and (v) transparent conductive oxide (TCO). Considering that the collection of the generated charge carriers is one of the most important parameters in a solar cell, the HTL and the ETL selected materials play a vital role to obtain high-performing perovskites solar cells. Moreover, these transport layers must show other important properties such as, stability, non-toxicity and must be able to withstand degrading factors like temperature, moisture, or exposure to UV radiation [60], [61] [62].

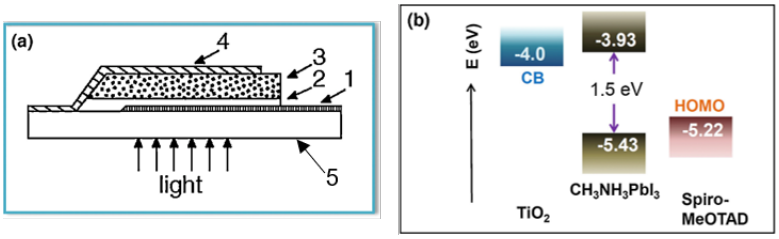

Figure 2.20: **(a)** Cross section of a solid-state perovskite solar cell. **1.** Conducting F-doped SnO2-coated glass (ETL), **2.** Perovskite **3.** Hole transport layer, **4.** Gold electrode **5.** Transparent conductive oxide. Adapted from [63]. **(b)** Schematic energy level diagram of TiO2, CH3NH3PbI3 and spiro-MeOTAD. Adapted from [64].

The different types of devices architectures for perovskite solar cells are depicted in Figure 2.21. The first one, known as dye-sensitized structure was developed in 2009 and is characterized by having a solid or liquid ETL. It showed a power conversion efficiency (PCE) of 3.81% and band-gap of 1.55 eV using $MAPbI_3$ as the absorber device and liquid TiO_2 as the ETL. However, after a short time, the performance of the device dropped by 80% due to the degradation of the liquid ETL [65]. In order to solve this issue, the same architecture was used, but this time a thick solid ETL of m-TiO_2 was implemented and not only the stability but also the PCE was improved from 10 min to 500hr and 9.7%, having a band-gap of 1.50 eV [66]. The second architecture is known as meso-superstructure, in these devices, the m-TiO_2 is replaced by an insulating layer of Al_2O_3. The results showed improvements in the charge collection, by increasing the open circuit voltage while using the same $MAPbI_3$ structure and band-gap (1.55eV) the PCE was increased to 10.9% [67], this can be acknowledged by the combination of the ETL and the perovskite, moreover, this architecture also allows the possibility of having perovskites deposited in flexible substrates [68]. The third one named regular or pillared structure uses the concept of the meso-superstructure of combining the perovskite and the ETL and therefore enables the possibility of using a thicker absorption layer. This concept was first proposed in 2013 by Heo et al. and it achieved a PCE of 12% by implementing $MAPbI_3$ perovskite absorber layer, solid m-TiO_2 as the ETL, and polytriamylamine (PTAA) as the HTL. Nevertheless, due to poor surface morphology, the performance of the device was limited [69]. The last architecture, *pin*-heterojunction is similar to a thin film structure and the ETL is not covered by the perovskite but instead, there is a separation between the top ETL, middle perovskite absorber, and a bottom HTL. These devices showed better stability and performance, achieving PCE above 15% and stability of more than 1000h [70] [71].

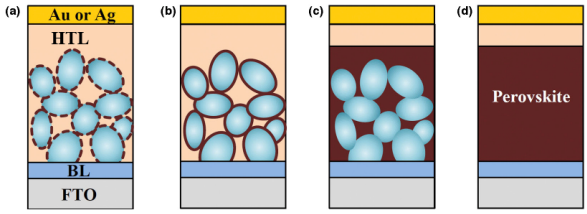

Figure 2.21: Different pervoskite devices architectures. **a.** Dye-sensitized, **b.** meso-superstructure, **c.**regular or pillared structure **d.** *pin*-heterojunction.

There are multiple manufacturing techniques that can be used to produce perovskite solar cell devices. Nonetheless, it is important to bear in mind that lab-scale processes cannot be used to produce large scale devices. The most important aspect to consider during the manufacturing process of this type of solar cells is the quality and properties of the perovskite film, such as morphology, uniformity, and, crystallinity among others. In order to achieve a good performance, the manufacture technique must give complete film coverage to prevent shunting paths and prevent lower absorption [58]. For lab-scale devices, the preferred method is spin coating (one step or two step deposition, Figure 2.22) with the use of anti-solvents to enhance nucleation, crystallinity, and uniformity of the perovskite film [72] [73] or increasing the precursor and substrate temperature (Figure 2.22 right) to induce fast crystallization and ease crystal growth [74]. While for large scale devices there is not an established technique, but the most promising ones are inkjet printing and doctor blade coating.

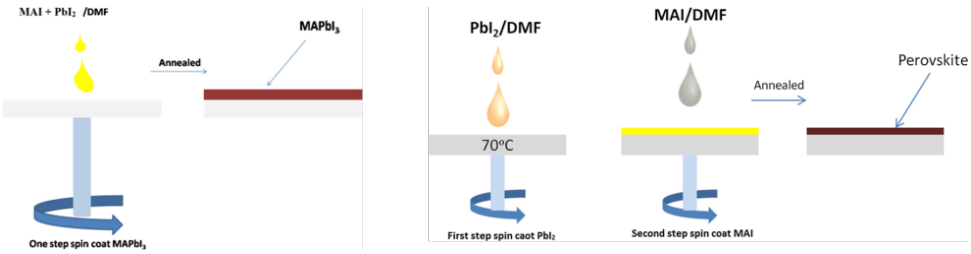

Figure 2.22: Spin coating manufacturing process. **Left.** One step. **Right.** Two step, hot casting sequential. Adapted from [58].

The last aspect to consider is the degradation of perovskite solar cells. This is an important aspect to consider since nowadays produced devices tend to have a life span ranging from a couple of days or months to a maximum of one year [75]. The main factors that affect the stability of the devices are: moisture, temperature, and, exposure to UV lights [76]. In addition, the use of materials such as lead makes perovskite solar cells toxic. In order to overcome this issue, the proposed solution is the use of encapsulation of the device. But still, the problems due to high temperatures and exposure to UV lights can not be solved by this means [77]. At the present, these aspects are now the main focus of research in order to produce feasible perovskite solar cells for commercial use.

2.3. DOUBLE JUNCTION TANDEM DEVICES

ONE innovative idea to increase the PCE of solar cells is to stack different technologies of solar cells on top of another (generally 2 or 3 stacks). Currently, in single junction devices, a large part of the solar spectrum is lost thanks to two main causes. Firstly, photons with lower energy than the solar cell band-gap are not absorbed, and secondly, excess energy from high energy photons is transformed into heat and thus lost due to thermalization. These two main losses were quantified using the Shockley-Queisser limit, and the results show that the maximum conversion efficiency that can be achieved with single junction devices and materials with band-gaps between 1.10 and 1.40 eV is approximately 30-33% [78]. To circumvent this issue, the implementation of two or more layers of materials with different band-gaps and stacking them one on top of the other (higher band-gap on top of lower band-gap Figure 2.23a. it is possible to reduce the thermalization losses and thus increase the PCE of the device.

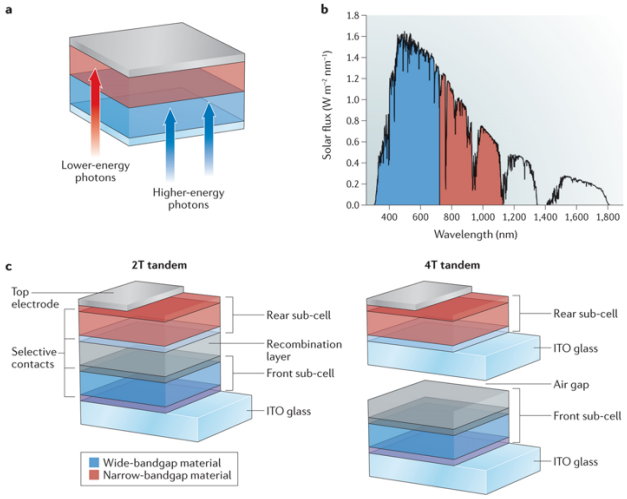

Figure 2.23: a. Tandem solar cell concept, where higher-energy photons are absorbed from the wider-band-gap semiconductor (in blue) and lower-energy photons can be absorbed by the narrower-band-gap semiconductor (in red).b. Solar irradiance spectrum showing the spectral regions over which the two semiconductors could absorb (the color scheme is the same as in part a). c. Diagram of the architecture of two-terminal (2T) and four-terminal (4T) tandem solar cells. Adapted from [79] and [80].

Figure 2.23c. and 2.23d., show the two main designs that can be used to connect the multiple layers of the solar cells. The first one called two terminal (2T) or monolithic configuration requires the fabrication of the top sub-cell directly on top of the bottom sub-cell. Consequently, the processing of this design requires proper use of solvents, thickness, and surface roughness of the layers that compose the device making it more challenging [79] [81] (reviewed in Section 2.3.1). Along with this, by implementing this type of design the cells are connected electronically in series configuration, meaning that the open circuit voltage of the device is the sum of both sub-cells open circuit voltage. While the short circuit current is limited by the bottom sub-cell, thus, the band-gap of both sub-cells must be properly tuned to achieve same short circuit current and reduce

losses. On the other hand, four terminal (4T) configuration devices, can be electrically connected in both series and parallel configuration since each sub-cell is produced in separate substrate and has its independent front and back contacts, however they are physically stacked on top of each other. This type of configuration enables easier manufacturing, avoid the limitation of current matching and thus band-gap optimization is not as critical as with 2T devices. Still, it is important to recall that three out of the four electrical contacts must be transparent to reduce optical and parasitic losses [79].

Among the different variables that play an important role in the creation of tandem devices, the band-gap is the most important one. Figure 2.24 shows the optimum band-gaps and the approximate PCE for 2T and 4T devices. Note that in 4T tandem devices the selection of ban-gap allows choosing from a much wider range compared to 2T. However, in both cases, the bottom cell band-gap should be around 1.10 eV when the top cell used correspond to a perovskite solar cell with a band-gap between 1.50 and 1.60 eV. Due to easier processing, manufacturing (especially for 4T tandem devices), and band-gap tunability, multiple research has been done to create tandem devices made out of just perovskite materials. Nevertheless, the lack of stability in terms of oxidation due to phase segregation [82] and band-gap retention after exposure to illumination [83] make the creation of tandem devices using only perovskite materials arduous. Moreover, 4T and 2T perovskite composed tandems suffer from large voltage deficit due to electronic losses [80]. In contrast, the use of hybrid perovskite-CIGS or Si-Perovskite tandem devices overcome the issue of phase segregation and band-gap stability. Although using Si solar cells as the bottom sub-cell shows the most promising development of tandem devices due to the low cost and maturity of the technology [84] [1], it can not be deposited on flexible substrates [85] and standard Si solar cells are not optimized for infrared absorption [79]. Whereas, CIGS solar cells can be easily optimized for infrared absorption and deposited on flexible substrates. Ideally, to obtain the most optimum perovskite-CIGS 2T and 4T tandem device the band-gaps must be 1.75 and 1.10 eV respectively [84].

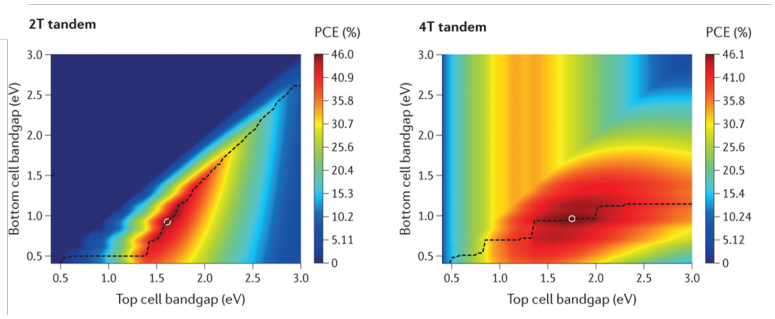

Figure 2.24: Theoretical maximum power conversion efficiency (PCE) as a function of the front (top) and rear sub-cell band-gap for 2T and 4T designs, assuming no absorption losses. The dashed line traces the peak efficiency for the whole range of front-cell band-gaps, and the white circles indicate the maximum power conversion efficiencies. Adapted from [79].

Apart from 2T and 4T tandem devices, over the last years, the development of a new concept three terminal (3T) tandem device started taking place. Nowadays, modeling of 3T tandem devices showed improved performance when compared to 2T and 4T thanks

to the multiple ways in which they can be configured and fabricated, in essence, it combines the advantages of both 2T and 4T tandem devices [86]. There are two main configurations for 3T tandem devices. The first one known as middle contact 3T device, implements a middle contact in the junction of the two sub-cells acts as a common ground and therefore the current form of both sub-cells is extracted, and thus there is no need for an ETL or tunnel junction like in 2T tandem devices [87], [88]. The second one is named integrated back contact (IBC) 3T device, the bottom sub-cell contains two terminals and allows to suppress parasitic absorption caused by the middle contact and consequently increase the performance [86] [89]. To date, only perovskite-Si and combinations of III-V group elements with Si have been used to fabricate 3T terminal tandem devices obtaining maximum efficiencies of 17.1% [86] and 34.5% [90] respectively. Figure 2.25 shows the different structures that can be used to build two cell tandem devices.

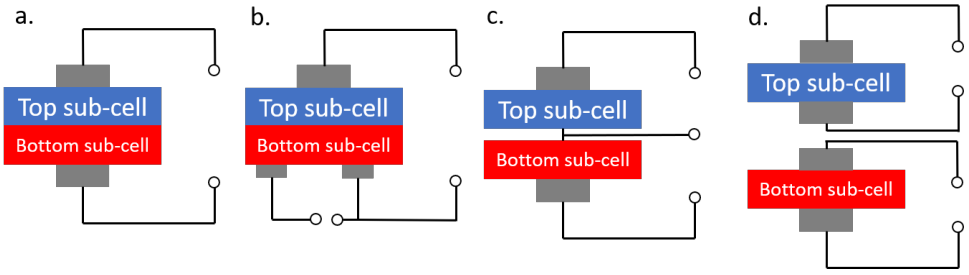

Figure 2.25: Different tandems structures. **a.** 2T structure, **b.** 3T IBC structure, **c.** 3T middle contact structure and **d.** 4T structure.

2.3.1. 2T PEROVSKITE-CIGS TANDEM DEVICES

THE creation of 2T tandem devices requires overcoming multiple challenges. In this section, the most important challenges for the production of 2T perovskite-CIGS devices are going to be discussed and reviewed. Figure 2.26 shows the device structure of a 2T tandem device together with the four vital layers. The first one, composed by the CIGS sub-cell needs to have the optimum band-gap to provide the correct short circuit current and also need to show low surface roughness. The second one is the tunnel junction or recombination layer, which should enable proper recombination of the electron generated carriers from the CIGS sub-cell and the holes from the perovskite sub-cell. The third one is the perovskite top sub-cell, similar to the bottom sub-cell it should provide the proper band-gap and also be highly transparent especially for the high wavelengths of the spectrum close to the NIR. Finally, the topmost layer composed of the ETL and contacts should be also as transparent as possible and provide high mobility for the electrons and thus allowing a proper separation and collection of them [81].

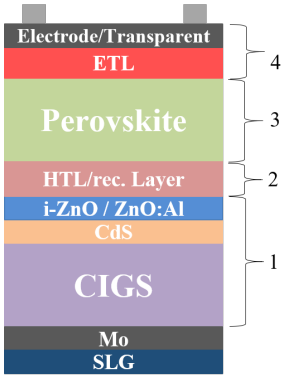

Figure 2.26: 2T perovskite-CIGS tandem structure and the four most important layers.

To begin, the bottom layer composed by the CIGS sub-cell must show a band-gap between 1.08 and 1.10 eV in order to provide accurate current matching with the top sub-cell. As discussed before in Section 2.1.2, by properly tuning the Ga profile in the absorber layer of the CIGS it is possible to achieve absorbers with different band-gap throughout its depth. Still, this sub-cell must also present low surface roughness to prevent shunting and allow for proper growth and deposition of the top cell [81]. Commonly, the surface roughness of a CIGS film can be in the order of 100 nm, [91] which is roughly in the same order of magnitude of the subsequent layers (buffer layer, TCO and perovskite layers). Consequently, by having a high surface roughness the deposition of the next layers can be imperfect by not achieving full coverage, or not having the appropriate thickness which then result in low performance of the tandem device [81]. To overcome this issue, it has been shown that the use of Ag and Cu during the absorber position the roughness of the cell can be improved by promoting grain growth [92].

To finish the bottom CIGS sub-cell, the buffer layer and a TCO are needed. It has been found by Kin et al. [93] that longer CBD deposition times of CdS promote the creation of CdS particles which can be as big as few hundreds nm in diameter, the same order of magnitude as the surface roughness of the CIGS. Thus, this kind of particles may be responsible of the creation of shunting areas were coverage is not achieved. The most common solution to prevent this is to reduce the CBD time and together with this the total thickness of the CdS layer, which can be beneficial and improve the short circuit current or can be detrimental and increase the surface recombination and reduce other electrical parameters such as open circuit voltage and FF. Another solution that can be implemented is the replacement of CdS with atomic layer deposition (ALD) of SnO_2 and thus ensure smooth surface coverage [94]. On top of the buffer layer, a TCO (i-ZnO) in combination with ZnO:Al are applied to provide full coverage of the surface. Furthermore, the use of this layer is essential to properly deposit the HTL and assure good performing tandem devices [81].

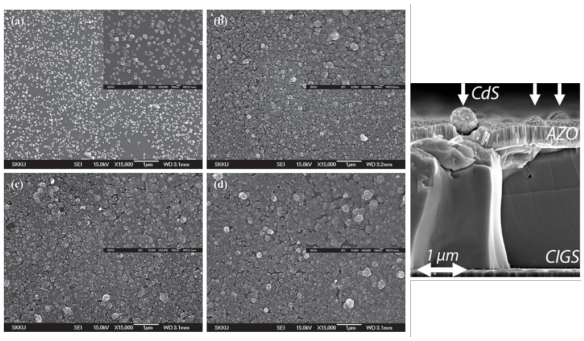

Figure 2.27: SEM micrographs of CdS thin films deposition with different thicknesses: **(a)** 27 nm, **(b)** 57 nm, **(c)** 89 nm, and **(d)** 113 nm. Adapted from [93] and **Right.** cross sectional view of a CdS particle in the surface of the CIGS layer [81].

The next important layer is the transparent recombination layer which needs to effectively create a tunnel junction for the generated electron carriers from the CIGS subcell and enable the recombination with the holes from the perovskite sub-cell. In addition to this, this layer should be transparent in order to enhance the absorption of the bottom sub-cell, and not damage the CIGS stack during its deposition. Some of the HTL materials that have shown good performance and can be implemented in a 2T tandem are: NiO [95]-[96], CuI [97], CuO [98], PTAA [99] among others. But, thanks to its good stability, earth abundance, and compatibility with vacuum deposition procedures NiO is the most used HTL in tandem devices. It can be applied by e-beam evaporation ([100]), sputtering [101]-[102], pulsed laser deposition [103], and ALD [104]. Recently, it has also been found that the use of a double stack of HTL composed by sputtering NiO and spin coating PTAA show higher homogeneity over the sample surface and thus produce better performing samples [81].

The last three layers of the tandem device correspond to the perovskite, ETL, and the top electrode. Some of the most important aspects that the perovskite sub-cell must exhibit are: the optimal band-gap and thickness to absorb all of the high energy photons from the solar spectrum in a single light pass and produce the desired matching current [79]. In addition, it must be stable and be able to avoid problems such as oxidation or phase segregation which could limit the performance of the device (discussed previously in Section 2.2). As well as with the other bottom layers, it should be transparent and provide full coverage to prevent shunts and bad performance. Next, the selection of the optimal ETL to effectively collect and separate the generated electrons in the perovskite tandem should be taken into account. One of the most effective ETL for single cell perovskite devices is the PCBM [105]-[106] achieving PCE above 15%. Nevertheless, when just this ETL is implemented in tandem devices it does not show to properly achieve good coverage resulting in lower performance. But when a combination between different ETL like LiF/PCBM/SnO_2 [81] or C60/SnO_2 [104] are used, proper coverage is achieved and thus good performance is expected. Finally, the last layer consists of the top electrode, most of the time a fluorine doped tin-oxide (FTO) or a TCO are used. This layer needs to exhibit high transmission properties to prevent parasitic or optical

losses.

2.3.2. 4T PEROVSKITE-CIGS TANDEM DEVICES

THANKS to its easier processing and large availability of good performing top and bottom sub-cells, 4T tandems provide are a fast investigation of this type of device due to its easy assembly and robustness. In contrast to 2T design where multiple interfaces need to be considered, in 4T devices the sub-cells only need to be tuned to provide the optimum band-gap. Nonetheless, the requirement of transparent electrodes both (front and rear) for the top sub-cell and front for the bottom sub-cell is the main concern in order to prevent parasitic and optical losses. Besides, both sub-cells are electrically isolated and need individual maximum power point trackers, inverters and additional wiring.

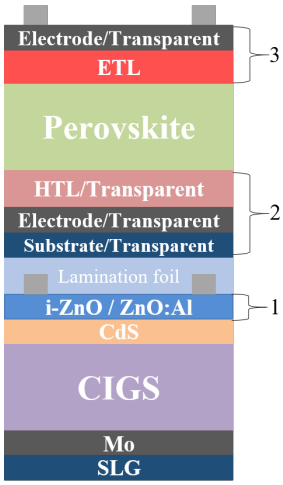

Figure 2.28: 4T perovskite-CIGS tandem structure and the three most important layers.

Figure 2.28 shows the device structure of a 4T tandem device together with the three most relevant layers (apart from the main absorber sub-cells) that need to be optimized to enhance the performance of this type of device. The first layer that needs to be considered is the TCO layer from the CIGS sub-cell, however, this layer has been widely studied, and ZnO:Al is most of the times selected as the front TCO due to its low resistance, high transparency, and low cost thanks to the high abundance of the elements that is made out make it the best option [107]. The next stack of layers that requires optimization are shown in Figure 2.28 with subscript 2. Depending on the type of device that wants to be manufactured (flexible or not) the substrate used can be glass (for rigid devices) or PET (for flexible ones) [108]. On top of the substrate, a transparent electrode needs to be deposited, the first 4T tandem device used a Ag-nanowire transparent electrode with a transmission above 85% and low resistance, making possible to achieve equal efficiency to that of a single junction perovskite solar cell [108]. Recently, one of the best performing 4T tandem devices incorporates an indium zinc oxide (IZO) as the back electrode

[109], other solutions consist on using the same TCO (ZnO:Al) as the bottom CIGS subcell [110]. The next layer is the HTL; the best performing devices use a combination of MoO_3 and Spiro-OMeTAD as the HTL, this combination results in high stability for this layer [109]. Finally, the third stack that needs to be considered is composed of the ETL and the front electrode of the perovskite solar cell. In contrast to the 2T device, the ETL does not need to be composed by multiple layers to enable uniform coverage. Thus, due to its good performance and stability TiO_2 is used in combination with FTO [111]-[110] or tin doped indium oxide ITO [112]-[108].

2.3.3. STATE OF THE ART HIGH EFFICIENCY 4T AND 2T TANDEM DEVICES

In Table 2.3 a short compilation of state of the art high efficiency 2T and 4T devices is provided.

Table 2.3: State of the art high efficiency 4T and 2T tandem devices.

Device Structure	Institute	Year	V_{OC} [V]	J_{SC} [mA cm^{-2}]	FF [%]	PCE [%]	MPP [%]	Area [cm^2]	Reference
2T	HZB	2019	1.58	18.0	76.0	21.6	21.6	0.78	[104]
2T	Empa	2019	1.75	16.3	46.4	13.2	13.2	-	[113]
2T	HZB/KUT	2019	1.68	19.2	81.9	23.3	23.3	1.03	[114]
2T	HZB	2020	1.76	19.2	72.9	24.2	24.2	1.04	[115]
4T	Empa/Solliance	2019	1.03/0.56	20.8/19.4	79.8/74.2	17.2/8.1	25.0	0.57	[31]
4T	KIT/ZSW	2020	1.16/0.71	19.7/13.6	78.7/78.1	17.5/7.5	25.0	0.06/0.5	[116]
4T	Empa	2020	1.09/0.56	22.9/17.5	70.5/73.7	17.3/7.3	24.6	0.3/0.51	[117]

REFERENCES

[1] M. Powalla, S. Paetel, D. Hariskos, R. Wuerz, F. Kessler, P. Lechner, W. Wischmann, and T. M. Friedlmeier, *Advances in cost-efficient thin-film photovoltaics based on Cu(In,Ga)Se_2*, Engineering **3**, 445 (2017).

[2] U. Rau, P. O. Grabitz, and J. H. Werner, *Resistive limitations to spatially inhomogeneous electronic losses in solar cells,* Applied Physics Letters **85**, 6010 (2004), https://doi.org/10.1063/1.1835536 .

[3] N. Naghavi, D. Abou-Ras, N. Allsop, N. Barreau, S. Bücheler, A. Ennaoui, C.-H. Fischer, C. Guillen, D. Hariskos, J. Herrero, R. Klenk, K. Kushiya, D. Lincot, R. Menner, T. Nakada, C. Platzer-Björkman, S. Spiering, A. Tiwari, and T. Törndahl, *Buffer layers and transparent conducting oxides for chalcopyrite Cu(In,Ga)(S,Se)$_2$ based thin film photovoltaics: present status and current developments,* Progress in Photovoltaics: Research and Applications **18**, 411 (2010), https://onlinelibrary.wiley.com/doi/pdf/10.1002/pip.955 .

[4] F. Pianezzi, *Electronic transport and doping mechanisms in Cu(In,Ga)Se_2 thin film solar cells,* (2014).

[5] P. Jackson, R. Wuerz, D. Hariskos, E. Lotter, W. Witte, and M. Powalla, *Effects of heavy alkali elements in Cu(In,Ga)Se_2 solar cells with efficiencies up to 22.6%,* physica status solidi (RRL) - Rapid Research Letters **10**, 583–586 (2016).

[6] NREL, *Best research-cell efficiency chart,* .

[7] M. Nakamura, K. Yamaguchi, Y. Kimoto, Y. Yasaki, T. Kato, and H. Sugimoto, *Cd-free Cu(In,Ga)(Se,S)$_2$ thin-film solar cell with record efficiency of 23.35%,* IEEE Journal of Photovoltaics **9**, 1863–1867 (2019).

[8] T. Kato, J.-L. Wu, Y. Hirai, H. Sugimoto, and V. Bermudez, *Record efficiency for thin-film polycrystalline solar cells up to 22.9% achieved by cs-treated Cu(In,Ga)(Se,S)$_2$,* IEEE Journal of Photovoltaics **9**, 325–330 (2018).

[9] P. Jackson, D. Hariskos, R. Wuerz, O. Kiowski, A. Bauer, T. M. Friedlmeier, and M. Powalla, *Properties of Cu(In,Ga)Se_2 solar cells with new record efficiencies up to 21.7%,* physica status solidi (RRL) - Rapid Research Letters **9**, 28–31 (2016).

[10] Photon.info, *ZSW increases efficiency of cigs solar cell to 22.0%,* (2016).

[11] M. Raghuwanshi, A. Vilalta-Clemente, C. Castro, S. Duguay, E. Cadel, P. Jackson, D. Hariskos, W. Witte, and P. Pareige, *Influence of RbF post deposition treatment on heterojunction and grain boundaries in high efficient (21.1%) Cu(In,Ga)Se_2 solar cells,* Nano Energy **60**, 103–110 (2019).

[12] T. Kodalle, T. Bertram, R. Schlatmann, and C. A. Kaufmann, *Effectiveness of an RbF post deposition treatment of CIGS solar cells in dependence on the cu content of the absorber layer,* IEEE Journal of Photovoltaics **9**, 1839–1845 (2019).

[13] P. Jackson, D. Hariskos, R. Wuerz, W. Wischmann, and M. Powalla, *Compositional investigation of potassium doped Cu(In,Ga)Se_2 solar cells with efficiencies up to 20.8%,* physica status solidi (RRL) - Rapid Research Letters **8**, 219–222 (2014).

[14] A. Chirilă, P. Reinhard, F. Pianezzi, P. Bloesch, A. R. Uhl, C. Fella, L. Kranz, D. Keller, C. Gretener, H. Hagendorfer, and et al., *Potassium-induced surface modification of Cu(In,Ga)Se_2 thin films for high-efficiency solar cells,* Nature Materials **12**, 1107–1111 (2013).

[15] S. Ishizuka, H. Shibata, J. Nishinaga, Y. Kamikawa, and P. J. Fons, *Effects of RbF postdeposition treatment and heat-light soaking on the metastable acceptor activation of CuInSe2 thin film photovoltaic devices,* Applied Physics Letters **113**, 063901 (2018).

[16] S. Wei and A. Zunger, *Band offsets and optical bowings of chalcopyrites and zn-based ii-vi alloys,* Journal of Applied Physics **78**, 3846 (1995), https://doi.org/10.1063/1.359901 .

[17] R. Carron, E. Avancini, T. Feurer, B. Bissig, P. A. Losio, R. Figi, C. Schreiner, M. Bürki, E. Bourgeois, Z. Remes, M. Nesladek, S. Buecheler, and A. N. Tiwari, *Refractive indices of layers and optical simulations of Cu(In,Ga)Se_2 solar cells,* Science and Technology of Advanced Materials **19**, 396 (2018), pMID: 29785230, https://doi.org/10.1080/14686996.2018.1458579 .

[18] J. Gong, Y. Kong, J. Li, K. Wang, X. Wang, Z. Zhang, Z. Ding, and X. Xiao, *Enhancing photocurrent of Cu(In,Ga)Se_2 solar cells with actively controlled ga grading in the absorber layer,* Nano Energy **62**, 205 (2019).

[19] T. Feurer, *Narrow band gap Cu(In,Ga)Se_2 for tandem solar cell application*, Ph.D. thesis, ETH Zurich (2019).

[20] T. Feurer, B. Bissig, T. P. Weiss, R. Carron, E. Avancini, J. Löckinger, S. Buecheler, and A. N. Tiwari, *Single-graded CIGS with narrow bandgap for tandem solar cells,* Science and Technology of Advanced Materials **19**, 263 (2018), pMID: 29707066, https://doi.org/10.1080/14686996.2018.1444317 .

[21] O. Lundberg, M. Edoff, and L. Stolt, *The effect of ga-grading in CIGS thin film solar cells,* Thin Solid Films **480-481**, 520 (2005), eMRS 2004.

[22] P. Jackson, R. Wuerz, D. Hariskos, E. Lotter, W. Witte, and M. Powalla, *Effects of heavy alkali elements in Cu(In,Ga)Se_2 solar cells with efficiencies up to 22.6%,* physica status solidi (RRL) – Rapid Research Letters **10**, 583 (2016), https://onlinelibrary.wiley.com/doi/pdf/10.1002/pssr.201600199 .

[23] P. Szaniawski, P. Salomé, V. Fjällström, T. Törndahl, U. Zimmermann, and M. Edoff, *Influence of varying cu content on growth and performance of ga-graded Cu(In,Ga)Se_2 solar cells,* IEEE Journal of Photovoltaics **5**, 1775 (2015).

[24] D. Colombara, U. Berner, A. Ciccioli, J. C. Malaquias, T. Bertram, A. Crossay, M. Schöneich, H. J. Meadows, D. Regesch, S. Delsante, G. Gigli, N. Valle, J. Guillot, B. El Adib, P. Grysan, and P. J. Dale, *Deliberate and accidental gas-phase alkali doping of chalcogenide semiconductors: Cu(In,Ga)Se_2,* Scientific Reports **7** (2017), 10.1038/srep43266.

[25] F. Hergert, S. Jost, R. Hock, M. Purwins, and J. Palm, *Formation reactions of chalcopyrite compounds and the role of sodium doping,* Thin Solid Films **515**, 5843 (2007), proceedings of Sympodium O on Thin Film Chalcogenide Photovoltaic Materials, EMRS 2006 Conference.

[26] S. Nishiwaki, T. Satoh, Y. Hashimoto, T. Negami, and T. Wada, *Preparation of Cu(In,Ga)Se_2 thin films at low substrate temperatures,* Journal of Materials Research **16**, 394–399 (2001).

[27] Y. Sun, S. Lin, W. Li, S. Cheng, Y. Zhang, Y. Liu, and W. Liu, *Review on alkali element doping in Cu(In,Ga)Se_2 thin films and solar cells,* Engineering **3**, 452–459 (2017).

[28] Lenntech, *Lenntech periodic table,* .

[29] A. Urbaniak, M. Igalson, F. Pianezzi, S. Bücheler, A. Chirilă, P. Reinhard, and A. Tiwari, *Effects of Na incorporation on electrical properties of Cu(In,Ga)Se_2-based photovoltaic devices on polyimide substrates,* Solar Energy Materials and Solar Cells **128**, 52–56 (2014).

[30] F. Pianezzi, P. Reinhard, A. Chirilă, S. Nishiwaki, B. Bissig, S. Buecheler, and A. N. Tiwari, *Defect formation in Cu(In,Ga)Se_2 thin films due to the presence of potassium during growth by low temperature co-evaporation process,* Journal of Applied Physics **114**, 194508 (2013).

[31] T. Feurer, R. Carron, G. Torres Sevilla, F. Fu, S. Pisoni, Y. E. Romanyuk, S. Buecher, and A. N. Tiwari, *Efficiency improvement of near-stoichiometric CuInSe2 solar cells for application in tandem devices,* Advanced Energy Materials 1901428, **9** (2019), 10.1002/aenm.201901428.

[32] T.-Y. Lin, I. Khatri, J. Matsuura, K. Shudo, W.-C. Huang, M. Sugiyama, C.-H. Lai, and T. Nakada, *Alkali-induced grain boundary reconstruction on Cu(In,Ga)Se_2 thin film solar cells using cesium fluoride post deposition treatment,* Nano Energy **68**, 104299 (2019).

[33] R. Wuerz, W. Hempel, and P. Jackson, *Diffusion of rb in polycrystalline Cu(In,Ga)Se_2 layers and effect of rb on solar cell parameters of Cu(In,Ga)Se_2 thin-film solar cells,* Journal of Applied Physics **124**, 165305 (2018).

[34] D. Rudmann, D. Brémaud, A. D. Cunha, G. Bilger, A. Strohm, M. Kaelin, H. Zogg, and A. Tiwari, *Sodium incorporation strategies for CIGS growth at different temperatures,* Thin Solid Films **480-481**, 55–60 (2004).

[35] O. Cojocaru-Mirédin, T. Schwarz, P.-P. Choi, M. Herbig, R. Wuerz, and D. Raabe, *Atom probe tomography studies on the Cu(In,Ga)Se_2 grain boundaries,* Journal of Visualized Experiments (2013), 10.3791/50376.

[36] P. Schöppe, S. Schönherr, R. Wuerz, W. Wisniewski, G. Martínez-Criado, M. Ritzer, K. Ritter, C. Ronning, and C. S. Schnohr, *Rubidium segregation at random grain boundaries in Cu(In,Ga)Se_2 absorbers,* Nano Energy **42**, 307–313 (2017).

[37] T. Kodalle, L. Choubrac, L. Arzel, R. Schlatmann, N. Barreau, and C. A. Kaufmann, *Effects of kf and RbF post deposition treatments on the growth of the cds buffer layer on CIGS thin films - a comparative study,* Solar Energy Materials and Solar Cells **200**, 109997 (2019).

[38] N. Taguchi, S. Tanaka, and S. Ishizuka, *Direct insights into RbInSe$_2$ formation at Cu(In,Ga)Se_2 thin film surface with RbF postdeposition treatment,* Applied Physics Letters **113**, 113903 (2018).

[39] A. Vilalta-Clemente, M. Raghuwanshi, S. Duguay, C. Castro, E. Cadel, P. Pareige, P. Jackson, R. Wuerz, D. Hariskos, W. Witte, and et al., *Rubidium distribution at atomic scale in high efficient Cu(In,Ga)Se_2 thin-film solar cells,* Applied Physics Letters **112**, 103105 (2018).

[40] P. Schöppe, S. Schönherr, M. Chugh, H. Mirhosseini, P. Jackson, R. Wuerz, M. Ritzer, A. Johannes, G. Martínez-Criado, W. Wisniewski, and et al., *Revealing the origin of the beneficial effect of cesium in highly efficient Cu(In,Ga)Se_2 solar cells,* Nano Energy **71**, 104622 (2020).

[41] F. Pianezzi, P. Reinhard, A. Chirilă, B. Bissig, S. Nishiwaki, S. Buecheler, and A. N. Tiwari, *Unveiling the effects of post-deposition treatment with different alkaline elements on the electronic properties of CIGS thin film solar cells,* Physical Chemistry Chemical Physics **16**, 8843–8851 (2014).

[42] S. Zahedi-Azad, M. Maiberg, R. Clausing, and R. Scheer, *Influence of heavy alkali post deposition treatment on wide gap Cu(In,Ga)Se_2,* Thin Solid Films **669**, 629 (2019).

[43] W. Witte, R. Kniese, and M. Powalla, *Raman investigations of Cu(In,Ga)Se_2 thin films with various copper contents,* Thin Solid Films **517**, 867–869 (2008).

[44] S. Siebentritt, L. Gütay, D. Regesch, Y. Aida, and V. Deprédurand, *Why do we make Cu(In,Ga)Se_2 solar cells non-stoichiometric?* Solar Energy Materials and Solar Cells **119**, 18–25 (2013).

[45] A. Gerhard, W. Harneit, S. Brehme, A. Bauknecht, U. Fiedeler, M. Lux-Steiner, and S. Siebentritt, *Acceptor activation energies in epitaxial $CuGaSe_2$ grown by movpe,* Thin Solid Films **387**, 67–70 (2001).

[46] E. Wallin, U. Malm, T. Jarmar, O. L. M. Edoff, and L. Stolt, *World-record Cu(In,Ga)Se_2-based thin-film sub-module with 17.4% efficiency,* Progress in Photovoltaics: Research and Applications **20**, 851–854 (2012).

[47] R. Carron, S. Nishiwaki, T. Feurer, R. Hertwig, E. Avancini, J. Löckinger, S. Yang, S. Buecheler, and A. N. Tiwari, *Advanced alkali treatments for high-efficiency Cu(In,Ga)Se_2 solar cells on flexible substrates,* Advanced Energy Materials **9**, 1900408 (2019).

[48] T. Feurer, F. Fu, T. P. Weiss, E. Avancini, J. Löckinger, S. Buecheler, and A. N. Tiwari, *RbF post deposition treatment for narrow bandgap Cu(In,Ga)Se_2 solar cells,* Thin Solid Films **670**, 34–40 (2019).

[49] S. Ishizuka, N. Taguchi, J. Nishinaga, Y. Kamikawa, S. Tanaka, and H. Shibata, *Group iii elemental composition dependence of RbF postdeposition treatment effects on Cu(In,Ga)Se_2 thin films and solar cells,* The Journal of Physical Chemistry C **122**, 3809–3817 (2018).

[50] T. Feurer, B. Bissig, T. P. Weiss, R. Carron, E. Avancini, J. Löckinger, S. Buecheler, and A. N. Tiwari, *Single-graded CIGS with narrow bandgap for tandem solar cells,* Science and Technology of Advanced Materials **19**, 263–270 (2018).

[51] T. Kodalle, M. D. Heinemann, D. Greiner, H. A. Yetkin, M. Klupsch, C. Li, P. A. V. Aken, I. Lauermann, R. Schlatmann, C. A. Kaufmann, and et al., *Elucidating the mechanism of an RbF post deposition treatment in CIGS thin film solar cells,* Solar RRL **2**, 1800156 (2018).

[52] E. Avancini, R. Carron, T. P. Weiss, C. Andres, M. Bürki, C. Schreiner, R. Figi, Y. E. Romanyuk, S. Buecheler, A. N. Tiwari, and et al., *Effects of rubidium fluoride and potassium fluoride postdeposition treatments on Cu(In,Ga)Se_2 thin films and solar cell performance,* Chemistry of Materials **29**, 9695–9704 (2017).

[53] T. P. Weiss, S. Nishiwaki, B. Bissig, R. Carron, E. Avancini, J. Löckinger, S. Buecheler, and A. N. Tiwari, *Injection current barrier formation for RbF postdeposition-treated Cu(In,Ga)Se_2-based solar cells,* Advanced Materials Interfaces **5**, 1701007 (2017).

[54] P. Schöppe, S. Schönherr, P. Jackson, R. Wuerz, W. Wisniewski, M. Ritzer, M. Zapf, A. Johannes, C. S. Schnohr, C. Ronning, and et al., *Overall distribution of rubidium in highly efficient Cu(In,Ga)Se_2 solar cells,* ACS Applied Materials amp; Interfaces **10**, 40592–40598 (2018).

[55] E. Handick, P. Reinhard, R. G. Wilks, F. Pianezzi, R. Felix, M. Gorgoi, T. Kunze, S. Buecheler, A. N. Tiwari, M. Bar, and et al., *NaF/KF post-deposition treatments and their influence on the structure of Cu(In, Ga)Se_2 absorber surfaces,* 2016 IEEE 43rd Photovoltaic Specialists Conference (PVSC) (2016), 10.1109/pvsc.2016.7749400.

[56] M. Guc, T. Kodalle, R. K. M. Raghupathy, H. Mirhosseini, T. D. Kühne, I. Becerril-Romero, A. Pérez-Rodríguez, C. A. Kaufmann, and V. Izquierdo-Roca, *Vibrational properties of $RbInSe_2$: Raman scattering spectroscopy and first-principle calculations,* The Journal of Physical Chemistry C **124**, 1285–1291 (2019).

[57] Z. T. T. Y. Z. X. Yu. William, Zhou. Di and T. Yafang, *Perovskite-based solar cells: Materials, methods, and future perspectives,* Journal of Nanomaterials **2018** (2018), 10.1155/2018/8148072.

[58] P. Roy, N. Kumar Sinha, S. Tiwari, and A. Khare, *A review on perovskite solar cells: Evolution of architecture, fabrication techniques, commercialization issues and status,* Solar Energy **198**, 665 (2020).

[59] H.-S. Kim, S. H. Im, and N.-G. Park, *Organolead halide perovskite: New horizons in solar cell research,* The Journal of Physical Chemistry C **118**, 5615 (2014), https://doi.org/10.1021/jp409025w .

[60] N. E. Courtier, J. M. Cave, J. M. Foster, A. B. Walker, and G. Richardson, *How transport layer properties affect perovskite solar cell performance: insights from a coupled charge transport/ion migration model,* Energy Environ. Sci. **12**, 396 (2019).

[61] K. Mahmood, S. Sarwar, and M. T. Mehran, *Current status of electron transport layers in perovskite solar cells: materials and properties,* RSC Adv. **7**, 17044 (2017).

[62] M. Jiang, Q. Niu, X. Tang, H. Zhang, H. Xu, W. Huang, J. Yao, B. Yan, and R. Xia, *Improving the performances of perovskite solar cells via modification of electron transport layer,* Polymers **11** (2019), 10.3390/polym11010147.

[63] U. Bach, D. Lupo, P. Comte, J. Moser, F. Weissörtel, J. Salbeck, H. Spreitzer, and M. Grätzel, *Solid-state dye-sensitized mesoporous TiO_2 solar cells with high photon-to-electron conversion efficiencies,* Nature **395**, 583 (1998), cited By 3199.

[64] N.-G. Park, *Perovskite solar cells: an emerging photovoltaic technology,* Materials Today **18**, 65 (2015).

[65] A. Kojima, K. Teshima, Y. Shirai, and T. Miyasaka, *Organometal halide perovskites as visible-light sensitizers for photovoltaic cells,* Journal of the American Chemical Society **131**, 6050 (2009), pMID: 19366264, https://doi.org/10.1021/ja809598r .

[66] H.-S. Kim, C.-R. Lee, J.-H. Im, K.-B. Lee, T. Moehl, A. Marchioro, S.-J. Moon, R. Humphry-Baker, J.-H. Yum, J. E. Moser, M. Grätzel, and N.-G. Park, *Lead iodide perovskite sensitized all-solid-state submicron thin film mesoscopic solar cell with efficiency exceeding 9%,* Scientific Reports **2**, 591 (2012).

[67] M. M. Lee, J. Teuscher, T. Miyasaka, T. N. Murakami, and H. J. Snaith, *Efficient hybrid solar cells based on meso-superstructured organometal halide perovskites,* Science **338**, 643 (2012), https://science.sciencemag.org/content/338/6107/643.full.pdf .

[68] J. M. Ball, M. M. Lee, A. Hey, and H. J. Snaith, *Low-temperature processed meso-superstructured to thin-film perovskite solar cells,* Energy Environ. Sci. **6**, 1739 (2013).

[69] J. H. Heo, S. H. Im, J. H. Noh, T. N. Mandal, C.-S. Lim, J. A. Chang, Y. H. Lee, H.-j. Kim, A. Sarkar, M. K. Nazeeruddin, M. Grätzel, and S. I. Seok, *Efficient inorganic–organic hybrid heterojunction solar cells containing perovskite compound and polymeric hole conductors,* Nature Photonics **7**, 486 (2013).

[70] D. Yang, R. Yang, K. Wang, C. Wu, X. Zhu, J. Feng, X. Ren, G. Fang, S. Priya, and S. F. Liu, *High efficiency planar-type perovskite solar cells with negligible hysteresis using edta-complexed SnO_2,* Nature Communications **9**, 3239 (2018).

[71] X. Liu, Z. Liu, B. Sun, X. Tan, H. Ye, Y. Tu, T. Shi, Z. Tang, and G. Liao, *17.46% efficient and highly stable carbon-based planar perovskite solar cells employing ni-doped rutile TiO_2 as electron transport layer,* Nano Energy **50**, 201 (2018).

[72] N. J. Jeon, J. H. Noh, Y. C. Kim, W. S. Yang, S. Ryu, and S. I. Seok, *Solvent engineering for high-performance inorganic–organic hybrid perovskite solar cells,* Nature Materials **13**, 897 (2014).

[73] M. Xiao, F. Huang, W. Huang, Y. Dkhissi, Y. Zhu, J. Etheridge, A. Gray-Weale, U. Bach, Y.-B. Cheng, L. Spiccia, and et al., *A fast deposition-crystallization procedure for highly efficient lead iodide perovskite thin-film solar cells,* Angewandte Chemie **126**, 10056–10061 (2014).

[74] W. Nie, H. Tsai, R. Asadpour, J.-C. Blancon, A. J. Neukirch, G. Gupta, J. J. Crochet, M. Chhowalla, S. Tretiak, M. A. Alam, H.-L. Wang, and A. D. Mohite, *High-efficiency solution-processed perovskite solar cells with millimeter-scale grains,* Science **347**, 522 (2015), https://science.sciencemag.org/content/347/6221/522.full.pdf .

[75] Q. Wang, N. Phung, D. Di Girolamo, P. Vivo, and A. Abate, *Enhancement in lifespan of halide perovskite solar cells,* Energy Environ. Sci. **12**, 865 (2019).

[76] G. Niu, X. Guo, and L. Wang, *Review of recent progress in chemical stability of perovskite solar cells,* J. Mater. Chem. A **3**, 8970 (2015).

[77] M. Asghar, J. Zhang, H. Wang, and P. Lund, *Device stability of perovskite solar cells – a review,* Renewable and Sustainable Energy Reviews **77**, 131 (2017).

[78] S. Rühle, *Tabulated values of the shockley–queisser limit for single junction solar cells,* Solar Energy **130**, 139 (2016).

[79] G. E. Eperon, M. T. Hörantner, and H. J. Snaith, *Metal halide perovskite tandem and multiple-junction photovoltaics,* Nature Reviews Chemistry **1**, 0095 (2017).

[80] G. E. Eperon, T. Leijtens, K. A. Bush, R. Prasanna, T. Green, J. T.-W. Wang, D. P. McMeekin, G. Volonakis, R. L. Milot, R. May, A. Palmstrom, D. J. Slotcavage, R. A. Belisle, J. B. Patel, E. S. Parrott, R. J. Sutton, W. Ma, F. Moghadam, B. Conings, A. Babayigit, H.-G. Boyen, S. Bent, F. Giustino, L. M. Herz, M. B. Johnston, M. D. McGehee, and H. J. Snaith, *Perovskite-perovskite tandem photovoltaics with optimized band gaps,* Science **354**, 861 (2016), https://science.sciencemag.org/content/354/6314/861.full.pdf .

[81] T. J. Jacobsson, A. Hultqvist, S. Svanström, L. Riekehr, U. B. Cappel, E. Unger, H. Rensmo, E. M. Johansson, M. Edoff, and G. Boschloo, *2-terminal CIGS-perovskite tandem cells: A layer by layer exploration,* Solar Energy **207**, 270 (2020).

[82] X. Zheng, A. Y. Alsalloum, Y. Hou, E. H. Sargent, and O. M. Bakr, *All-perovskite tandem solar cells: A roadmap to uniting high efficiency with high stability,* Accounts of Materials Research **1**, 63 (2020).

[83] E. T. Hoke, D. J. Slotcavage, E. R. Dohner, A. R. Bowring, H. I. Karunadasa, and M. D. McGehee, *Reversible photo-induced trap formation in mixed-halide hybrid perovskites for photovoltaics,* Chem. Sci. **6**, 613 (2015).

[84] W. Shockley and H. J. Queisser, *Detailed balance limit of efficiency of p-n junction solar cells,* Journal of Applied Physics **32**, 510 (1961), https://doi.org/10.1063/1.1736034 .

[85] S. Kim, H. V. Quy, and C. W. Bark, *Photovoltaic technologies for flexible solar cells: beyond silicon,* Materials Today Energy **19**, 100583 (2021).

[86] P. Tockhorn, P. Wagner, L. Kegelmann, J.-C. Stang, M. Mews, S. Albrecht, and L. Korte, *Three-terminal perovskite/silicon tandem solar cells with top and interdigitated rear contacts,* ACS Applied Energy Materials **3**, 1381 (2020), https://doi.org/10.1021/acsaem.9b01800 .

[87] E. L. Warren, W. E. McMahon, M. Rienäcker, K. T. VanSant, R. C. Whitehead, R. Peibst, and A. C. Tamboli, *A taxonomy for three-terminal tandem solar cells,* ACS Energy Letters **5**, 1233 (2020), https://doi.org/10.1021/acsenergylett.0c00068 .

[88] S. Sakai and M. Umeno, *Theoretical analysis of new wavelength-division solar cells,* Journal of Applied Physics **51**, 5018 (1980), https://doi.org/10.1063/1.328382 .

[89] T. Nagashima, K. Okumura, K. Murata, and Y. Kimura, *Three-terminal tandem solar cells with a back-contact type bottom cell,* in *Conference Record of the Twenty-Eighth IEEE Photovoltaic Specialists Conference - 2000 (Cat. No.00CH37036)* (2000) pp. 1193–1196.

[90] S. Essig, C. Allebé, T. Remo, J. F. Geisz, M. A. Steiner, K. Horowitz, L. Barraud, J. S. Ward, M. Schnabel, A. Descoeudres, D. Young, M. Woodhouse, M. Despeisse, C. Ballif, and A. Tamboli, *Raising the one-sun conversion efficiency of iii–v/si solar cells to 32.8% for two junctions and 35.9% for three junctions,* Nature Energy **2**, 17144 (2017).

[91] Z. Jehl, M. Bouttemy, D. Lincot, J. F. Guillemoles, I. Gerard, A. Etcheberry, G. Voorwinden, M. Powalla, and N. Naghavi, *Insights on the influence of surface roughness on photovoltaic properties of state of the art copper indium gallium diselenide thin films solar cells,* Journal of Applied Physics **111**, 114509 (2012), https://doi.org/10.1063/1.4721648 .

[92] M. Edoff, T. Jarmar, N. S. Nilsson, E. Wallin, D. Högström, O. Stolt, O. Lundberg, W. Shafarman, and L. Stolt, *High voc in (Cu,Ag)(In,Ga)Se_2 solar cells,* IEEE Journal of Photovoltaics **7**, 1789 (2017).

[93] D. Kim, Y.-J. Jang, H.-S. Jung, M. Kim, D. Baek, J. Yi, J. Lee, and Y. Choi, *Optimization of CdS buffer layer for high efficiency CIGS solar cells,* Journal of Nanoscience and Nanotechnology **16**, 5074–5077 (2016).

[94] A. Hultqvist, C. Platzer-Björkman, U. Zimmermann, M. Edoff, and T. Törndahl, *Growth kinetics, properties, performance, and stability of atomic layer deposition Zn–Sn–O buffer layers for Cu(In,Ga)Se_2 solar cells,* Progress in Photovoltaics: Research and Applications **20**, 883 (2012), https://onlinelibrary.wiley.com/doi/pdf/10.1002/pip.1153 .

[95] S. Seo, I. J. Park, M. Kim, S. Lee, C. Bae, H. S. Jung, N.-G. Park, J. Y. Kim, and H. Shin, *An ultra-thin, un-doped NiO hole transporting layer of highly efficient (16.4%) organic–inorganic hybrid perovskite solar cells,* Nanoscale **8**, 11403 (2016).

[96] W.-C. Lai, K.-W. Lin, T.-F. Guo, and J. Lee, *Perovskite-based solar cells with nickel-oxidized nickel oxide hole transfer layer,* IEEE Transactions on Electron Devices **62**, 1590 (2015).

[97] W. Sun, S. Ye, H. Rao, Y. Li, Z. Liu, L. Xiao, Z. Chen, Z. Bian, and C. Huang, *Room-temperature and solution-processed copper iodide as the hole transport layer for inverted planar perovskite solar cells,* Nanoscale **8**, 15954 (2016).

[98] H. Rao, S. Ye, W. Sun, W. Yan, Y. Li, H. Peng, Z. Liu, Z. Bian, Y. Li, and C. Huang, *A 19.0% efficiency achieved in CuO_x-based inverted $CH_3NH_3PbI_3xCl_x$ solar cells by an effective cl doping method,* Nano Energy **27**, 51 (2016).

[99] M. Saliba, J.-P. Correa-Baena, C. M. Wolff, M. Stolterfoht, N. Phung, S. Albrecht, D. Neher, and A. Abate, *How to make over 20% efficient perovskite solar cells in regular (n–i–p) and inverted (p–i–n) architectures,* Chemistry of Materials **30**, 4193 (2018).

[100] S. R. Pae, S. Byun, J. Kim, M. Kim, I. Gereige, and B. Shin, *Improving uniformity and reproducibility of hybrid perovskite solar cells via a low-temperature vacuum deposition process for NiO_x hole transport layers,* ACS Applied Materials amp; Interfaces **10**, 534–540 (2017).

[101] G. Li, Y. Jiang, S. Deng, A. Tam, P. Xu, M. Wong, and H.-S. Kwok, *Overcoming the limitations of sputtered nickel oxide for high-efficiency and large-area perovskite solar cells,* Advanced science (Weinheim, Baden-Wurttemberg, Germany) **4**, 1700463 (2017).

[102] M. B. Islam, M. Yanagida, Y. Shirai, Y. Nabetani, and K. Miyano, *Nio_x hole transport layer for perovskite solar cells with improved stability and reproducibility,* ACS Omega **2**, 2291 (2017).

[103] J. H. Park, J. Seo, S. Park, S. S. Shin, Y. C. Kim, N. J. Jeon, H.-W. Shin, T. K. Ahn, J. H. Noh, S. C. Yoon, and et al., *Efficient $CH_3NH_3PbI_3$ perovskite solar cells employing nanostructured p-type nio electrode formed by a pulsed laser deposition,* Advanced Materials **27**, 4013–4019 (2015).

[104] M. Jošt, T. Bertram, D. Koushik, J. A. Marquez, M. A. Verheijen, M. D. Heinemann, E. Köhnen, A. Al-Ashouri, S. Braunger, F. Lang, B. Rech, T. Unold, M. Creatore, I. Lauermann, C. A. Kaufmann, R. Schlatmann, and S. Albrecht, *21.6%-efficient monolithic perovskite/Cu(In,Ga)Se_2 tandem solar cells with thin conformal hole transport layers for integration on rough bottom cell surfaces,* ACS Energy Letters **4**, 583 (2019).

[105] L. Zhou, J. Chang, Z. Liu, X. Sun, Z. Lin, D. Chen, C. Zhang, J. Zhang, and Y. Hao, *Enhanced planar perovskite solar cell efficiency and stability using a perovskite/pcbm heterojunction formed in one step,* Nanoscale **10**, 3053 (2018), cited By 49.

[106] Z.-K. Wang, M. Li, Y.-G. Yang, Y. Hu, H. Ma, X.-Y. Gao, and L.-S. Liao, *High efficiency Pb–In binary metal perovskite solar cells,* Advanced Materials **28**, 6695 (2016), https://onlinelibrary.wiley.com/doi/pdf/10.1002/adma.201600626 .

[107] A. Smets, K. Jäger, O. Isabella, R. van Swaaij, and M. Zeman, *Solar Energy: The Physics and Engineering of Photovoltaic Conversion, Technologies and Systems* (UIT Cambridge, 2016).

[108] C. D. Bailie, M. G. Christoforo, J. P. Mailoa, A. R. Bowring, E. L. Unger, W. H. Nguyen, J. Burschka, N. Pellet, J. Z. Lee, M. Grätzel, R. Noufi, T. Buonassisi, A. Salleo, and M. D. McGehee, *Semi-transparent perovskite solar cells for tandems with silicon and CIGS,* Energy Environ. Sci. **8**, 956 (2015).

[109] H. Shen, T. Duong, J. Peng, D. Jacobs, N. Wu, J. Gong, Y. Wu, S. K. Karuturi, X. Fu, K. Weber, X. Xiao, T. P. White, and K. Catchpole, *Mechanically-stacked perovskite/CIGS tandem solar cells with efficiency of 23.9% and reduced oxygen sensitivity,* Energy Environ. Sci. **11**, 394 (2018).

[110] L. Kranz, A. Abate, T. Feurer, F. Fu, E. Avancini, J. Lockinger, P. Reinhard, S. M. Zakeeruddin, M. Gratzel, S. Buecheler, and A. N. Tiwari, *High-efficiency polycrystalline thin film tandem solar cells,* The Journal of Physical Chemistry Letters **6**, 2676 (2015), https://doi.org/10.1021/acs.jpclett.5b01108 .

[111] F. Fu, T. Feurer, T. Jäger, E. Avancini, B. Bissig, S. Yoon, S. Buecheler, and A. N. Tiwari, *Low-temperature-processed efficient semi-transparent planar perovskite solar cells for bifacial and tandem applications,* Nature Communications **6**, 8932 (2015).

[112] P. Löper, S.-J. Moon, S. Martín de Nicolas, B. Niesen, M. Ledinsky, S. Nicolay, J. Bailat, J.-H. Yum, S. De Wolf, and C. Ballif, *Organic–inorganic halide perovskite/crystalline silicon four-terminal tandem solar cells,* Phys. Chem. Chem. Phys. **17**, 1619 (2015).

[113] F. Fu, S. Nishiwaki, J. Werner, T. Feurer, S. Pisoni, Q. Jeangros, S. Buecheler, C. Ballif, and A. N. Tiwari, *Flexible perovskite/Cu(In, Ga) Se_2 monolithic tandem solar cells,* Cornell University (2019), 1907.10330.

[114] A. Al-Ashouri, A. Magomedov, M. Roß, M. Jošt, M. Talaikis, G. Chistiakova, T. Bertram, J. A. Márquez, E. Köhnen, E. Kasparavičius, S. Levcenco, L. Gil-Escrig, C. J. Hages, R. Schlatmann, B. Rech, T. Malinauskas, T. Unold, C. A. Kaufmann, L. Korte, G. Niaura, V. Getautis, and S. Albrecht, *Conformal monolayer contacts with lossless interfaces for perovskite single junction and monolithic tandem solar cells,* Energy Environ. Sci. **12**, 3356 (2019).

[115] E. Bellini, *Hzb scientists announce 24.16% efficiency for tandem CIGS solar cell,* (2020).

[116] S. Gharibzadeh, I. M. Hossain, P. Fassl, B. A. Nejand, T. Abzieher, M. Schultes, E. Ahlswede, P. Jackson, M. Powalla, S. Schäfer, M. Rienäcker, T. Wietler, R. Peibst, U. Lemmer, B. S. Richards, and U. W. Paetzold, *2d/3d heterostructure for semitransparent perovskite solar cells with engineered bandgap enables efficiencies exceeding 25% in four-terminal tandems with silicon and CIGS,* Advanced Functional Materials **30**, 1909919 (2020), https://onlinelibrary.wiley.com/doi/pdf/10.1002/adfm.201909919 .

[117] Y. Jiang, T. Feurer, R. Carron, G. T. Sevilla, T. Moser, S. Pisoni, R. Erni, M. D. Rossell, M. Ochoa, R. Hertwig, A. N. Tiwari, and F. Fu, *High-mobility In_2O_3:H electrodes for four-terminal perovskite/$CuInSe_2$ tandem solar cells,* ACS Nano **14**, 7502 (2020), pMID: 32459466, https://doi.org/10.1021/acsnano.0c03265 .

3

Experimental Methods

In this Chapter, the process of fabrication of the CIGS solar cells and the multiple employed characterization techniques are described. The first four Sections compile the process of substrate preparation, 3-stage co-evaporation using Ga grading to achieve low band-gap CIGS, afterwards buffer layer and front contact deposition are described. Next, the used compositional and electrical characterization techniques are described. These make possible the identification of important parameters and variables to take into account for the RbF PDT optimization described in detail in Chapter 4.

3.1. DEVICE FABRICATION

3.1.1. SUBSTRATE

ALL the solar cells produced in this work are deposited on a float soda lime glass (SLG) substrate of 1.1mm thickness, the substrate dimensions are 10x10cm^2 (Figure 3.1), which is then cut into 5x5cm^2 in order to perform multiple variations in each of the quadrants if needed. The approximate composition of the SLG can be found in Table 3.1.

Table 3.1: SLG composition.

Elemental Composition of SLG	
SiO_2	70-73 %
Al_2O_3	1.1-2.2 %
Fe_2O_3	0.08-0.14 %
CaO	7-12 %
MgO	1-4.5 %
SO_3	0.05 0.5 %
$NaO_2 + K_2O$	13-15 %

In order to properly deposit the Molybdenum back contact, first, the substrates are cleaned using a standardized Solliance procedure. Then, a sputtering tool is used to deposit two different layers of Mo, the first one is an adhesive layer which is mainly composed of larger grains and act as a buffer for the second layer which is the conductive Mo. This second layer is higher in density and therefore contains smaller grains. The total thickness of the Mo layer is approximately 500nm.

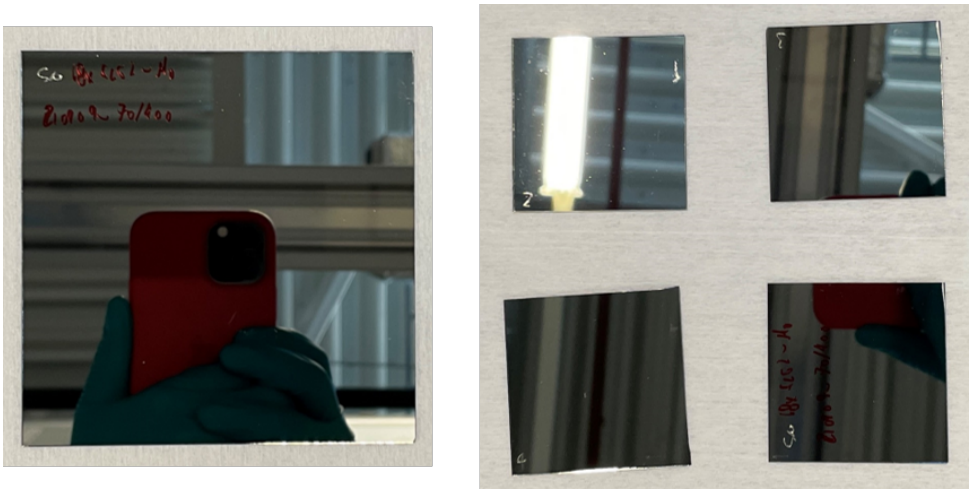

Figure 3.1: Mo on SLG substrate. **a.** 10x10cm^2 SLG/Mo substrate. **b.** 5x5cm^2 Four quadrant division.

3.1.2. ABSORBER GROWTH

THE CIGS absorbers are produced via physical vapor deposition (PVD) using the co-evaporation tool in Figure 3.2

Figure 3.2: Co-evaporation tool.

The source materials used are listed in Table 3.2 along with its purity. The evaporation rate of the elements is controlled by their source temperature. The tool contains one k type thermocouples in each of the crucibles of In, Ga, Cu, and RbF, while the Se source contains two thermocouples, one in the crucible and another one in the heater. Each of the sources is properly calibrated with reference runs to enable reproducibility and repeatability of the absorber.

Table 3.2: Material purity.

Purity of the materials	
In	99.9999 %
Cu	99.9999 %
Ga	99.999 %
RbF	99.98 %
Se	99.999 %

Figure 3.3 illustrates the regular three stage process used to deposit the absorbers, throughout the deposition the temperature of the substrate is kept at 550°C and samples are preheated for 40 minutes to enable Na diffusion from the SLG (some samples were also prepared without the first 40 minutes preheat, explicitly mentioned on the results section). During the first stage In and Ga is deposited, for six minutes. The first two minutes In at a lower rate than Ga. Then, in order to create Ga back graded absorber, the remaining four minutes Ga is ramped down, and In is ramped up. In the second stage, the sample becomes Cu rich by depositing excess Cu, and finally, the last stage In is ramped up again to finish the deposition. The Cu concentration in the sample is controlled by the duration of the second and third stages, therefore variable CGI concentrations can be achieved by tuning the deposition time of these stages. After finishing the deposition, the sample heater is turned off, cooled down, and taken out of the chamber when its temperature is between 150°C-130°C.

After finishing the absorber deposition, the RbF PDT is performed on the samples. Depending on the state of the sample, exposed or not exposed to air a different procedure is followed, described in more detail in Chapter 4.

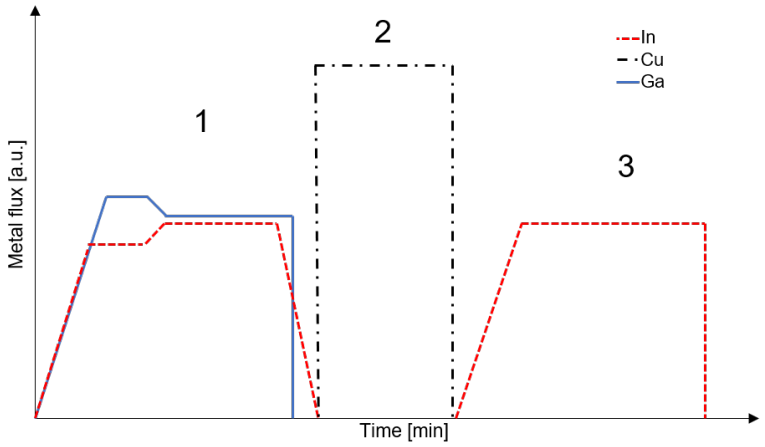

Figure 3.3: Three stage absorber growth.

3.1.3. BUFFER LAYER

ONCE the absorber deposition and RbF PDT is performed on the samples, the CdS buffer layer deposition is carried out. The process is done by chemical bath deposition (CBD), using 600ml of an aqueous solution of Cadmium, ammonia, and thiourea. The CBD is performed at a temperature of 65°C for a period of 4:00 minutes for the standard process (other variations were performed, discussed in Chapter 4), resulting in an approximate thickness of 30-35nm.

However, thanks to the PDT, the CdS layer thickness can be further optimized, and the thickness can be reduced in order to increase the short circuit current, discussed in Section 4.2.4.

3.1.4. FRONT CONTACT

To finish the samples, front contact is deposited by radio frequency magnetron sputtering, using an MRC 643 vertical batch sputtering tool. It consists of two layers, the first one is intrinsic ZnO (i-ZnO) and on top of this aluminum doped zinc oxide (AZO). The i-ZnO is sputtered from a 100% ZnO target with a ratio of 99% Ar to 1% O_2 and the AZO is sputtered from ZnO:3%Al_2O_3 target using 100% Ar. Typically, the resistivity is of approximately 30 Ohm cm^{-2}. The total layer thickness of both layers is approximately 330nm; 60nm i-ZnO and 270nm the AZO.

After the TCO is deposited, Cu grids are placed via sputtering and the sample is manually scribed to create single solar cells of 50mm by 100mm. Each sample can consist of 1 quadrant of 32 single solar cells or 4 quadrants of 128 solar cells (Figure 3.4).

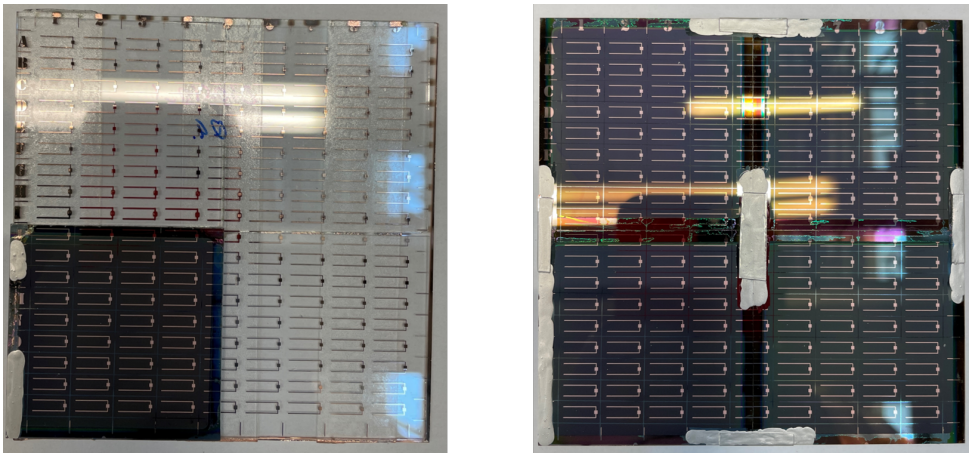

Figure 3.4: One (32 cells) and four (128 cells) quadrant division samples.

3.2. DEVICE COMPOSITIONAL CHARACTERIZATION

3.2.1. X-RAY FLUORESCENCE (XRF)

THE elemental composition of the samples was measured using the Fischerscope X-ray SDV instrument. It uses a 50kV X-ray source and a silicon drift detector. The acquisition time is 15s using a spot size of 3mm. The sample is measured in 36 different points, each of them spaced equally in the x and y direction (Figure 3.5). For quantification, only the K_α peaks of Cu, In, Ga, Se, and Mo are correlated with a calibrated reference sample.

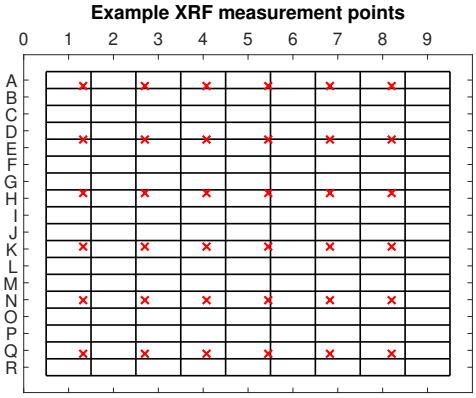

Figure 3.5: XRF measurement positions and sample contour.

Samples are measured by XRF immediately after finishing absorber deposition since with the CdS buffer layer the accuracy of the XRF results is reduced. To calculate the homogeneity of the samples Equation 3.1 is used, where the larger the value is the sample show a large nonuniformity. Also, based on the different points were the XRF is measured the quadrant CGI and GGI can be obtained as well as an approximate concentration of the composition of the cells with the closest XRF measurement point.

$$\%\ \text{of non uniformity.} = \frac{max(x) - min(x)}{max(x)} \times 100\% \tag{3.1}$$

3.2.2. GLOW DISCHARGE OPTICAL EMISSION SPECTROSCOPY (GD-OES):

TO complements the compositional characterization and obtain depth profiles of the multiple elements that are present in the samples glow discharge optical emission spectroscopy (GD-OES) is used. GD-OES allows measuring the elemental distribution of the sample, with a sufficient depth resolution in the typical thickness of the absorber (2-3μm).

However, the measured raw data (intensity vs sputtering time) of GD-OES does not directly allow for analysis of the band-gap profile and molar fractions of each of the elements as a function of the absorber depth. In order to do so, a reliable quantification procedure must be implemented. In order to derive the profiles of the different elements

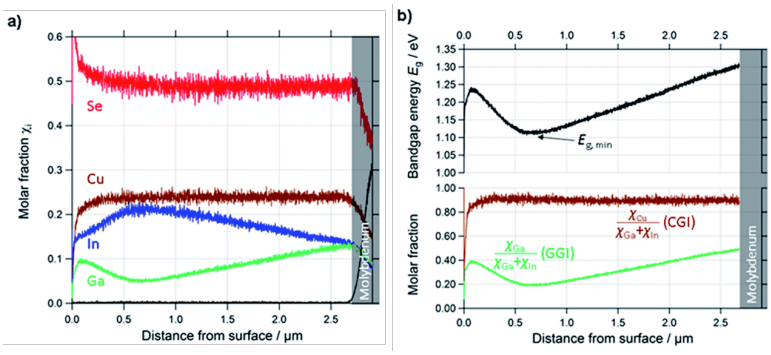

Figure 3.6: **(a)** Quantified depth profile of a standard CIGSe layer. **(b)** Calculated profiles of CGI, GGI, and Eg of the same layer. Adapted from [1].

and the location inside the absorber depth, Figure 3.6 shows the results of implementing Kodalle et al. [1] algorithm based on the assumption of constant emission yield. And thus allowing to quantify correctly the results and obtain molar fraction of each element vs layer depth to calculate the CGI, GGI and calculate the band-gap of the absorber across its depth by using Equation **??**.

All GD-OES depth profiles were measured using the GDA650-system built by Spectruma Analytic in pulse radiofrequency mode. The system uses an Ar-plasma for sputtering and a CCD-array to detect the photons emitted during the relaxation of the atoms and ions and is equipped with a Grimm-type glow discharge source including an anode with an inner diameter of 2.5mm and a non-conducting cathode plate with a front end coupling. The optimal parameters for standard CIGS samples are: Pressure: 2.5hPa, Voltage: 650V, Frequency: 451Hz, Pulse length: 89ms, and duty cycle: 4%.

3.2.3. RAMAN SPECTROSCOPY

To identify the different phases and compounds present in the solar cell Raman spectroscopy can be used. This technique is highly valuable because is non-destructive and thus allows to perform other measurements on the same sample to obtain important results and correlate them. In the case of CIGS solar cells, some of the most important characteristics that can be extracted are: the identification of Cu poor and Cu-In-Se phases also called ordered vacancy compounds (OVC), secondary phases like RIS or KIS, and the correlation of the width of the CIGS A1 mode with the Cu-poor or Cu-rich absorber composition.

In Table 3.2.3, the different Raman shifts of the mentioned phases and compounds can be found. The measurements were done using a Renishaw inVia Raman microscope with a HeNe 633nm wavelength red light laser. The laser power was kept at 10% of the rated power of the laser to prevent degradation of the samples, the acquisition time was set between 15s and 30s sample exposure and 10 accumulations. Depending on the intensity and noise to signal ratio of the results, higher acquisition times or accumulations are used. The penetration depth was estimated to be 300nm. To correct background noises and baseline subtraction, MATLAB software is used following the procedure de-

Table 3.3: Raman shifts for different compounds at different wavelengths.

Compound	Laser Wavelength [nm]	Raman Shift [cm^{-1}]	Reference
OVC ($A1\ CuIn_3Se_2$)	532-633	150-160	[2]
CIGS A1 mode	532-633	173-175	[2]
CIGS B2 mode	532-633	212	[3]
CIGS E mode	532-633	228	[3]
CuSe	514-633	260	[4]
$RbInSe_2$	442	175.8, 113.05, 237.9*	[5]

scribed in Appendix D.

3.3. DEVICE ELECTRICAL CHARACTERIZATION

3.3.1. CURRENT-VOLTAGE MEASUREMENTS (I-V)

LIGHT I-V

BASIC electrical parameters of the solar cell such as efficiency, fill factor, open circuit voltage, short circuit current, series, and shunt resistance are measured under a calibrated solar simulator using standard test conditions (STC) [6]. The V_{OC} and J_{SC} current are calculated from the IV curve3.7. For the series and shunt resistance, the slope is calculated using the point after the V_{oc} and J_{sc} respectively.

$$FF = \frac{V_{MPP} \cdot J_{MPP}}{V_{OC} \cdot J_{SC}} \tag{3.2}$$

$$\eta = \frac{P_{MPP}}{P_{Illumination}} \tag{3.3}$$

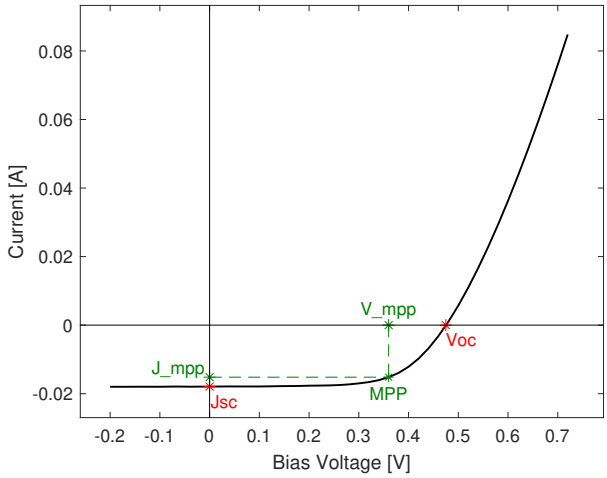

Figure 3.7: LIV curve and relevant parameters.

The mentioned variables are measured using a dual-axis mechanical auto-tracking machine equipped with a Keitley 2400 source to perform the current-voltage measurements. The illumination was provided by an arc lamp mks6286, power supply (mks69911), beam turning mirror (mks66245) to reflect the light normal to the solar cell, and an optical filter holder (mks71260) together with an AM 1.5 filter. The lamp is calibrated with a reference Si cell to provide a power density of 1000 W/m^2. The cells are measured using a bias voltage from -0.2 to 0.6V using a current limit of 0.1A to prevent the destruction of the solar cells by an increased current.

DARK I-V

ONE important technique that can be used to examine and understand the diode properties when the carriers are not generated (by the light) but rather injected.

By making this, it is possible to calculate relevant parameters of the solar cell such as recombination current and diode ideality factor. According to Williams et al. [7], with this technique, in combination with an equivalent circuit model consisting of 2 diodes in parallel, the quality of the material can be evaluated by correlating higher recombination currents with the presence of multiple defects such as micro-scale pinholes in layers of the CIGS, segregation of conductive chemical elements in grain boundaries and thus the formation of resistance pathways. Or diode factors deviated from 1, which can be correlated with different types of recombination such as Auger (n=2/3), radiative (n=1-2) or Shockley-Read-Hall (n=2) [8].

To identify them, a two diode model is described in [7] make use of 4 parallel current pathways (Equations 3.4-3.7) that correspond to the main junction diode, a second diode (weaker), Ohmic leakage current, and non-Ohmic leakage current. By combining all of the above, the dark recombination current can be modeled (Equation 3.8). It is important to recall that the recombination current has a strong dependence on the temperature. In comparison to a one diode model, the two diode model used assure accurate fitting of the experimental results with the modeled ones at room temperature (323K). By isolating the main junction from the effects of non-idealities, series and shut resistance and can be validated by obtaining diode ideality factors within the allowed limits ($1 < n < 2$), which can be calculated using Equation 3.9, where K is the Boltzmann's constant, T is the temperature and q is the electron charge.

$$J_1 = J_{01}(e^{A1V} - 1) \tag{3.4}$$

$$J_2 = J_{02}(e^{A2V} - 1) \tag{3.5}$$

$$J_3 = V/R_{SH} \tag{3.6}$$

$$J_4 = kV^m \tag{3.7}$$

$$J_0 = J_{01}(e^{A1(V-J_0R_s)} - 1) + J_{02}(e^{A2(V-J_0R_s)} - 1) + (V - J_0R_s)/R_{SH} + k(V - J_0R_s)^m \tag{3.8}$$

$$n = \frac{q}{AkT} \tag{3.9}$$

In order to calculate the different parameters, dark I-V values are fitted to Equation 3.8 using a non-linear least square in MATLAB. The model limits the number of iterations to 500, and the specified limits of the calculated parameters are set as in Table 3.4. To evaluate the accuracy of the fit, the error is calculated together with the goodness of the fit (GOF), which is defined as the sum of the squared norm of the residuals. To present the results, the maximum error and GOF values are taken into account since there might be only one point that presents a large error. In case the maximum error is above 12%, the GOF is assessed and if it is larger than 0.9 the results are excluded otherwise the results are included. This excluding procedure was established after assessing previous data sets. The solar cells are measured from -0.2 to 1 V using a current limit of 0.1A to prevent damaging the solar cell.

Table 3.4: Fitted parameters boundaries.

Parameter	Boundaries	Units
J_0	[1x10^{-15} 1x10^{-1}]	A*cm^{-2}
n	[1 3]	-
R_s	[0.1 100]	Ohm*cm^2
R_{SH}	[0.1 1x10^6]	kOhm*cm^2

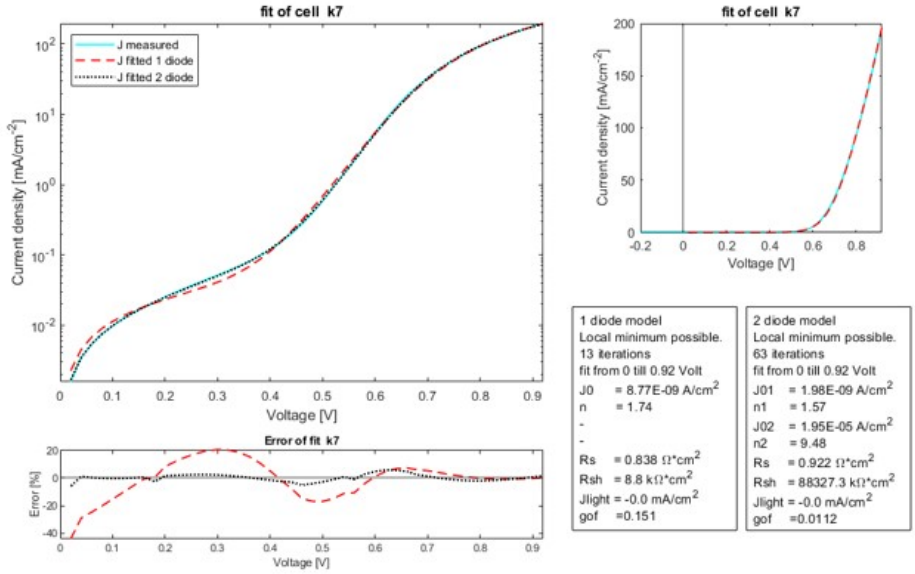

Figure 3.8: Example of the 2 diode model fitting results.

3.3.2. EXTERNAL QUANTUM EFFICIENCY

THE external quantum efficiency (EQE) is measured on a custom setup designed at Solliance. The setup consists of a halogen lamp as a light source and a monochromator. The cells are measured using a 10nm step and 66Hz as the chopping frequency in the lock-in amplifier. Before each set of measurements, the spectrum of the lamp is acquired and calibrated with reference Si and Ge cells.

Figure 3.9 describes the ratio of absorbed and extracted photons, with respect to the total incoming photons in dependence on the illumination wavelength. Among the different characteristics of the solar cell that can be extracted from this curve are: J_{SC}, band-gap, parasitic absorption in the buffer and window layer, and losses due to reflection at the front interface.

To extract the band-gap of the solar cell, the maximum of the derivative $(-d(EQE)/d\lambda)$ is calculated in the NIR. Whereas, by integrating the product of the EQE with the solar photon flux density over the relevant wavelengths, under short circuit conditions ($V = 0$), the current of the solar cell can be obtained. Generally, EQE measurements are performed on the best two cells for each of the quadrants, these two cells are selected based

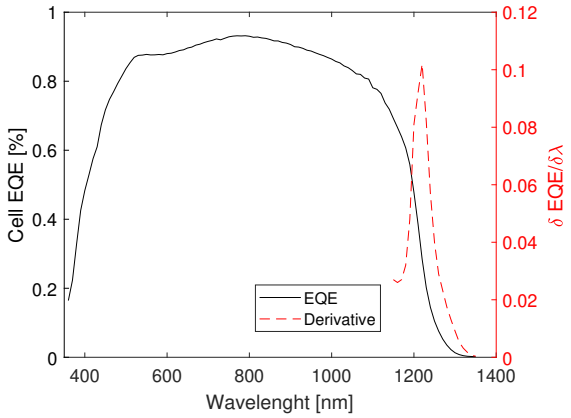

Figure 3.9: The EQE of a typical CIGS solar cell. The band-gap of the absorber layer can be determined by the peak in the derivative in the near infrared region decay of the curve.

on the FF × V_{OC} parameter.

3.3.3. VARIABLE IRRADIANCE MEASUREMENTS (VIM)

THE performance of the solar cells might be affected by several parameters. Two of the most important ones are: the irradiance level and the temperature. By changing the irradiance level at which the cells are exposed, it is possible to obtain the quasi state V_{OC} and J_{SC}, as well as the FF and η dependence on the irradiance level. In comparison to standard IV measurements, this method allows to reduce the effect of the series resistance on the solar cell which generally represents the dominant losses on a solar cell, and thus obtain an ideal IV curve [9].

In addition, by analyzing the different shapes of the IV curves obtained the presence of distortions such as crossover between the curves can be observed, and correlated with possible current barriers present at the different interfaces [10]. Figure 3.10 left, shows the curves obtained under different irradiance levels. From this figure, the V_{OC} and J_{SC} of the solar cell can be extracted and compared with the DIV performance of the solar cell (Figure 3.10 right), the deviation of the DIV and ideal LIV represents different losses in the solar cell. In order to be able to quantify this loss, the procedure explained in Appendix E is implemented.

The data is acquired using the NeonSee solar simulator calibrated with a reference Si solar cell. The variation of the solar spectrum is changed by an attenuator, and the IV parameters are obtained with built-in software. The temperature of the solar cells is kept between 24°C to 25°C with the use of a water chiller. The cells are measured from -0.2 to 0.6V.

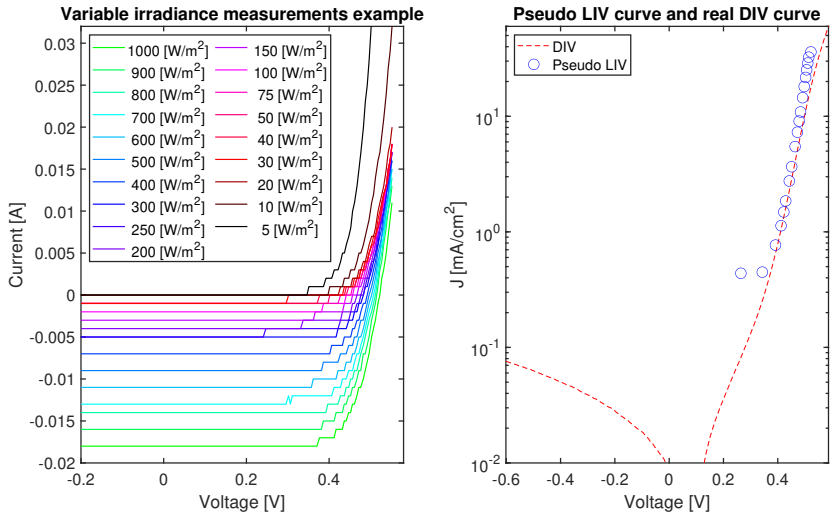

Figure 3.10: Variable irradiance measurements example. **Left.** IV curves of a solar cell under different irradiance levels. **Right.** DIV and Pseudo LIV curve comparison.

3.3.4. LIGHT DEPENDENCE MEASUREMENTS

To investigate the possible presence of a photoactive barrier in one of the two interfaces: CdS/CIGS or CIGS/Mo, light dependence measurements were performed with infrared and blue light. With the use of this technique, depending on the energy of the photons generated with the induced light, the photogenerated carriers will be either at the front or at the back with the blue (high energy photons) or infrared (lower energy photons) light respectively [10]. Furthermore, thanks to the photoconductive effect with the generated carriers either at the front or at the back, the presence of a photoactive barrier can be detected by observing different performances under infra-red, blue, and white light on the different electrical parameters.

Additionally, different distortions in the IV curve such as s-shapes, kinks, or crossovers [11] could appear (Figure 3.11), caused by the presence of deep defects in one of the interfaces mentioned earlier.

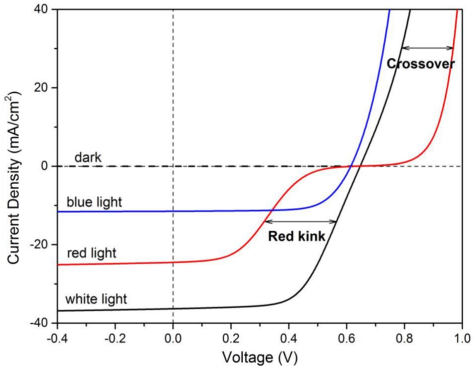

Figure 3.11: Different distortions in IV curves were observed by light dependence measurements. Adapted from [10].

In order to compare the results obtained by both the infrared and blue light, the photogenerated carriers should be as close as possible to the ones generated under white light. However, this is not possible with the current setup without exceeding the maximum rated power of the LED lights used. Nevertheless, the calibration was performed in order to obtain half of the actual J_{SC} of a reference cell for both infrared and blue light. The measurements were performed using mounted LEDs with spectra of 530nm and 850nm, the electrical parameter of the solar cells were extracted using the same setup as with the light IV measurements.

REFERENCES

[1] T. Kodalle, D. Greiner, V. Brackmann, K. Prietzel, A. Scheu, T. Bertram, P. Reyes-Figueroa, T. Unold, D. Abou-Ras, R. Schlatmann, C. A. Kaufmann, and V. Hoffmann, *Glow discharge optical emission spectrometry for quantitative depth profiling of cigs thin-films,* J. Anal. At. Spectrom. **34**, 1233 (2019).

[2] C. Insignares-Cuello, C. Broussillou, V. Bermúdez, E. Saucedo, A. Pérez-Rodríguez, and V. Izquierdo-Roca, *Raman scattering analysis of electrodeposited Cu(In,Ga)Se_2 solar cells: Impact of ordered vacancy compounds on cell efficiency,* Applied Physics Letters **105**, 021905 (2014).

[3] T. Mise and T. Nakada, *Microstructural properties of (In,Ga)$_2$$Se_3$ precursor layers for efficient cigs thin-film solar cells,* Solar Energy Materials and Solar Cells **93**, 1000 (2009), 17th International Photovoltaic Science and Engineering Conference.

[4] C. Rincón and F. J. Ramírez, *Lattice vibrations of $CuInSe_2$ and $CuGaSe_2$ by raman microspectrometry,* Journal of Applied Physics **72**, 4321–4324 (1992).

[5] M. Guc, T. Kodalle, R. K. M. Raghupathy, H. Mirhosseini, T. D. Kühne, I. Becerril-Romero, A. Pérez-Rodríguez, C. A. Kaufmann, and V. Izquierdo-Roca, *Vibrational properties of $RbInSe_2$: Raman scattering spectroscopy and first-principle calculations,* The Journal of Physical Chemistry C **124**, 1285–1291 (2019).

[6] S. Odeh, *The development of a performance indicator for pv power generators,* Transition Towards 100% Renewable Energy Innovative Renewable Energy , 295–309 (2018).

[7] B. L. Williams, S. Smit, B. J. Kniknie, K. J. Bakker, W. Keuning, W. M. M. Kessels, R. E. I. Schropp, and M. Creatore, *Identifying parasitic current pathways in CIGS solar cells by modelling darkj-vresponse,* Progress in Photovoltaics: Research and Applications **23**, 1516–1525 (2015).

[8] P. Education, *Idealty factor and I_0,* .

[9] H. Hidayat, P. Widenborg, and A. Aberle, *Large-area suns-voc tester for thin-film solar cells on glass superstrates,* Energy Procedia **15**, 258 (2012), international Conference on Materials for Advanced Technologies 2011, Symposium O.

[10] T. Song, *Distortions to current-voltage curves of cigs cells with sputtered Zinc(Oxygen,Sulfur) buffer layers,* Ph.D. thesis, Colorado State University (2013).

[11] C.-H. Chung, B. Bob, T.-B. Song, and Y. Yang, *Current–voltage characteristics of fully solution processed high performance CuIn(S,Se)2 solar cells: Crossover and red kink,* Solar Energy Materials and Solar Cells **120**, 642 (2014).

4

RbF POST DEPOSITION TREATMENT OPTIMIZATION

After finishing the absorber deposition, a RbF PDT is implemented with the aim of enhancing the electrical performance of the solar cell. However, it has been observed in previous studies that multiple parameters such as substrate, source temperature, and annealing atmosphere [1], PDT duration [2], CGI of the absorber [3], buffer layer thickness [4] play an important role on the effectiveness of the PDT. Therefore this Chapter is divided in 4 sections, the first one explains in detail the steps involved during the PDT as well as the different sets of experiments that were performed. The next two sections show the material characterization and performance of the solar cells respectively. Finally, a correlation between the observed material properties and electrical performance is performed.

4.1. 3-STAGE RUBIDIUM FLUORIDE POST DEPOSITION TREATMENT

AFTER finishing the regular 3 stage deposition of the CIGS, the next step is to perform the Rubidium fluoride post deposition treatment (PDT). The PDT is divided into three different stages as it can be seen in Figure 4.1. The first one, is the deposition of the capping layer, during this stage In and Se are deposited on the sample at a lower substrate temperature than for the regular three stage deposition, here both temperature and duration play an important role. The second stage, consist of the deposition of RbF under a reduced Se flux. Similarly to the previous stage, substrate temperature and duration of this stage are paramount to obtain good electrical performance. The last stage is the annealing of the sample, in which the sample temperature is kept constant at 380°C and is subjected only to a Se atmosphere.

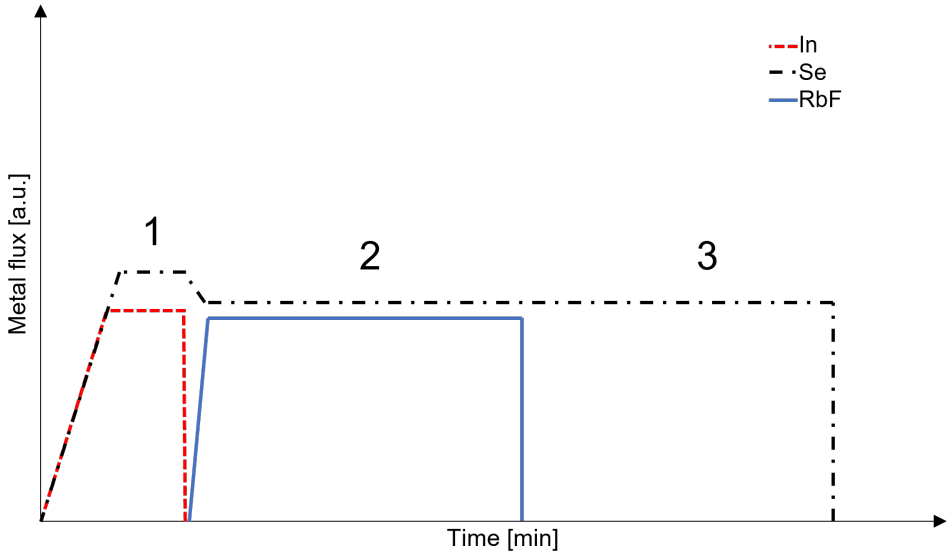

Figure 4.1: Schematic of the 3 stage involved during the PDT. **1.** Deposition of the capping layer, **2.** Deposition of the RbF and **3.** Annealing.

In order to evaluate the impact that each of the three different steps has on the electrical performance and material composition, different experiments were performed. Based on the literature, the substrate temperature during the second stage as well as the duration of this is key in order to obtain proper electrical performance. Therefore, in the first set of samples, a variation of the substrate temperature was implemented. Next, based on the optimum substrate temperature, the RbF flux was modified to extend the duration of the second stage and perform a similar duration as reported on literature (longer deposition but depositing the same amount of material). After noticing that the samples showed a large Cu depletion on the surface, a variation in the duration of the first stage of the PDT was implemented in order to correlate the duration of the InSe cap-

ping layer with the observed Cu depletion and thus lower electrical performance. Subsequently, with the optimum duration and substrate temperature of the first and second stage, and with the desired chemical composition of the absorber (CGI) different variations on the rinsing procedures prior to the deposition of the CdS were performed. Table 4.1 presents the different experiments performed together with the description and purpose.

Table 4.1: Description of the 4 different experiments performed to optimize the first 2 stages of the PDT.

Experiment	Title	Description	Purpose
1	Substrate temperature optimization	Implement 3 different substrate temperatures (340°C-350°C-360°C) during the second stage	Optimization of the substrate temperature
2	RbF flux calibration	Based on the RbF crucible temperature, calibrate the RbF flux for varying RbF crucible temperature	Deposit the same amount of material using 6.5 and 10 minutes
3	InSe capping layer duration	Test 2 different duration of the InSe capping layer deposition (1-2 minutes) during the first stage	Correlation of the InSe capping layer with the creation of OVC
4	Absorber CGI composition	Increase the CGI of the absorber (>0.90).	Observe the electrical performance and OVC amount of high CGI samples

In addition to the different variations implemented for the PDT, it was noticed that the rinsing procedure prior to the deposition of the buffer layer might be another important parameter to optimize in order to prevent losses in the V_{OC} by an excess of alkali in the surface, incomplete coverage as a result of the thinner CdS layer, obtain an ideal J_{SC} and minimize the oxidation of the treated surface. For this reason, the variations on the cleaning procedures prior to the CdS layer depositions described in Table 4.2 were performed.

Table 4.2: Description of the 4 different rinsing procedures performed prior CdS deposition.

Experiment	Rinsing procedure	Description
1	NH_3+N_2 (dry)	Rinse the sample with NH_3 afterwards blow dry with the nitrogen gun and start deposition
2	NH_3 (wet)	Rinse the sample with NH_3 and start deposition
3	NH_3+H_2O+N_2	Rinse the sample with NH_3, afterwards H_2O blow dry and start deposition
4	Room temperature deposition	Place the samples in the holder and start deposition from RT

In the next sections, the different results an analysis of the material and electrical characterization techniques will be presented. The different samples prepared were divided into four different groups depicted in Table 4.3, based on the experiment performed (described in Table 4.1). It is important to bear in mind that some samples might have also a variation in the rinsing procedure prior to the CdS, if this is the case it will be stated on the sample description.

Table 4.3: Description of the 4 different set of samples prepared.

Set name	Description
Temperature series	Overview of the substrate temperature influence during the RbF deposition.
Capping layer variation	Implementation of different substrate temperatures and deposition times for the InSe first stage.
Buffer layer variations	Based on the established substrate temperature and duration of the first and second stage, evaluate the impact of rinsing procedures prior to CdS deposition.
CGI variation	Based on the established substrate temperature and duration of the first and second stage, evaluate the impact on high CGI samples.

4.2. MATERIAL CHARACTERIZATION

In this Section, the results and analysis of Raman spectroscopy, GD-OES, and XRF measurements will be presented for the different sets of samples. For each of the sets, one table will show the description of the variables used for the PDT, CdS rinsing technique, and other relevant notes (if necessary). Thanks to improper removal of the CdS buffer layer on the samples, the quantification of the GD-OES data was not possible. Consequently, the GD-OES data only provides information related to the distribution of the different elements.

4.2.1. TEMPERATURE SERIES

THE substrate temperature is one of the most important parameters of the PDT. The electrical performance of the samples, passivation of OVC is heavily affected by the substrate temperature at which RbF is deposited on the sample.

In order to find the optimum substrate temperature, 3 different sets of samples were deposited varying the temperature, trying to keep the same average CGI and GGI concentrations to minimize the effect of these parameters in the electrical performance of the samples. However, it is important to remember that the samples show sometimes large non-uniformity (Appendix H) in the different quadrants (observed in the XRF maps, Section 3.2.1). After finishing the PDT, all samples received the same CdS buffer layer, TCO, and grids (except for sample 210706_1 which by mistake stayed one night inside the chamber, and the buffer layer was deposited one day after). All the samples prepared for this set were done in a span of two weeks.

Table 4.4: Substrate temperature series overview.

Sample	Substarte Temperature [°C]	Capping layer stage duration [min]	RbF stage duration [min]	Annealing stage duration [min]	CdS description
Reference	-	-	-	-	No rinse. 5:15 min deposition
210625_1	360	2	6.5	20	NH_3+N_2 rinse. 3:30 min deposition
210706_1	350	2	6.5	20	NH_3+N_2 rinse. 3:30 min deposition
210708_1	340	2	6.5	20	NH_3+N_2 rinse. 3:30 min deposition

With the use of XRF, it is possible to quantify the elements present in the different layers of the CIGS and extract important parameters such as CGI and GGI ratios. Table 4.5 shows the results for the different substrate temperatures. Compared to the reference performance, the first thing that can be observed for all PDT samples regardless of the substrate temperature is a large decrease in the CGI of the sample. This can be a result of a Cu depletion caused by the InSe capping layer in which the Cu migrate outside the absorber layer towards the InSe and thus large Cu vacancies are created (observed later with the GD-OES results).

The second thing that can be observed, is that the additional In added with the InSe capping layer on the PDT samples is not affecting the GGI of them. Therefore, the extra InSe layer together with the RbF deposited on the absorbers is only responsible for modifying the Cu content particularly in the surface of the samples and not the Ga content. With Raman spectroscopy (Figure 4.2) a clear difference in the Raman spectra is observed for various substrate temperatures. The presence of the OVC peak at 150 cm^{-1} for PDT samples becomes more prominent with lower substrate temperatures (i.e. 340°C).

Table 4.5: Substrate temperature series compilation XRF results.

Sample	Substarte Temperature [°C]	Average CGI [-]	CGI non uniformity [%]	Average GGI [-]	GGI non uniformity [%]	Avergae thickness [μm]	Thickness non uniformity [%]
210624_2	-	0.89	8.3	0.07	9.8	2.28	8.2
210625_1	360	0.86	6.2	0.07	8.3	1.84	9.2
210706_1	350	0.85	10.7	0.05	9.5	1.63	5.9
210708_1	340	0.85	12.4	0.07	11.0	1.84	8.5

This reduction in the OVC peak for higher substrate temperatures might suggest that the RbF is effectively diffusing throughout the Cu vacancies and thus is passivating them. Whereas on the lower substrate temperatures the diffusion and mobility of Rb are reduced and as a result, higher intensities in the OVC are observed.

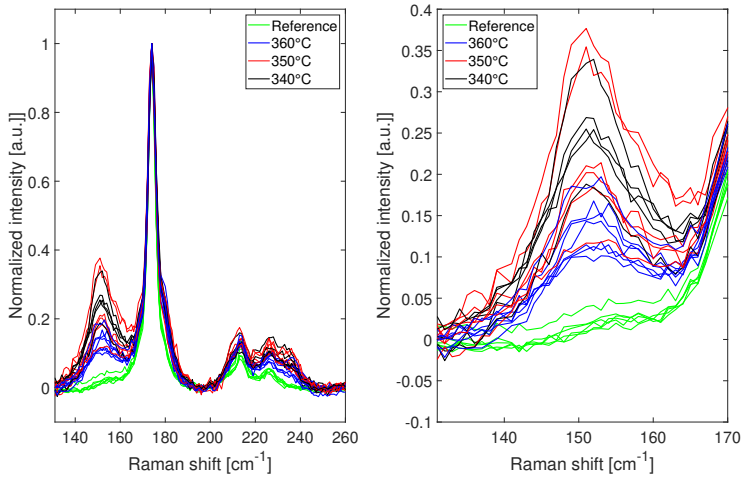

Figure 4.2: Raman spectra for the different substrate temperatures, Lower temperatures create larger intensities in the OVC peak present at 150cm^{-1}.

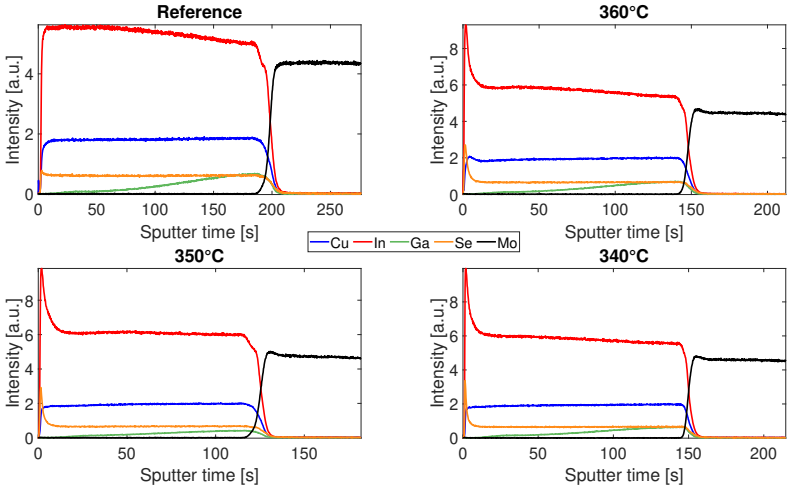

Figure 4.3: Substrate temperature series compilation GD−OES results non-alkali elements, clear In and Se peaks are present in the surface of the PDT samples. No modification of the Ga distribution is observed.

Figure 4.3 shows the distribution of the non-alkali elements for the different substrate temperatures used and the reference sample. The main difference between the PDT solar cells and the reference sample lays on the In and Se peak observed at the front of the absorber. Making a close up into the first 3s of sputtered time (Figure 4.4) it can be noticed that the In peak is accompanied by a strong Cu depletion (between 0 and 1s) in which 340°C show the lowest Cu intensity, followed by 350°C and 360°C, similar to what

the OVC intensities show on the Raman spectra, therefore it can be concluded that the InSe capping layer is responsible for the Cu depletion in the surface of the solar cells.

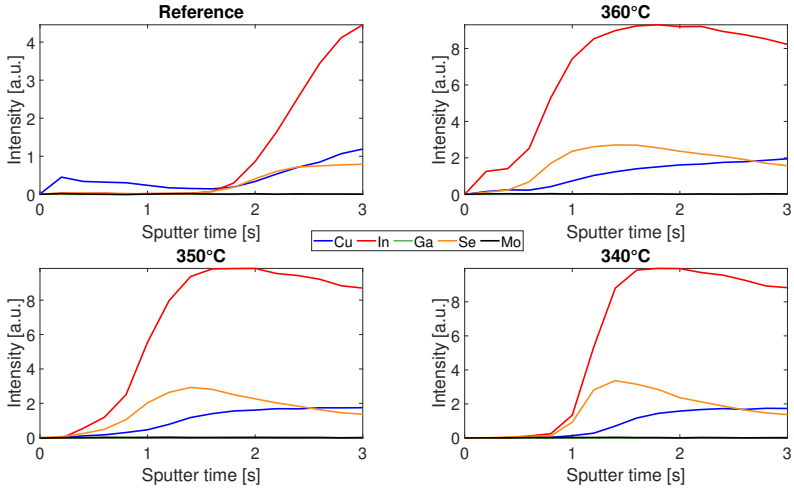

Figure 4.4: Substrate temperature series compilation GD-OES results close up to the surface. Cu depletion accompanied by Se increase is observed on the different substrate temperatures. In some cases (350°C and 360°C) In is also present at the top of the absorbers.

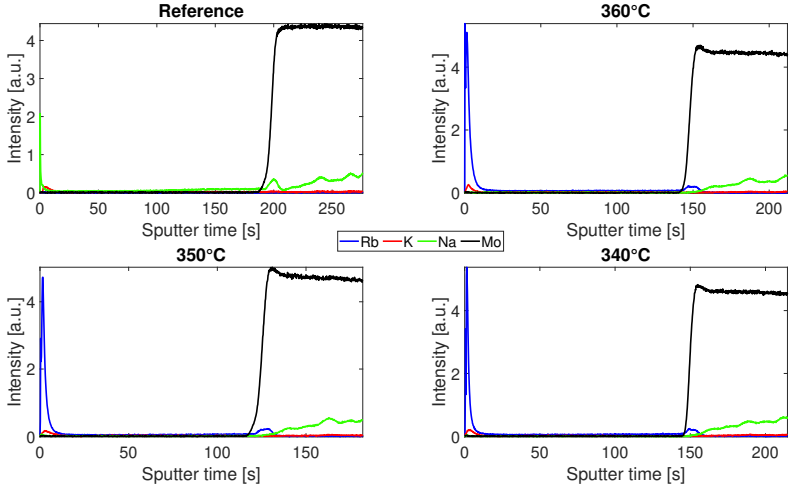

Figure 4.5: Substrate temperature series compilation GD-OES results alkali elements. Large Rb peaks are observed at the top of the PDT absorbers, while K and Na are pushed out in the back.

Analyzing the distribution of the no-alkali elements at the back part of the solar cells close to the Mo back electrode, the 350°C sample shows a different Ga distribution com-

pared to the PDT and reference sample, which can describe the lower performance observed on this sample (especially in the V_{OC} Section 4.3.1).

On Figure 4.5 the distribution for the three alkali elements present in the solar cells can be observed. Obviously, on the reference sample, Rb is not present, but instead, a large Na intensity is observed at the top of the absorber.

Similar to what is reported in the literature, when heavier (Rb) alkali metals are introduced into the CIGS a large decrease of smaller ones (Na, K) is observed (Figure 4.6) this can be explained by the ion exchange mechanism (where Rb occupies the position of Na and K at grain boundaries, thus, these are pushed inside the grains). Additionally, it can be perceived that for all the samples there is a presence of alkali elements in the buffer layer, Na for the reference sample and Rb for the PDT ones. After the buffer layer, the distribution of Rb on the 360°C sample decrease gradually while for 350°C and 340°C a steeper decrease is noticed. Suggesting that Rb is in abundance, thanks to an enhanced diffusion for the higher substrate temperature (360°C).

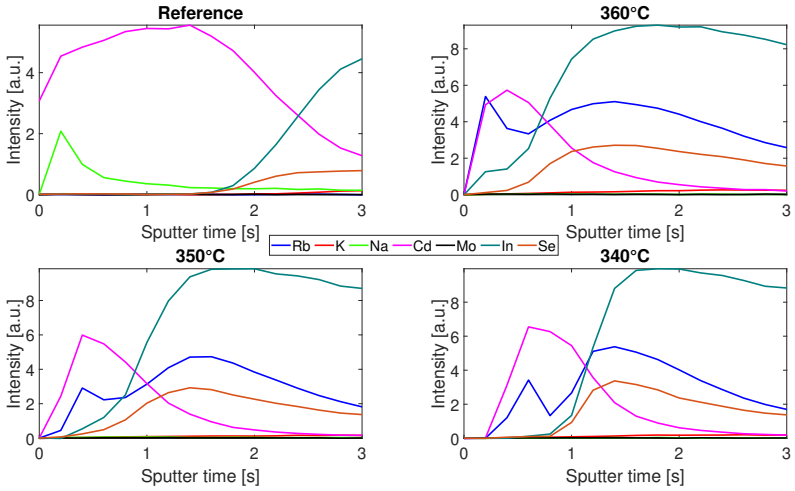

Figure 4.6: Substrate temperature series compilation GD-OES results alkali elements, In, Se, and Cd close up, front. Rb like to be present inside the CdS buffer layer regardless of the substrate temperature used, sometimes the Rb is accompanied by In and Se (350°C and 360°C).

On the back part of the cells (Figure 4.7), accumulation of Na and Rb can be identified especially inside the Mo back contact. On the PDT samples first Rb and afterward Na, while on the reference sample only Na accumulation is observed. Surprisingly no K is detected throughout the absorber in none of the analyzed.

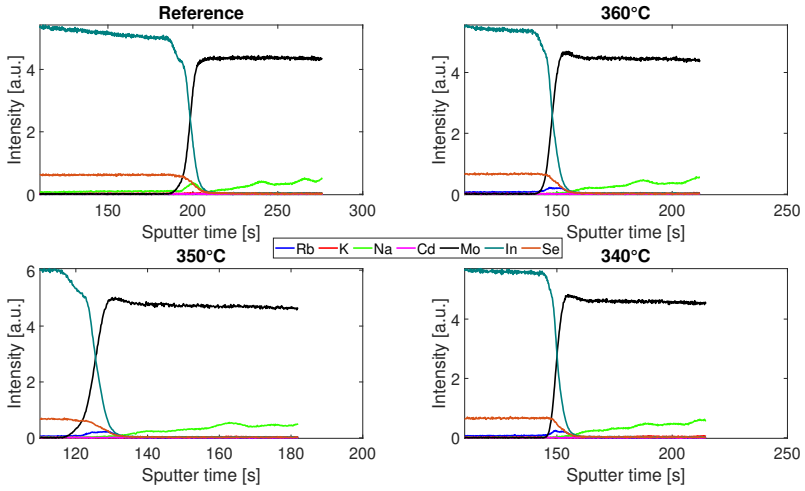

Figure 4.7: Substrate temperature series compilation GD-OES results alkali elements and Mo close up, back. Similar profiles are observed for the PDT absorbers, where Rb pushes out smaller alkali elements (K, Na).

4.2.2. CAPPING LAYER VARIATION

ONE of the variables that need to be considered to perform the PDT, is the capping layer. The aim of the capping layer is to provide a buffer for the RbF allowing it to stick to the surface of the absorber layer and later diffuse throughout it. There are two main variables to consider during the deposition of the capping layer: the temperature of the substrate, and the thickness or duration of the deposition. Based on the literature review, Feurer et al. [1] performed a capping layer of approximately 50 nm thick using a substrate temperature of 380°C.

In order to be able to modify the capping layer, first, a characterization was performed (Appendix F). After this, it was established that to obtain a 50nm capping layer the duration of this stage should be of approximately 2 minutes. To verify the influence that the duration of the capping layer has on the elemental composition of the CIGS, 2 sets of samples were performed and analyzed by Raman spectroscopy and XRF. Table 4.6 shows the detailed description of the samples, the average intensity of the OVC peak, average CGI, and GGI for each of the quadrants. For each of the samples, the same cells were measured and a total of 12 cells were measured by Raman (i.e. 3 in each of the quadrants).

Both samples have the same CBD for depositing the CdS buffer layer of 5:15 minutes, giving an approximate CdS thickness of 60nm, since the goal of the experiment is to verify the impact of the capping layer on the creation of OVC, the samples are only subjected to the first stage of the PDT.

Table 4.6: InSe Capping layer comparison.

Sample	Quadrant	Capping layer stage duration [min]	Approximate thickness [nm]	CGI [%]	GGI [%]	OVC intensity [a.u.]
210726_1	1	1	23.8	0.868	0.057	0.264
	2	1	23.0	0.888	0.056	0.173
	3	1	25.5	0.870	0.055	0.244
	4	1	24.6	0.846	0.055	0.275
210727_1	1	2	47.6	0.857	0.053	0.518
	2	2	46.0	0.871	0.053	0.454
	3	2	53.0	0.862	0.054	0.457
	4	2	49.2	0.848	0.054	0.555

Comparing the 2 different samples, the main difference observed is the intensity of the OVC peak which directly correlates with the duration of this stage. As expected, with a longer and therefore thicker capping layer, the presence of the OVC peak will be increased creating a copper poor surface in which Rb can easily be absorbed and hence diffuse throughout the absorber. Nevertheless, it is important to keep in mind that a high copper poor surface can be detrimental to the electrical performance of the PDT treated CIGS (observed in the previous internship), by mainly reducing the FF of the cells.

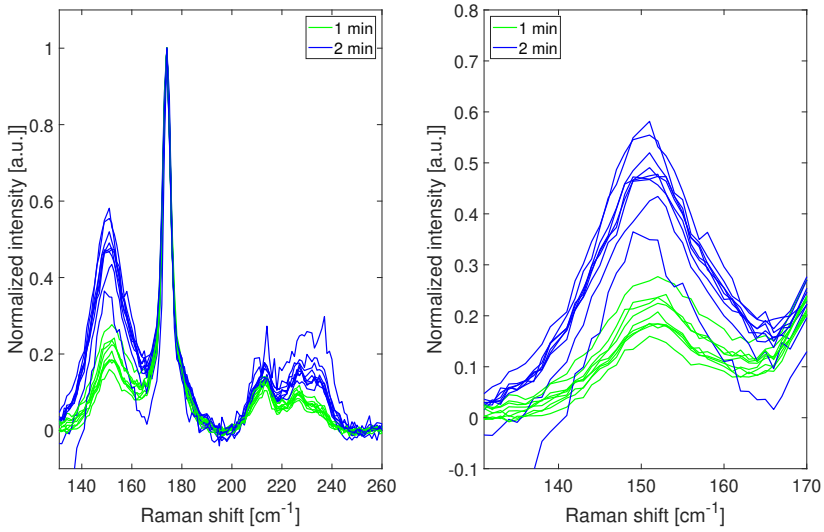

Figure 4.8: 1-2 minutes capping layer Raman spectra, the intensity of the OVC peak is proportional to the duration of the capping layer deposition.

Table 4.7: Capping layer Raman cells results.

Sample	Cell	Capping layer stage duration [min]	OVC Intensity [cm^{-1}]	OVC location [cm^{-1}]	OVC width [cm^{-1}]	CIGS A1 intensity [cm^{-1}]	CIGS A1 location [cm^{-1}]	CIGS A1 width [cm^{-1}]	GOF [%]
210726_1	B2	1	0.178	152	16	0.989	174	4	0.994
210727_1	B2	2	0.473	151	18	0.976	174	5	0.898
210726_1	B4	1	0.149	152	16	0.993	174	4	0.993
210727_1	B4	2	0.418	151	16	0.947	174	4	0.994
210726_1	B6	1	0.183	151	18	0.982	174	4	0.996
210727_1	B6	2	0.490	151	17	0.995	174	4	0.987
210726_1	D7	1	0.220	152	17	0.985	174	4	0.992
210727_1	D7	2	0.495	151	17	0.983	174	4	0.996
210726_1	E3	1	0.191	152	16	0.989	174	4	0.996
210727_1	E3	2	0.485	151	17	0.991	174	4	0.989
210726_1	G2	1	0.181	152	18	0.981	174	4	0.994
210727_1	G2	2	0.462	151	17	0.982	174	4	0.996
210726_1	H8	1	0.275	152	19	0.977	174	5	0.993
210727_1	H8	2	0.564	151	17	0.982	174	4	0.991
210726_1	N3	1	0.240	151	17	0.992	174	4	0.997
210727_1	N3	2	0.546	151	17	0.971	174	4	0.993
210726_1	Q1	1	0.232	151	18	0.992	174	4	0.995
210727_1	Q1	2	0.348	151	13	0.937	174	4	0.996

Although the GGI compositions obtained by the XRF measurements differ by 0.03% by inspecting the location of the CIGS A1 mode it can be stated that the InSe capping layer is only affecting the Cu and not the Ga concentration, since for all the measured cells the location of the CIGS A1 mode is on the same Raman band. Similar to what can be observed with the Ga distribution and intensity from the GD-OES results (Section 4.2.1). Moreover, the Cu depletion is only produced on the surface in most of the cases given that the width of the CIGS A1 mode is constant and not changing extremely when comparing 1 and 2 minutes capping layer depositions times. Furthermore, the creation of OVC in all the quadrants of the samples is homogeneous as given the OVC intensities and the results obtained in Appendix F.

4.2.3. CGI VARIATION

BASED on the electrical performance obtained with the different substrate temperatures for the RbF deposition and the duration of the capping layer, three important decisions were taken: the first one related to the capping layer, it was established that the 2 minutes capping layer deposition was lengthy and therefore large amount of OVC were not been passivated by the RbF, therefore 1 minute InSe capping layer deposition is performed instead of 2. The second one, related to the substrate temperature for the RbF deposition and duration of this stage. It was concluded that the substrate temperature must be 360°C for the RbF deposition and an extended duration of the PDT should be performed i.e. from 6.5 to 10 minutes (Appendix G) in order to enhance the Rb diffusion. Finally, the last decision was to increment the CGI content of the samples, according to literature and suggestions from partners.

In Table 4.8 an overview of the 4 different quadrants of the high CGI sample is shown. As stated previously, the purpose of this sample is to evaluate the performance obtained after the different variables of the PDT were tuned. In addition, compared to the temperature series (Section 4.2.1) the duration and cleaning procedure for the CdS layer deposition is different (discussed in Section 4.2.4).

Table 4.8: High CGI series overview.

Sample	Quadrant	Substarte [°C]	Capping layer stage duration [min]	RbF stage duration [min]	Annealing stage duration [min]	CdS description
210624_2	1	-	-	-	-	No rinse. 5:15 min deposition
210803_1	1	360	1	10	20	NH_3 (Wet), 4:00 min deposition
210803_1	2	360	1	10	20	NH_3 (Wet), 4:00 min deposition
210803_1	3	360	1	10	20	NH_3+N_2, 4:00 min deposition
210803_1	4	360	1	10	20	NH_3+N_2, 4:00 min deposition

Table 4.9: High CGI series XRF results.

Sample	Quadrant	Average CGI [-]	CGI non uniformity [%]	Average GGI [-]	GGI non uniformity [%]	Avergae thickness [μm]	Thickness non uniformity [%]
210624_2	1	0.892	8.3	0.07	9.8	2.28	8.2
210803_1	1	0.904	4.0	0.06	4.9	2.26	3.5
210803_1	2	0.923	3.8	0.06	4.1	2.26	4.2
210803_1	3	0.887	6.9	0.06	11.9	2.20	5.6
210803_1	4	0.871	4.7	0.06	6.5	2.20	5.8

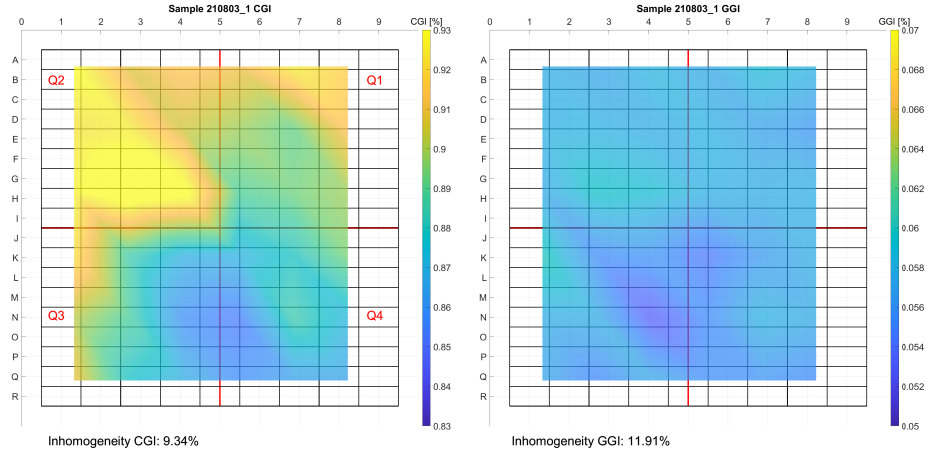

Figure 4.9: High CGI series XRF results.

Table 4.9 shows the different CGI, GGI, and thickness obtained for the CGI variation sample. Compared to the previous set of samples, it can be observed that on average the CGI is around 0.03 higher. In Figure 4.9, the map of the 4 different quadrants from sample 210803_1 can be observed. As generally observed with Solliance co-evaporation depositions, quadrants 1 and 2 have the higher CGI among the rest (Appendix H), thus, is not a consequence of the different rinsing procedures prior to the CdS deposition.

In agreement with these results of the XRF analysis, the spectra of the different quadrants for the high CGI sample (Figure 4.10) do not show a high intensity for the OVC at 150cm^{-1}. Still, the quadrants with lower CGI reported by XRF (Q3 and Q4) show a slightly higher intensity around that area, but the fitting routine does not detect them as a peak since the intensity is below 10% of the maximum value. Therefore, by reducing the InSe capping layer deposition time, extending the RbF deposition duration, and increasing the overall CGI of the samples (i.e. reducing the time of the third stage during the absorber deposition) it is possible to achieve a low concentration of OVC in the surface of the absorbers. Besides this, the overall GGI concentration of the samples is not modified regardless of the modification of the PDT variables or the 3-stage step in the co-evaporation process to deposit the absorber.

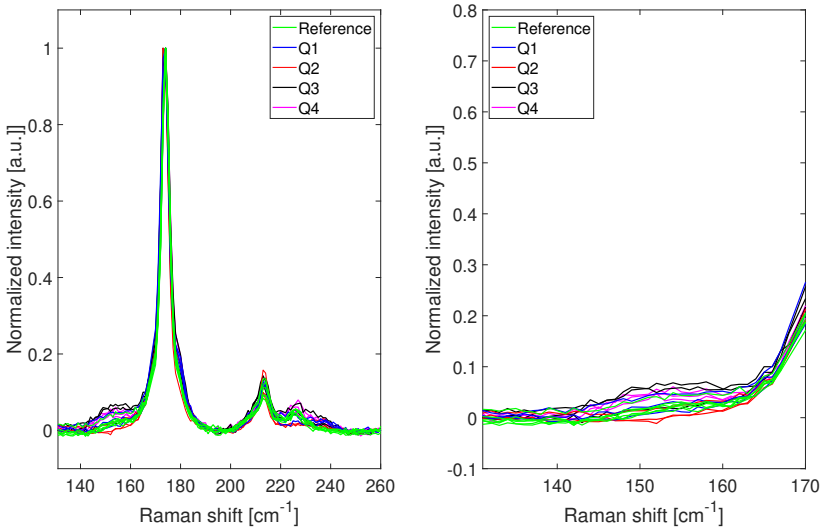

Figure 4.10: High CGI series Raman spectra for the different quadrants, as a result of the high CGI and reduced duration of the capping layer deposition, no OVC are created on the surface of the CIGS.

In Figure 4.11 and 4.12 the distribution of the non-alkali elements for quadrant two can be observed. Similar to the Temperature Series samples (Section 4.2.1), a large in the Se intensity can be identified in the surface of the samples. Although, in this case, the In and Cu signals of reference and 210803_1 samples show a similar distribution, the latter one with stronger intensity showing a direct correlation between the observed Raman spectra with none OVC.

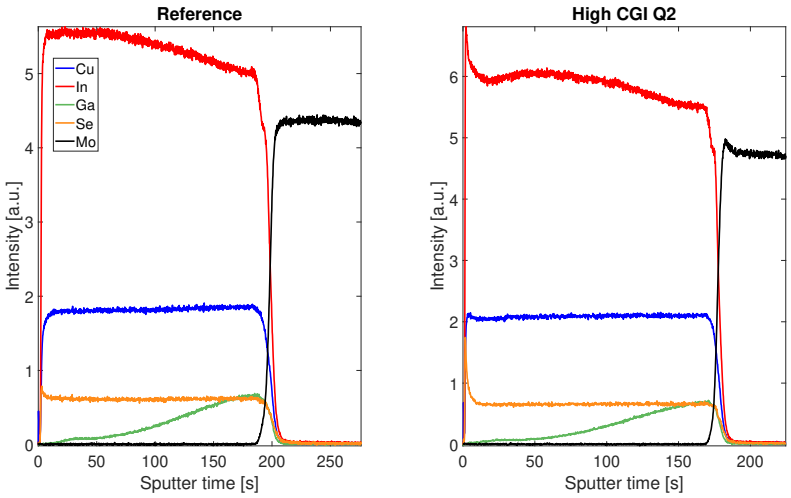

Figure 4.11: GD-OES results, non alkali elements for the high CGI series (quadrant two). Significant In and Se peak are present at the surface of the absorbers, and a small Cu migration towards the front. With respect to Ga, no modification is noticed.

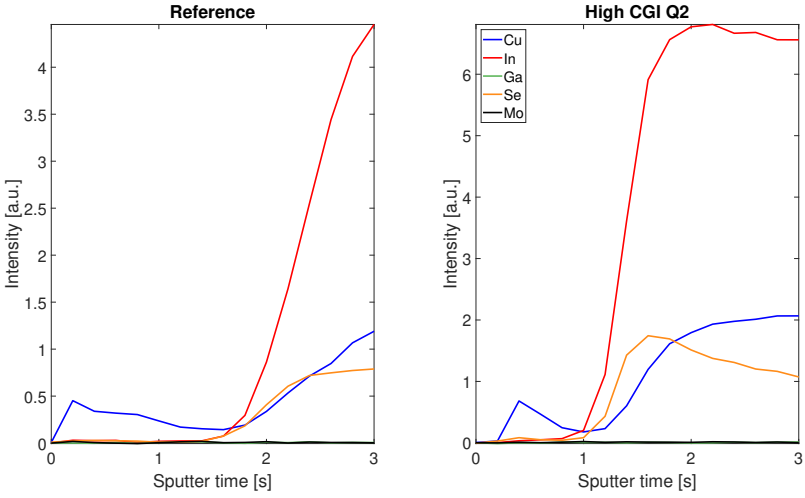

Figure 4.12: GD-OES results, non alkali elements for the high CGI series (quadrant two), close up. No Cu depletion is observed at the front of the absorbers. However compared to the reference, In and Se show larger intensities.

Overall, the intensity and distribution of the non-alkali elements after a sputter time of 3s is reasonably similar. Except for the In signal, which is around 1.5 times larger, as a result of the deposited InSe capping layer which in this sample is not creating a Cu depletion and probably just diffusing throughout the absorber.

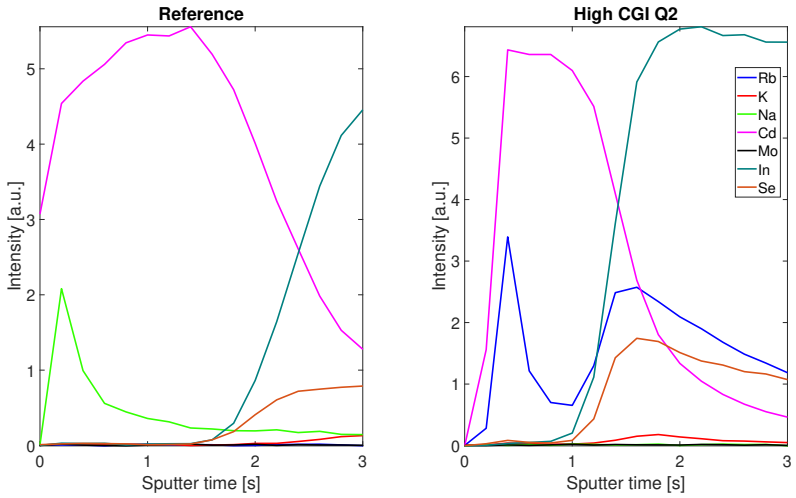

Figure 4.13: GD-OES results alkali elements, In, Se, and Cd at the front high CGI series (quadrant two), close up. The clear presence of Rb in a "U" shaped profile inside the CdS buffer layer, lower intensity of Rb detected after the buffer layer compared to the results of the substrate temperature series.

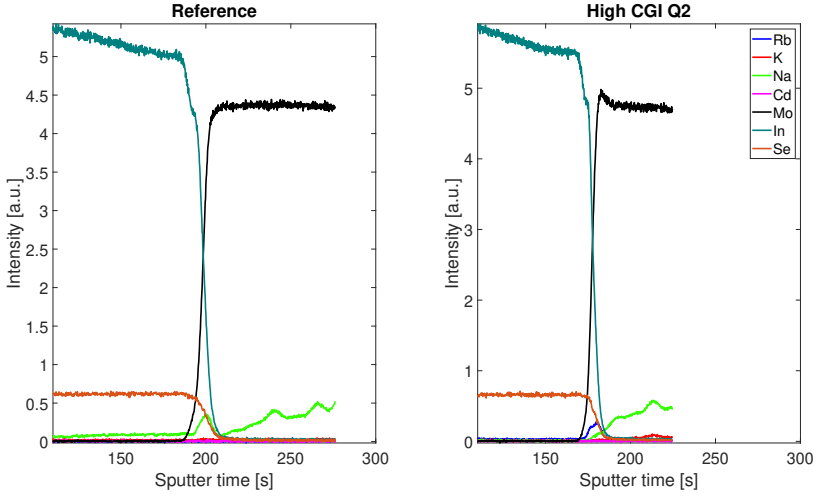

Figure 4.14: GD-OES results alkali elements, In, Se, and Cd at the back high CGI series (quadrant two), close up. Similar results to the temperatures series, smaller alkali elements (K, Na) are pushed out by the Rb.

Comparing the distribution of the alkali at the front interface (Figure 4.13), the signal of Rb inside the buffer layer has two peaks with similar intensities, but shortly after the buffer layer, the Rb intensity decreases rapidly. This can be explained by the lower amount of OVC present in the surface of the absorber, thus lower Rb adhesion and overall

lower concentration and diffusion of it. On the back of the sample (Figure 4.14), accumulation of both Na and Rb is identified, with Na reporting lower intensities if the Rb intensity is bigger (ion exchange mechanism).

4.2.4. BUFFER LAYER VARIATIONS

The last set of samples to be analyzed is the one in which different rinsing techniques prior to the deposition of the CdS buffer layer were implemented. The intention of this set of samples is to test different methods to clean the surface of low band-gap PDT samples. Since on previous high band-gap PDT samples (Appendix A), it was noted that different electrical performance can be obtained by changing the rinsing technique. Therefore, Table 4.10 shows the different procedures implemented for rinsing this set of samples.

Table 4.10: Buffer layer variation set overview.

Sample	Quadrant	Substarte Temperature [°C]	Capping layer stage duration [min]	RbF stage duration [min]	Annealing stage duration [min]	CdS description
210624_2	1	-	-	-	-	No rinse. 5:15 min deposition
210802_1	1	360	1	10	20	NH_3 (Wet), 4:00 min deposition
210802_1	3	360	1	10	20	NH_3+N_2, 4:00 min deposition
210401_1	1	360	1	6.5	20	NH_3+H_2O+N_2, 3:30 min deposition
210401_1	3	360	1	6.5	20	NH_3+N_2, 3:30 min deposition
210805_1	1	360	1	10	20	No rinse, room temperature CdS 14:40 min deposition

Table 4.11 shows the different compositions for the 5 different variations of rinsing procedures and CdS deposition times. The set of samples is selected with the aim of having similar CGI, GGI, and thickness in order to be able to distinguish clearly on Raman the impact of the different rinsing procedures, CBD and PDT implemented on them. It is worth mentioning that the XRF is measured prior rinsing the samples.

Table 4.11: Buffer layer variation set XRF results.

Sample	Quadrant	Average CGI [-]	CGI non uniformity [%]	Average GGI [-]	GGI non uniformity [%]	Avergae thickness [μm]	Thickness non uniformity [%]
210624_2	1	0.89	8.3	0.07	9.8	2.28	8.2
210802_1	1	0.87	5.7	0.06	7.5	2.13	5.2
210802_1	3	0.88	5.3	0.06	4.9	2.13	5.4
210401_1	1	0.87	4.3	0.08	7.0	1.96	3.4
210401_1	3	0.87	3.9	0.08	6.7	1.93	5.4
210805_1	1	0.89	5.6	0.06	7.1	2.20	3.7

Figure 4.15 presents the multiple Raman spectra obtained. In the first place, a clear difference can be observed with the sample rinsed with NH_3+H_2O+N_2 in which the intensity of the OVC peak at 150cm^{-1} is negligible compared to the sample rinsed with

NH_3+N_2, considering that both samples have the same PDT, CGI, and CdS deposition time, oxygen from the water molecules might occupy the Cu vacancies, oxidizing the surface and reducing drastically the electrical performance (Section 4.3.3). In contrast, samples rinsed without water show a similar response despite the rinsing procedure used, except for a clear outlier in the sample rinsed with NH_3+N_2 and 4:00 minutes CdS deposition, where a large intensity can be observed in the OVC region. After fitting the data to the Gauss model this cell also displayed a larger CIGS A1 width compared to the others, thus the large intensity of the OVC can be correlated with a lower Cu content on this specific cell and not to the rinsing procedure performed on it.

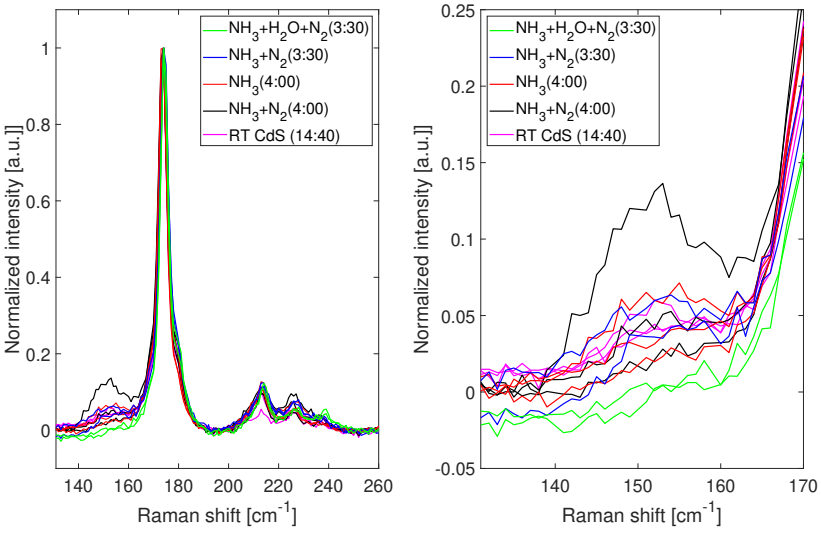

Figure 4.15: Buffer layer variations series Raman spectra. With the reduced InSe capping layer deposition, lower OVC intensities are observed.

Figure 4.16 shows the fitted results of the different cells measured by Raman, in addition to what it was observed previously the sample rinsed with NH_3+H_2O+N_2 show the emergence of a third peak at 240 cm^{-1} which the other cells do not show. Comparing the different spectra from 135 cm^{-1} to 170 cm^{-1} a reduction in the OVC peak can be noticed for the sample with RT CdS and sample rinsed with NH_3+N_2 (3:30) which contain a different RbF deposition (210401_1).

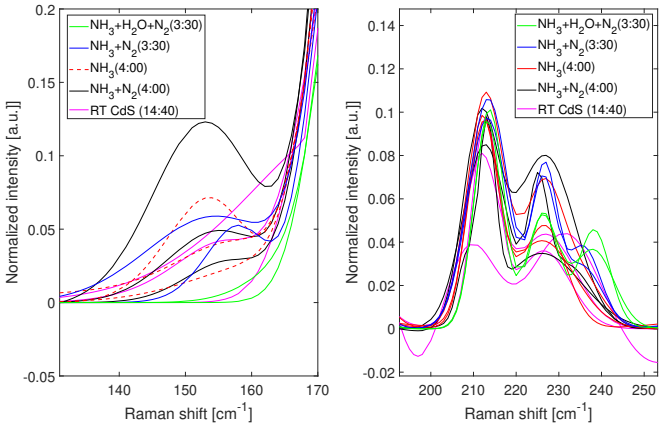

Figure 4.16: Buffer layer variations series Raman fitted spectra results, on the OVC region the different spectra show similar results, however, a 3 peak is identified between 200cm^{-1} and 250cm^{-1}.

From the different buffer layer variations implemented, only sample with RT CdS (210805_1) was analyzed by GD-OES. Figure 4.17 shows the distribution of the non alkali elements of this sample, the reference sample, and sample 210625_1 (Substrate Temperature variations 360°C). As expected a noticeable Cu depletion is created in the surface of the PDT sample by the introduced capping layer, nonetheless on sample 210805_1 the Cu depletion is larger despite of the reduced capping layer thickness, but this also leads to a surface extremely poor of Cu, In and Se (0 to 1s). Moreover, the Se peak present after 1.5s decrease more intensely comparing samples 210805_1 (RT CdS) and 210625_1 (NH_3+N_2 from the temperature series). After the first 3s, no clear differences can be identified in the distribution of the non-alkali elements.

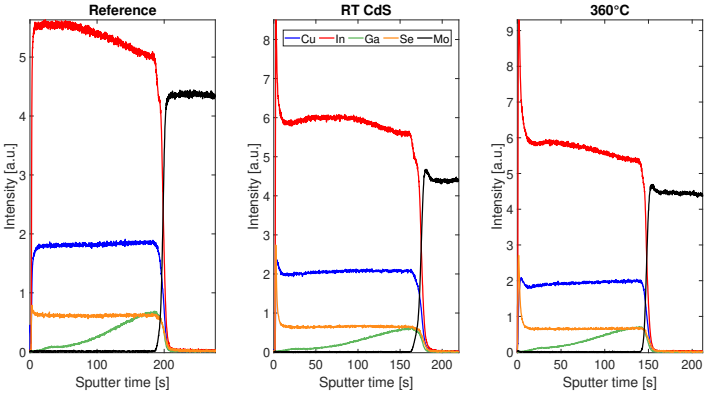

Figure 4.17: GD-OES results for the Buffer layer variations. Reference, RT CdS deposition and 360°C Substrate temperature variation sample (210625_1), distribution of non-alkali elements. Similar results for the PDT samples, large In and Se peaks, with small Cu migration towards the front of the samples. Sample 210625_1 shows a larger intensity for the In peak as a consequence of the longer InSe capping layer deposition.

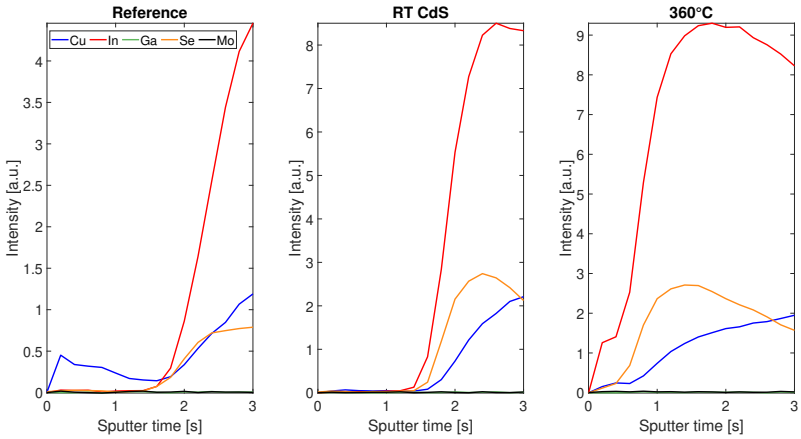

Figure 4.18: GD-OES results for the Buffer layer variations. Reference, RT CdS deposition and 360°C Substrate temperature variation sample (210625_1), non-alkali elements, close upfront. RT CdS sample show a clear Cu and Se depleted surface, while sample 210625_1 the Cu depletion is also accompanied by the presence of In and Se.

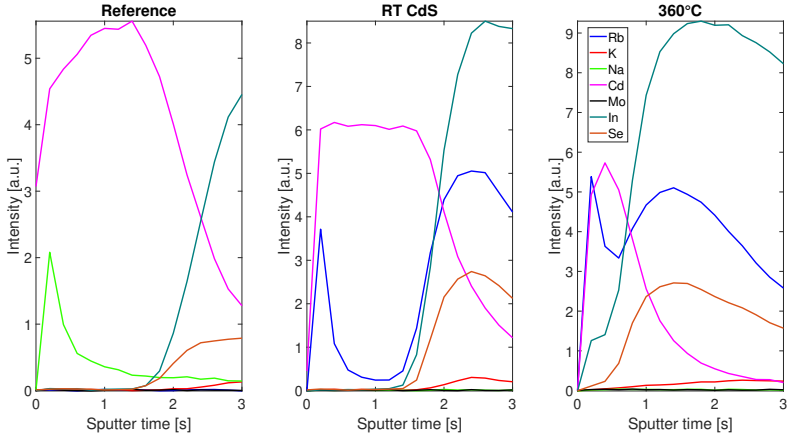

Figure 4.19: GD-OES results for the Buffer layer variations. Reference, RT CdS deposition, and 360°C Substrate temperature variation sample, alkali elements, Cd, In, Mo close up front. Similar "U" shaped profiles for the Rb distribution inside the CdS buffer layer, however, samples with RT-CdS show lower content of Rb throughout the CdS layer. After the CdS, similar Rb intensities and profiles are noticed. Additionally, RT CdS do not show the presence of In or Se inside the CdS buffer layer.

On the other hand, Figure 4.19 shows the distribution of the alkali elements together with the Cd, Mo, In, and Se. The first thing that can be examined is the thickness of the buffer layer of the multiple samples, where the reference and sample 210805_1 exhibit similar thickness while sample 210625_1 show a reduced one. The next relevant thing is the intensity of Rb inside the CdS buffer layer. In both PDT samples behave similarly hav-

ing a "U" shaped profile, though on sample 210805_1 (RT CdS) this "U" shaped profile is deeper and the intensity of Rb decrease by 4 units, while on 210625_1 it only decreases by 1.5, and a clear presence of In is noted at the surface of the absorber, presumably as a consequence of the different RbF and InSe capping layer deposition duration.

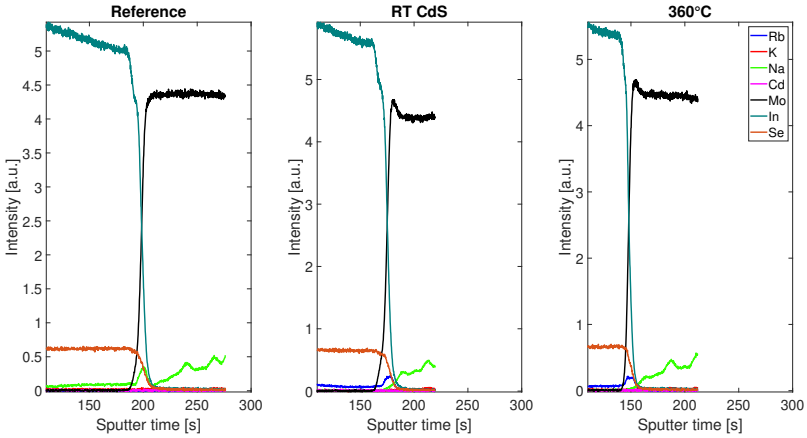

Figure 4.20: GD-OES results for the Buffer layer variations. Reference, RT CdS deposition, and 360°C Substrate temperature variation sample, alkali elements, Cd, In, Mo close up back. Similar results to the previous samples, Rb pushes out smaller alkali elements inside the Mo.

Lastly, the distribution of alkali elements at the back of the absorber for both PDT samples behaves similarly where Na is pushed out replaced by Rb (Figure 4.20).

4.2.5. CONCLUSIONS

After the different material characterization techniques were performed, remarkable differences in the different sample sets were noticed. With the use of Raman spectroscopy, the determination of OVC present at the surface of the CIGS were observed and correlated with the InSe capping layer deposition duration, in which for longer capping layer deposition a larger amount of OVC are created except on the high CGI variation sample, where no Cu depletion was seen in spite of the deposited InSe capping layer. Furthermore, the distribution of the elements throughout the absorber was identified with the help of GD-OES, it can be concluded that with a thicker (2 minute deposition) InSe capping layer an increased migration of Cu, and Se towards the front interface is created. Whereas on thinner (1 minute capping layer deposition) the ideal Cu depletion is created without the migration of other elements.

With respect to the alkali elements distribution, it was noted that they are present inside the CdS buffer layer regardless of the rinsing procedure performed on them. Also, significant changes in the profile of the Rb distribution and intensity at the front of the samples were observed by changing the duration of the second stage where for longer deposition times the "U" shaped profile shows a deeper response. While by changing the substrate temperature during the Rb deposition, the diffusion of the Rb after the buffer layer shows slight variation. Finally, it was noted that accumulation of Rb and

Na takes place in the Mo back contact where the ion exchange mechanism becomes evident (as well as in the surface of the solar cells) and smaller alkali elements (Na) are replaced by heavier (Rb) ones. Overall, no other notable changes are observed in the Ga, Se, Cu, and In distribution on the solar cells, indicating that the PDT is only responsible for modifying the surface of the absorber.

4.3. ELECTRICAL PERFORMANCE OF THE SOLAR CELLS

Following the material characterization of the samples, it is also essential to evaluate the electrical performance of each of the sets. To do this, depending on the data set different electrical measurements were conducted on them.

This Section will be divided similarly to the material characterization section. Depicting an overview table with the description of the PDT variables, CdS description, and average of the best 2 cells electrical parameters (LIV and DIV) for the best quadrant. In addition, different box plots comparing the best quadrants will be shown to give a broader overview of the performance of the samples.

The set which attracted the most attention was the temperature series, in which clear improvements were observed in the recombination current but a large loss in V_{OC} was still observed, in an effort to understand why is this happening, variable irradiance measurements and light dependent measurements were performed.

After analyzing the results, it was observed that a possible photoactive barrier might be present in the top interface between the CdS/CIGS layers. Thus, the buffer layer variations set in which CdS was deposited starting from room temperature was also analyzed by variable irradiance measurements and light dependent measurements in order to observe possible differences, and compare the different CdS deposition techniques. Regarding the capping layer variation and CGI variation sets, only the standard electrical measurements were performed on them.

To conclude and make a clear correlation between the material properties and electrical performance observed from each set, multiple plots with the CGI, OVC intensity, light, and dark IV parameters will be presented from the measured cells in the different characterization techniques used.

4.3.1. TEMPERATURE SERIES

On Table 4.12 the description of the implemented substrate temperatures, PDT variables, and CdS deposition techniques can be observed, Table 4.13 shows the average electrical performance of the best two cells from the best quadrants, and Figure 4.21 shows the distribution of all the measured cells. Remarkably, FF, J_0, and n1 of the PDT solar cells show improved parameters compared to the reference sample. However the V_{OC} is almost 20-30 mV lower compared to the reference sample, and thus η too.

Table 4.12: Substrate temperature series overview.

Sample	Substarte Temperature [°C]	Capping layer stage duration [min]	RbF stage duration [min]	Annealing stage duration [min]	CdS description
Reference	-	-	-	-	No rinse. 5:15 min deposition
210625_1	360	2	6.5	20	NH_3+N_2 rinse. 3:30 min deposition
210706_1	350	2	6.5	20	NH_3+N_2 rinse. 3:30 min deposition
210708_1	340	2	6.5	20	NH_3+N_2 rinse. 3:30 min deposition

Similar to the literature, the different temperatures used during the PDT result in variations of the electrical performance of the solar cells. Figure 4.21 gives a broader overview of the variation in electrical performance. On one hand, FF, J_0 and n1 are the parameters that are mainly affected by changing significantly, while the V_{OC} is approximately similar regardless of the substrate temperature used.

Table 4.13: Temperature series electrical performance.

Sample	Quadrant	Substarte temperature [°C]	η [%]	V_{OC} [mV]	J_{SC} [mA/cm^2]	FF [%]	Rs [Ohm*cm^2]	Rsh [kOhm*cm^2]	J_0 [mA/cm^2]	n1 [-]
210624_2	1	Reference	15.31	532.50	39.67	72.45	1.63	502	4.63×10^{-8}	1.49
210625_1	2	360	15.08	511.50	40.06	73.60	1.32	582	2.08×10^{-9}	1.22
210706_1	4	350	13.11	505.50	37.82	68.60	1.82	582	6.68×10^{-9}	1.36
210708_1	3	340	14.07	515.50	38.55	70.80	1.88	425	5.58×10^{-9}	1.39

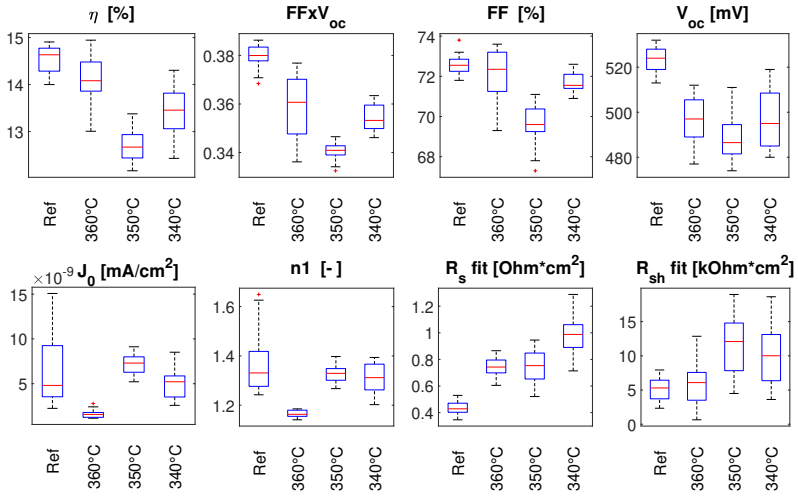

Figure 4.21: Temperature series LIV and DIV performance (best quadrants).

On one hand, substrate temperature of 360°C gives the best performance of the different substrate temperatures used. It shows a J_0 one order of magnitude lower than the reference performance, 1.15% increased FF, and a diode ideality factor closer to 1. This can be explained by the passivation of defects caused by the Rb atoms diffusing effectively throughout the absorber layer with the help of Cu vacancies. Probably explains the lower intensity observed for the OVC peak in the Raman spectra, indicating that these parameters might be correlated (discussed in Appendix C).

On the other hand, substrate temperatures of 340°C and 350°C show decreased electrical performance. A clear inconsistency can be observed, the data set does not follow the expected trend of lower electrical performance for lower substrate temperatures. This can be caused by the different processing of sample 210706_1 (explained in Section 4.2.1). Despite of this, comparing the Raman OVC and GD-OES intensities and element

distribution, larger OVC peak intensities together with a steeper reduction of Rb intensities are observed for lower substrate temperatures, where a lower amount of Rb was successfully diffused. Arguably explaining the variations in J_0, diode ideality factor, and particularly FF.

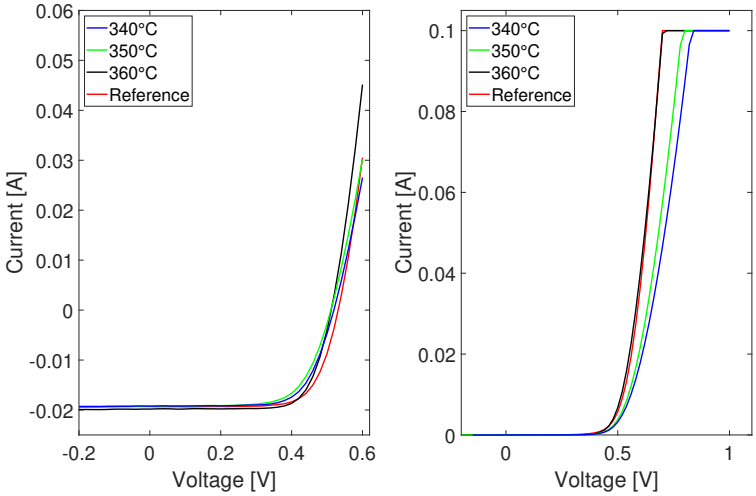

Figure 4.22: Temperature series LIV and DIV curves best cells.

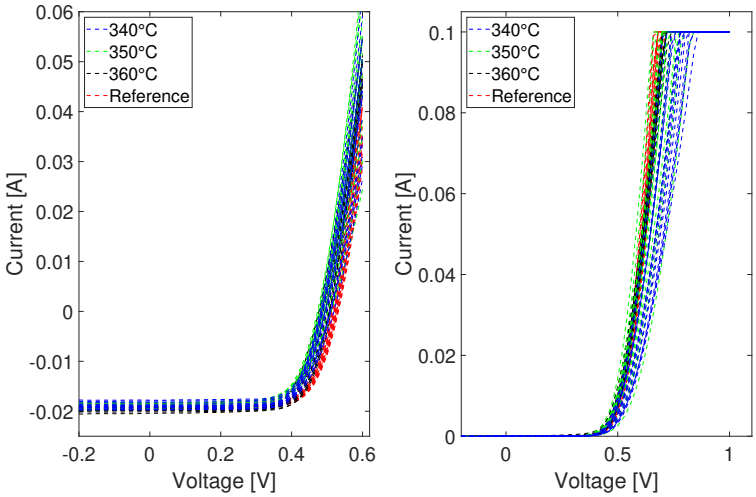

Figure 4.23: Temperature series LIV and DIV curves of all cells for the best quadrants.

Despite the fact that the PDT solar cells show better performance in most electrical parameters, the V_{OC} of the solar cells is not improving but degrading substantially. In an

effort to explain the lower V_{OC} observed for the PDT solar cells the LIV and DIV curves of them were analyzed to observe the presence of possible distortions that might help to explain the large reduction in V_{OC} observed. Figure 4.22 shows the different LIV and DIV curves for the best cells and Figure 4.23 shows the LIV and DIV curves for all the cells of the best quadrant, but in none of the cases, the clear presence of rollover behavior or kinks are observed. The largest difference can be seen on the DIV curves of 350°C and 340°C where a large voltage is needed to achieve the same current as of the reference and 360°C samples.

Subsequently, a comparison between the LIV and DIV curves for the best cells and 3 random cells was performed with the aim of identifying possible crossovers between the curves and thus correlating it with the presence of a photoactive barrier as described in [5].

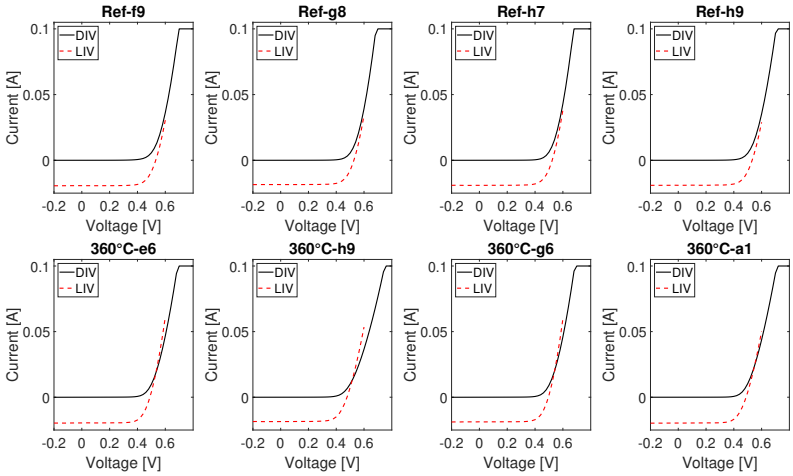

Figure 4.24: Temperature series LIV and DIV curves for crossover comparison, part 1.

Figure 4.24 and 4.25 show the curves of the reference and 3 different substrate temperatures used. Distinctively PDT cells show crossover of the DIV and LIV curves which becomes more apparent for lower substrate temperatures whereas the reference sample does not. In some cases (cell 360°C-h9, 350°C-g6, 340°C-n7) these crossover is located at lower voltages, while in other cases (cell 360°C-e6, 350°C-k8, 340°C-a6) is at higher voltages. With the results obtained it can be stated that a photoactive barrier is present in the conduction band of the solar cells and in some cases, this barrier is larger than in others creating a bigger V_{OC} drop [5].

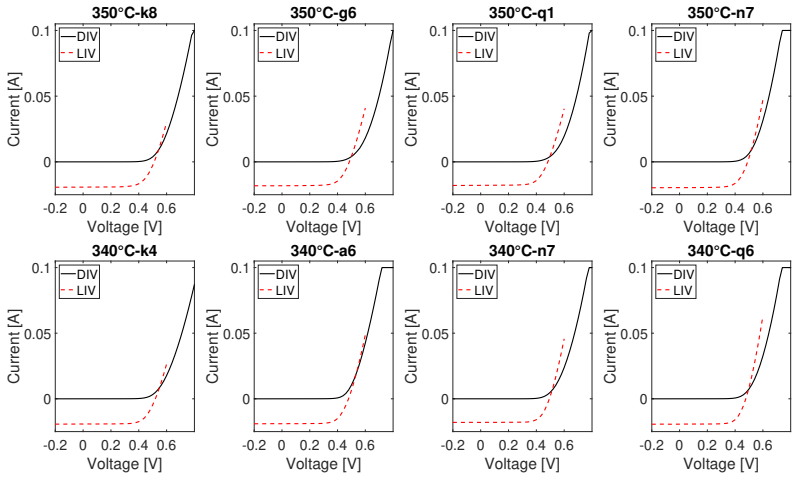

Figure 4.25: Temperature series LIV and DIV curves for crossover comparison, part 2.

To be able to quantify the drop in the V_{OC} created by the photoactive barrier and evaluate the possible location (top or bottom interface) of the barrier, two different measurements were performed; the first one known as variable irradiance measurements (VIM), in which the cell electrical parameters are measured under different irradiance intensities, and the second one is the characterization of the solar cells under different light spectra (blue and infrared).

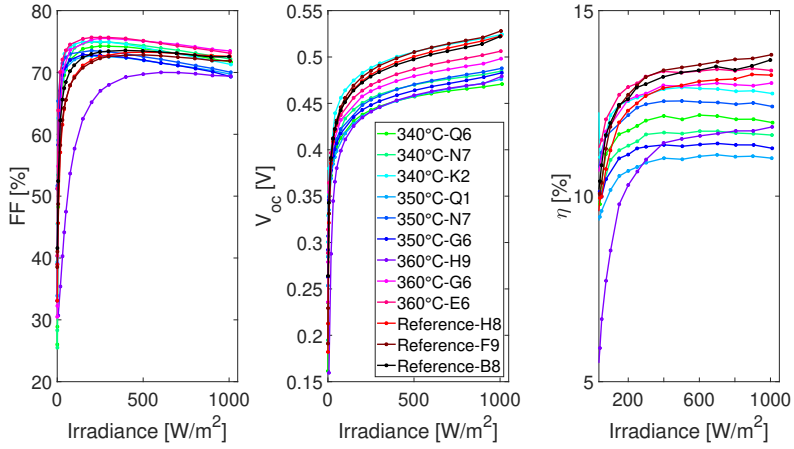

Figure 4.26: VIM results, for selected cells from the temperature series.

Figure 4.26 shows the evolution of FF, V_{OC}, and η under different irradiance levels. It compares the reference sample and the multiple substrate temperatures used. On the leftmost figure the evolution of FF is displayed, ideally, the FF should not change drastically upon different irradiance levels. The reference sample shows this behavior, while the PDT multiple cells show significant changes in FF especially when they are subjected to lower irradiance. This is because of the lower current generated and thus lower electrical losses ($P_{loss} = I^2R$) obtained when the current is flowing across the solar cell. Considering that the current is similar for the different cells at the same irradiance, the only parameter that can be causing this reduction in FF is a larger series resistance, created by an increased barrier height. This barrier height change upon illumination and thus different FF are obtained (Figure 4.29). Unlike the FF, the V_{OC} increases logarithmically with the irradiance and for both reference and PDT solar cells, a similar trend is observed. Lastly, the efficiency is directly proportional with the FF, V_{OC} and J_{SC}, therefore the multiple changes in the parameters will be reflected on the efficiency curves.

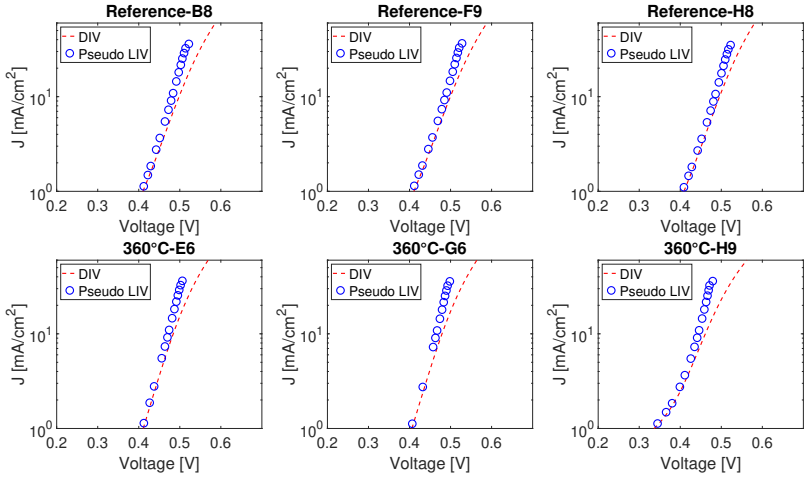

Figure 4.27: VIM results for reference and 360°C temperature series comparison between DIV and Pseudo LIV.

One approach to quantify the loss in V_{OC} created by the barrier is to calculate the pseudo IV curve in which the effect of the series resistance is neglected (explained in more detail on Appendix E). Figure 4.27 and Figure 4.28 shows the obtained DIV and reconstructed LIV curves, Table 4.14 shows the obtained parameters. Clearly in the PDT solar cells that have the largest discrepancy between the curves at higher voltages, the presence of the barrier contributes to a loss in V_{OC} of more than 60 mV, especially in the cells with 350°C and 340°C substrate temperatures.

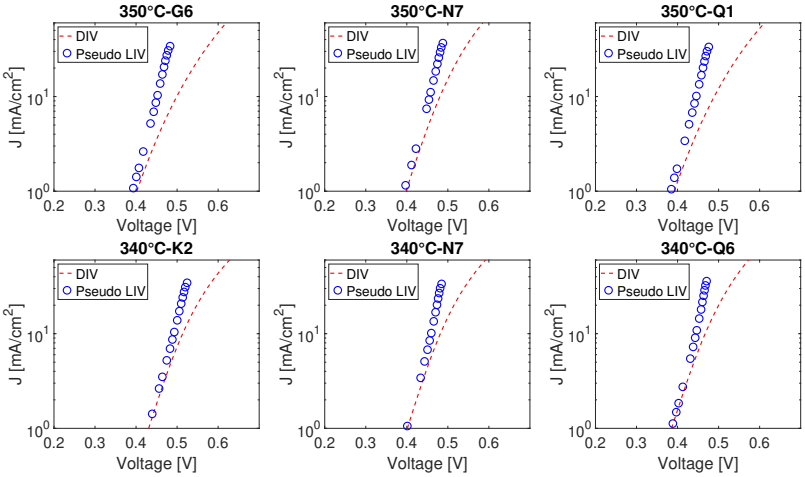

Figure 4.28: VIM results for 350°C and 340°C temperature series comparison between DIV and Pseudo LIV.

Table 4.14: Temperature series V_{OC} loss and FF slope quantification.

Sample	Cell	J_{SC} [mA/cm^2]	V_{OC} [mV]	V_{OC} loss [mV]	Slope FF	GOF FF
Reference	B8	36.07	522.01	34.23	-1.94×10^{-3}	0.952
Reference	F9	36.57	528.08	30.53	-1.74×10^{-3}	0.925
Reference	H8	35.09	522.67	27.94	-1.19×10^{-3}	0.908
360°C	E6	36.30	506.28	32.91	-3.93×10^{-3}	1.000
360°C	G6	35.83	498.22	35.46	-3.15×10^{-3}	0.993
360°C	H9	36.04	479.15	46.55	-7.69×10^{-5}	0.004
350°C	G6	34.07	482.95	91.63	-4.96×10^{-3}	0.990
350°C	N7	36.70	487.79	61.23	-4.85×10^{-3}	0.998
350°C	Q1	33.43	476.06	88.24	-4.22×10^{-3}	0.997
340°C	K2	34.49	524.36	57.97	-5.32×10^{-3}	0.999
340°C	N7	33.58	484.74	61.48	-4.14×10^{-3}	0.994
340°C	Q6	35.92	470.79	63.80	-4.05×10^{-3}	0.992

To identify the location of the barrier present on the PDT solar cells, light dependent measurements were performed. Figure 4.29 shows the change of FF and V_{OC} when different spectra of light are used. The main difference observed is in FF (similar to VIM results) comparing red and blue light. On one hand, when higher energy photons are used, a larger FF is obtained. This is because the barrier height is dependent on the carrier density when the solar cells are exposed to blue light, a substantial amount of carriers will be generated at the front compared to infrared light, where the majority of carriers will be generated at the back or far away from the top interface. As a result, the doping density in the front interface is increased with blue light hence the barrier is decreased and a better FF is obtained. On the other hand, when the cells are exposed to infra-red light, a clear decrease in FF is observed thanks to the absence of carriers at the front that help reduce the barrier height thus, a lower performance when compared to

white and blue light is noted. Although it is not clear why the V_{OC} of the solar cells remains constant for red and blue light. In contrast to the PDT samples, the reference cell shows a different trend, in which the FF improves for infra-red light and degrades slightly for blue light. However, the performance is increased compared to the white light by using blue or infra-red light.

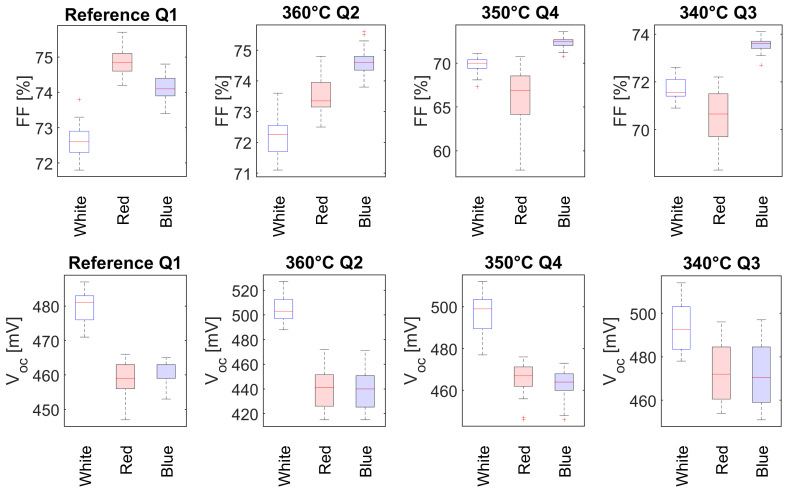

Figure 4.29: Light dependence measurements FF and V_{OC} results, best quadrants from the temperature series.

To analyze if the PDT substrate temperature has an influence on the J_{SC} EQE measurements were carried out. On literature, it is stated that thinner CdS buffer layers can be used, and thus the J_{SC} of the solar cell can be enhanced. As described in Table 4.4 a shorter and thus thinner CdS layer is deposited on the PDT solar cells. Figure 4.30 depicts the EQE of the best cells from each of the samples, a clear increase in the blue region is observed for the PDT cells thanks to the reduced thickness of the CdS, however, the absorption in the NIR is decreased, particularly for 350°C substrate temperatures. Nevertheless, the J_{SC} of the best two cells using 360°C substrate temperature is 1.5 mA/cm^2 more than the reference sample.

Table 4.15 shows the relevant parameters that can be extracted from the EQE measurements such as band-gap, J_{SC}, and projected J_{SC} in a 2-terminal tandem device. Cells from the sample deposited at 360°C show 0.012 eV smaller band-gap and V_{OC} than the reference cells despite this, the calculated V_{OC} deficit is similar to the reference cells. In contrast, samples deposited at 350°C and 340°C show a comparable band-gap to the reference cells but a substantially larger V_{OC} deficit, in connection to what is observed on the VIM measurements loss created by the barrier.

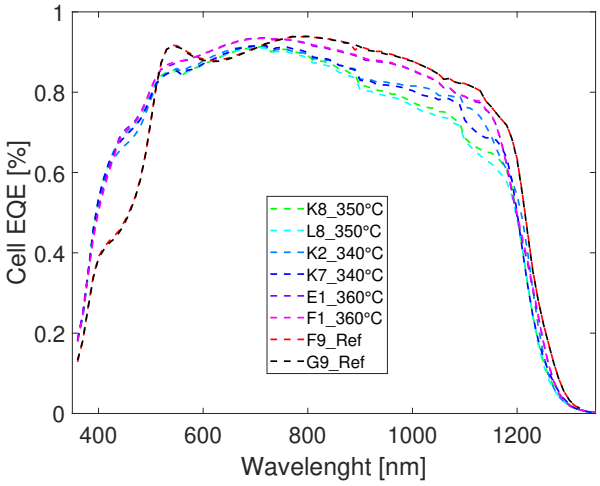

Figure 4.30: EQE results of the best cells from the temperature series and reference sample.

The potential application of the different cells in a tandem device can be calculated with the projected J_{SC}, but as the different EQE curves show the absorption in the NIR region is reduced compared to the reference cells, thereby it is essential to improve the CdS deposition in order to enhance the absorption at the NIR (discussed on Section 4.3.3).

Table 4.15: Temperature series EQE results.

Sample	Cell	Band-gap [eV]	V_{OC} [mV]	V_{OC} deifcit [mV]	J_{SC} [mA/cm^2]	Projected J_{SC} 2-Terminal [mA/cm^2]
210624_2	F9	1.02	532	484	39.70	24.24
210624_2	G9	1.02	533	483	39.65	24.23
210625_1	E1	1.00	512	488	40.05	23.42
210625_1	F1	1.00	511	489	40.07	23.46
210706_1	L8	1.02	500	516	37.67	21.97
210706_1	K8	1.02	511	514	37.97	21.70
210708_1	K2	1.01	516	492	38.61	22.65
210708_1	K7	1.02	514	511	38.30	22.45

To conclude, by using a substrate temperature of 360°C the performance of the PDT solar cells can be enhanced. Mainly, parameters like FF, J_{SC}, n1, and J_0 show improvement. However, the creation of a photoactive barrier in the top interface reduces the V_{OC} of the solar cells by more than 60 mV in most of the cases, and overall the performance of the sample is considerably reduced. This photoactive barrier is weakened upon blue light illumination thanks to the generation of carriers and change in the acceptor density at the top interface or the so called photoconductive effect. It is still unclear what is the source of this barrier since it can be the InSe capping layer and amount of OVC, accumulation of Rb at the surface, incorrect cleaning of the samples prior to CdS deposition, or possible issues in the TCO stack when samples are subjected to an RbF PDT (however in literature there no suggestion of this). In order to confront and reduce the barrier

height, different variations in the cleaning procedures prior to CdS, higher CGI samples intended to suppress the formation of OVC as well as variations in the PDT variables like duration of the RbF and InSe deposition were performed.

4.3.2. CGI VARIATIONS

Based on the results obtained in the substrate temperature series (Section 4.3.1), and capping layer variations (Section 4.2.2). Different variables of the PDT were modified, first, the substrate temperature was set to 360°C during the PDT and the RbF deposition time was extended from 6.5 to 10 minutes (reducing the flux of RbF), next, the capping layer was reduced from 2 to 1 minute but the same substrate temperature was used for its deposition (380°C), finally, two different rinsing techniques prior CdS depositions were performed and the CBD was extended from 3:30 to 4:00 minutes as it can be seen on Table 4.16.

Table 4.16: High CGI series overview.

Sample	Quadrant	Substarte Temperature [°C]	Capping layer stage duration [min]	RbF stage duration [min]	Annealing stage duration [min]	CdS description
210624_2	1	-	-	-	-	No rinse. 5:15 min deposition
210803_1	1	360	1	10	20	NH_3 (Wet), 4:00 min deposition
210803_1	2	360	1	10	20	NH_3 (Wet), 4:00 min deposition
210803_1	4	360	1	10	20	NH_3+N_2, 4:00 min deposition

Table 4.17 presents the obtained electrical performance for the high CGI sample. Compared to previously deposited samples the CGI was increased by 0.03 on quadrant 1, 0.06 on quadrant 2, and 0.02 on quadrant 4. Looking into the average values of the best two cells for different parameters and Figure 4.31, there is a big spread in performance. In contrast to what is suggested in the literature, high CGI PDT samples (>0.90) do not result in better electrical performance. In contrast, the higher CGI (0.92) sample (Q2) show the lowest performance, V_{OC}, FF and J_0 are the most affected parameters. While Q1 having a CGI of 0.90 shows a two order of magnitude better J_0, 50 mV higher V_{OC}, and 8% absolute higher FF. Comparatively, Q4 having a CGI of 0.87 shows similar J_0, FF but 10mV lower V_{OC} and 1mA/cm^2 lower J_{SC} (probably thanks to the different rinsing implemented, and not to the lower CGI).

Table 4.17: High CGI series electrical performance.

Sample	Quadrant	CGI [-]	η [%]	V_{OC} [mV]	J_{SC} [mA/cm^2]	FF [%]	Rs [Ohm*cm^2]	Rsh [kOhm*cm^2]	J_0 [mA/cm^2]	n1 [-]
210624_2	1	0.892	15.31	532.50	39.67	72.45	1.63	502	4.63×10^{-8}	1.49
210803_1	1	0.904	14.07	57.5	38.80	71.45	1.71	730	1.4×10^{-9}	1.18
210803_1	2	0.923	11.10	458.50	38.30	63.20	1.98	552	1.96×10^{-7}	1.53
210803_1	4	0.871	13.08	494.50	37.39	70.80	1.38	632	3.27×10^{-9}	1.25

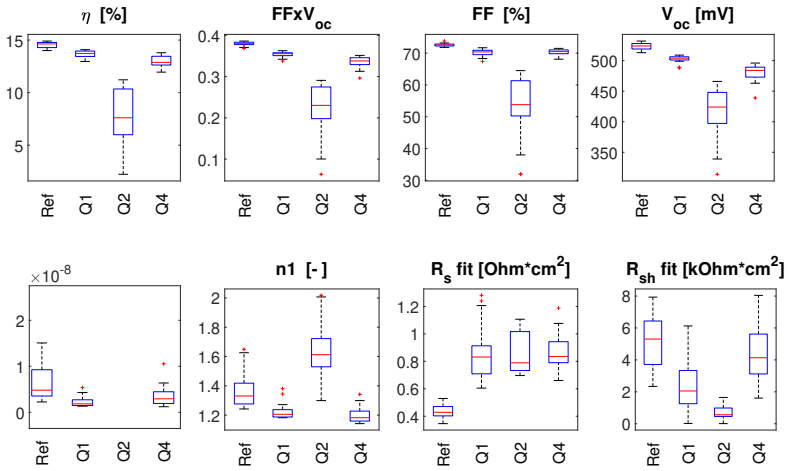

Figure 4.31: CGI variation series LIV and DIV performance (best quadrants). J_0 of Q2 not shown here, on average it is 2 orders of magnitude larger compared to the other quadrants.

One of the possible explanations for the observed lower performance on the high CGI sample (Q2) can be the non diffusion of Rb throughout the absorber (higher J_0 and n1), but instead accumulation on the surface. With the capping layer variation experiments (Section 4.2.2), it was observed that the creation of OVC is directly related to the CGI of the samples, and by reviewing the Raman spectra of Q2 (Figure 4.10) no OVC were created on the surface of the CIGS, therefore little or no Rb could adhere to the Cu vacancies for latter diffusion, this can be observed in the GD-OES results of the high CGI sample (Figure 4.13) where the intensity of the Rb signal is lower at the front and decreases rapidly as the sputter time increases.

Moreover, the LIV and DIV curves of the best cells from the different quadrants were plotted together in Figure 4.32. Meanwhile, Q1, Q4, and reference show similar behavior on LIV and DIV curves. The quadrant with higher CGI (Q2) show an increased current in the DIV curve at lower voltages making the kink in both LIV and DIV curves initiate at lower voltages (thanks to the higher J_0), this can be seen as an interface issue between the CIGS absorber and the deposited RbF layer, which could not diffuse properly, explaining the lower FF, V_{OC} and increased recombination current.

With the aim of observing if the photoactive barrier is still present after increasing the CGI of the samples, the LIV and DIV curves from the best cells of the quadrants were superimposed in Figure 4.33.

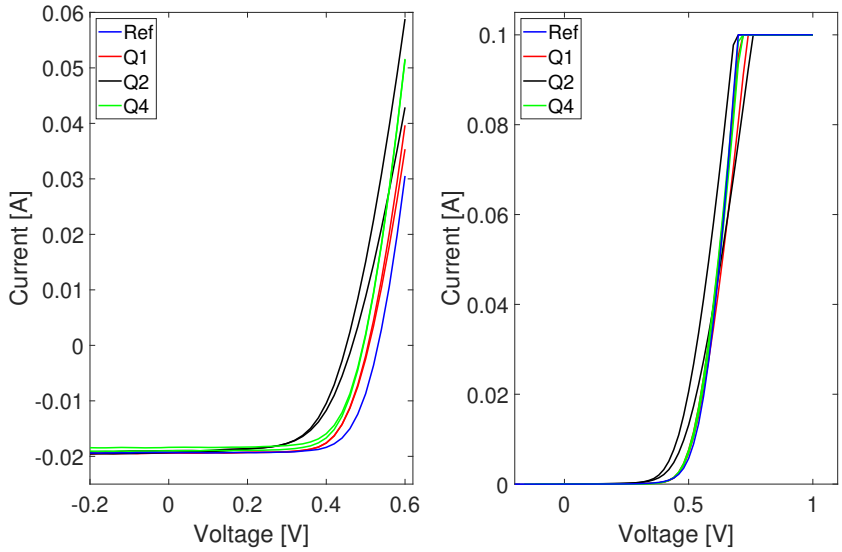

Figure 4.32: CGI variation series LIV and DIV curves comparison best cells.

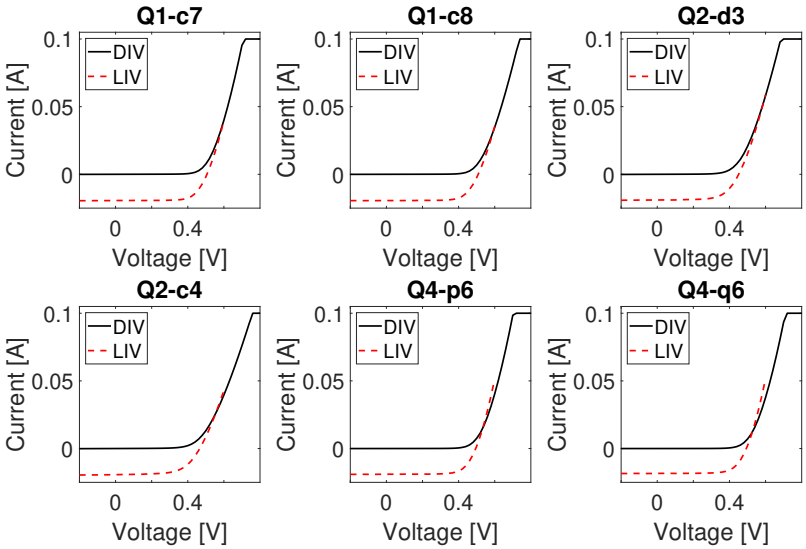

Figure 4.33: CGI variation series LIV and DIV curves crossover comparison, best cells Q1 (c7-c8), Q2 (d3-c4), Q4 (p6-q6).

The results suggest that the photoactive barrier is still present in Q4, where a small crossover can be observed. Remarkably, Q1 and Q2 show a lesser crossover, in contrast to

Q4 the rinsing procedure prior to CdS deposition implemented on the latter one, differs from Q1 and Q2. On the other hand, it can not be ruled out the lower CGI content in Q4 (CGI<0.90). For this reason, it might be possible that the appearance of the photoactive barrier occurs during the rinsing procedure implemented before the CBD of the CdS or thanks to the lower CGI of the sample. Discussed further in Section 4.3.3.

After noticing the poor performance with high (>0.90) CGI samples. It was established that the optimum CGI should be in the range of 0.85 to 0.90. Within this range, the creation of OVC in the surface is optimum with a 1 minute capping layer deposition. However, the Rb deposition might need to take place in a faster or slower manner since at 360°C In, Cu, and Na are highly movable and might affect the final distribution of them inside the different layers of the CIGS and hence the electrical performance of the sample. Intriguingly, the sample that shows a crossover between the LIV and DIV curve has similar CBD deposition procedures and CGI to the ones from the temperature series, which might indicate that the rinsing of the samples or the CGI content is responsible for the creation of the photoactive barrier.

4.3.3. BUFFER LAYER VARIATIONS

The last set of samples was prepared with the aim of evaluating different buffer layer deposition techniques and rinsing procedures. In accordance with what was observed in the previous set of samples, the suppression of the photoactive barrier is key to reduce the large reduction in V_{OC}. Furthermore, the CGI of the samples should be kept within 0.88 and 0.90 enabling the creation of the optimum density of OVC in the surface of the CIGS with the 1 minute deposited InSe capping layer, and consequently, allow proper Rb absorption and diffusion throughout the absorber. For this set, one of the first samples that were prepared is used (210401_1), this sample was prepared with a different RbF deposition duration of 6.5 instead of 10 minutes.

Table 4.18 shows the 5 different variations of rinsing procedures and CdS deposition times used for this set of samples. The different variations include changes in the CBD of 3:30, 4:00, and 14:40 minutes (starting from room T) in combination with cleaning techniques prior to CdS such as rinsing with NH_3, water, N_2, or no rinsing were implemented.

Table 4.18: Buffer layer variation set overview.

Sample	Quadrant	Substarte Temperature	Capping layer stage duration [min]	RbF stage duration [min]	Annealing stage duration [min]	CdS description
210624_2	1	Reference	-	-	-	No rinse. 5:15 min deposition
210802_1	2	360	1	10	20	NH_3 (Wet), 4:00 min deposition
210802_1	4	360	1	10	20	NH_3+N_2, 4:00 min deposition
210401_1	1	360	1	6.5	20	NH_3+H_2O+N_2, 3:30 min deposition
210401_1	3	360	1	6.5	20	NH_3+N_2, 3:30 min deposition
210805_1	1-4	360	1	10	20	No rinse, room temperature CdS 14:40 min deposition

Table 4.19: Buffer layer variation electrical performance.

Sample	Quadrant	CGI [-]	η [%]	V_{OC} [mV]	J_{SC} [mA/cm^2]	FF [%]	Rs [Ohm*cm^2]	Rsh [kOhm*cm^2]	J_0 [mA/cm^2]	n1 [-]
210624_2	1	0.892	15.31	532.50	39.67	72.45	1.63	502	4.63×10^{-8}	1.49
210802_1	2	0.890	14.05	503.50	39.86	70.00	1.69	343	1.02×10^{-8}	1.28
210802_1	4	0.865	13.98	453.50	37.67	71.95	1.37	788	1.91×10^{-9}	1.19
210401_1	1	0.870	13.17	548.00	40.39	68.40	2.16	789	8.20×10^{-8}	1.57
210401_1	3	0.870	16.24	564.50	40.17	71.60	2.27	333	3.21×10^{-7}	1.99
210805_1	3	0.914	14.85	522.50	39.38	72.20	1.77	513	2.54×10^{-8}	1.58

Table 4.19 shows the electrical performance and composition obtained with the multiple variations. The first thing that can be observed is the considerable increase in the V_{OC} for all the samples, except the one been rinsed with NH_3+N_2. Regarding FF, a large decrease in performance is noted for the sample rinsed with NH_3 and water although the J_0 is in the same order of magnitude as most of the other samples. Apart from those two samples, all the others show V_{OC} above 500 mV, FF larger than 70%, similar J_{SC} and J_0. Notably, sample (210401_1 Q3) shows a recombination current 2 orders of magnitude higher and largest diode ideality factor despite being the best PDT performing sample. Implying that first, the combination of 1 minute InSe capping layer with 6.5 minutes RbF deposition creates the optimum amount of OVC in the surface, and diffusion of RbF can take place effectively.

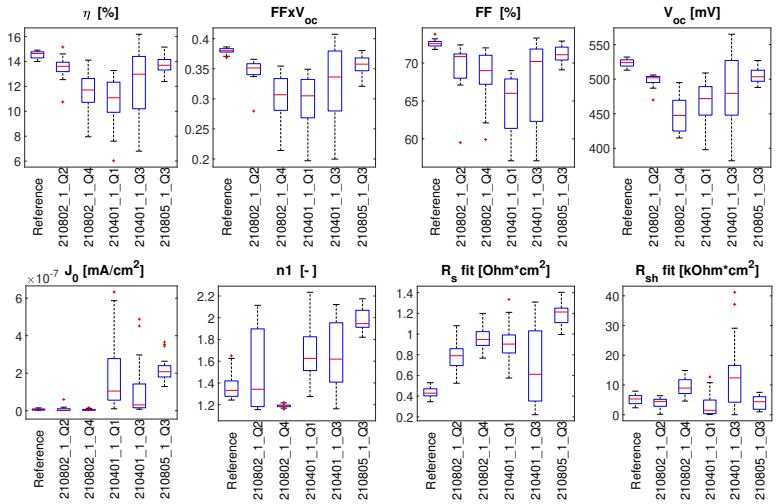

Figure 4.34: Buffer layer variation series LIV and DIV performance (best quadrants), NH_3 Wet (210802_1-Q2), NH_3+N_2 (210802_1-Q4), NH_3+H_2O+N_2 (210401_1-Q1), NH_3+N_2 (210401_1-Q3) and RT-CdS (210805_1-Q3).

Figure 4.34 shows the distribution of the electrical parameters from the whole quadrant. A big spread in all parameters can be observed for samples produced with 6.5 RbF deposition time, suggesting that probably the RbF is reaching and diffusing adequately on some cells while not on others, another reason could be insufficient coverage of the CdS thanks to the reduced CBD time (the InSe capping layer is not responsible since the

capping layer is homogeneous in all the quadrants as described in Appendix F, and the intensities of OVC are similar as discussed on Section 4.2.2).

The multiple LIV and DIV curves for the best cells can be observed in Figure 4.35. Under dark conditions, the shape of almost all curves is similar and do not show any strange kinks, rollovers, or other types of distortions, except for the sample that uses water in the rinsing procedure (210401_1 Q1) where the steepness of the curve is lower at higher bias voltages. One outstanding difference, is the start of the curve bending, in which depending on the duration of the CdS and rinsing procedure implemented, the curve bending starts at different bias voltages. First, the two samples with longer CdS deposition and ammonia rinsing, next to the samples with 3:30 minutes CdS deposition, and finally the sample with RT CdS deposition. Regarding the LIV curves, no notable difference can be observed, except for the increased V_{OC} observed for the sample rinsed with NH_3+N_2, 1 minute capping layer, and 6.5 minutes RbF deposition.

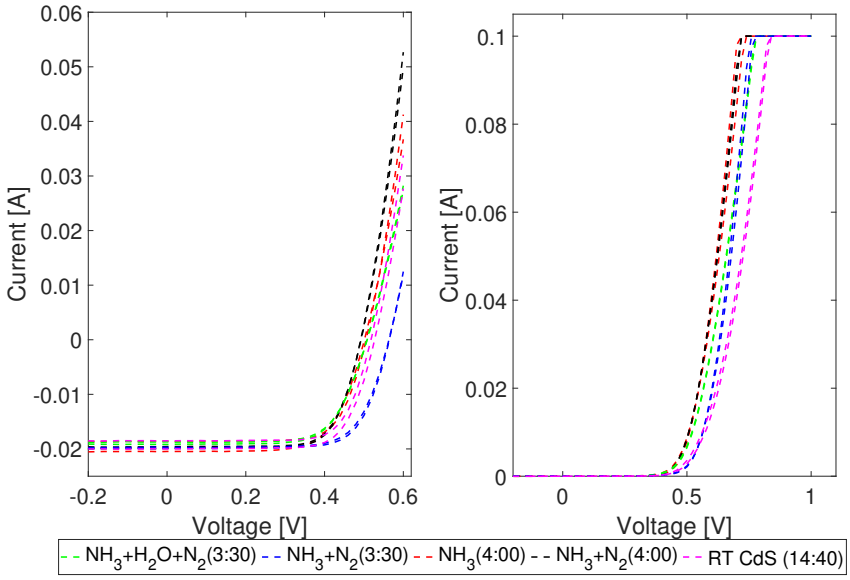

Figure 4.35: LIV and DIV curves for the best cells of the different rinsing procedures implemented.

After superimposing the LIV and DIV curves of the best cells from each of the samples (Figure 4.37 and 4.37), an evident crossover is noticed for the samples cleaned with NH_3+N_2 (21802_1 Q4), similarly, the high CGI sample (210803_1 Q4 Figure 4.33) and all the samples from the substrate temperature series (Section 4.3.1, Figure 4.24) were cleaned using the same method. Indicating that this type of cleaning promotes barrier creation at the surface, by improper deposition of the CdS created by the defective rinsing procedure implemented. Although for sample 210401_1 Q3 rinsed with the same procedure this is not observed, probably thanks to a longer rinsing implemented on this sample (performed by a different operator)

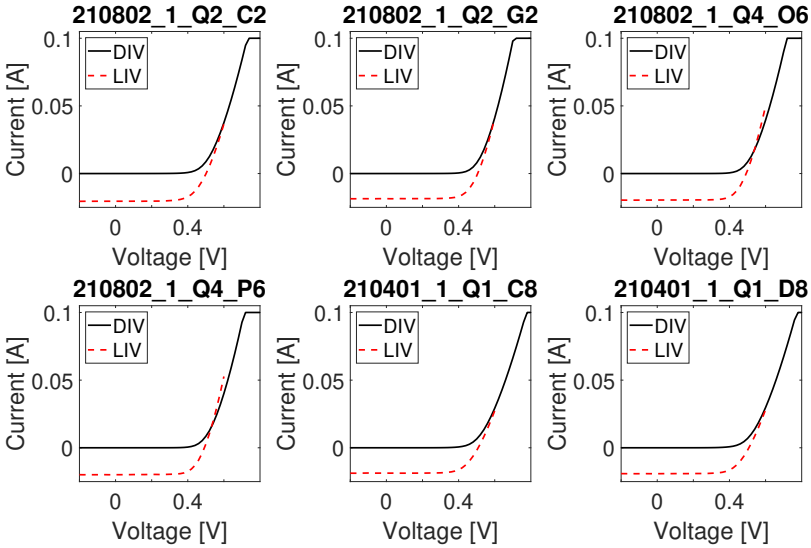

Figure 4.36: Buffer layer variation series LIV and DIV best cells crossover, NH_3 Wet (210802_1-Q2), NH_3+N_2 (210802_1-Q4) and NH_3+H_2O+N_2 (210401_1-Q1) part 1.

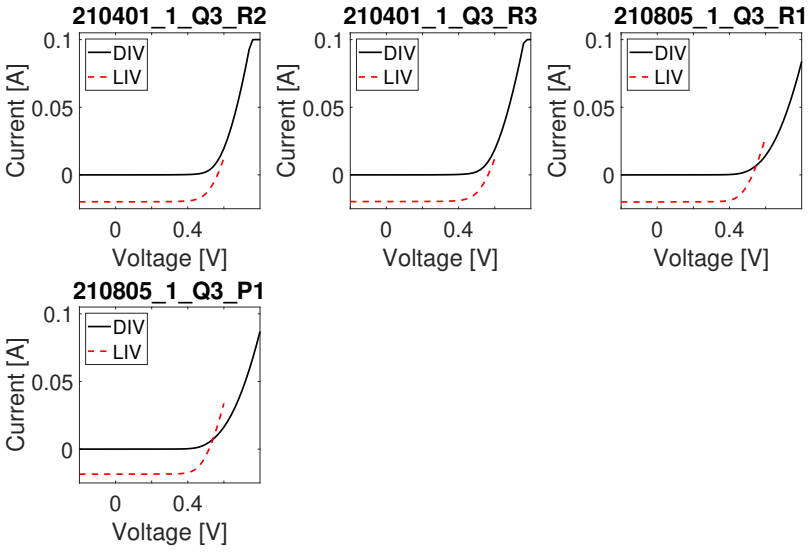

Figure 4.37: Buffer layer variation series LIV and DIV best cells crossover, NH_3+N_2 (210401_1-Q3), RT-CdS (210805_1-Q3) part 2.

Compared to these samples, the one without cleaning and deposition of CdS starting

from RT also shows a clear crossover but this time at lower bias voltages. To verify if the crossover observed on the sample with RT CdS deposition is a consequence of a photoactive barrier, VIM were performed and compared to the reference sample. Figure 4.38 shows the V_{OC} and FF variation depending on the irradiance intensity and Figure 4.39 the comparison of the obtained pseudo LIV curve with the DIV one.

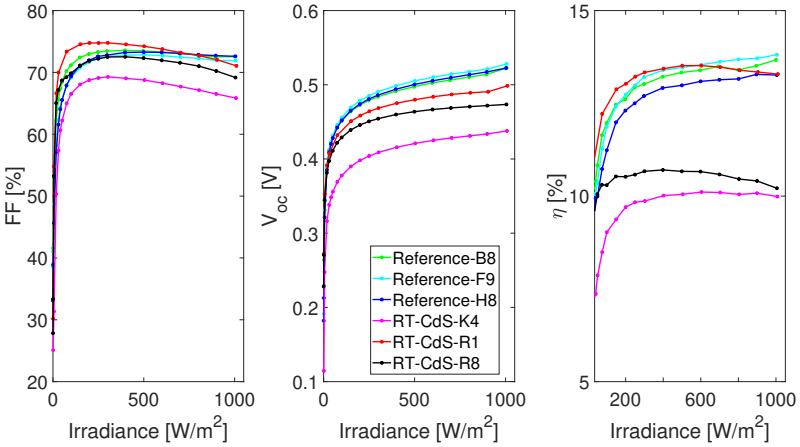

Figure 4.38: VIM results, for selected cells of the reference and RT-CdS sample.

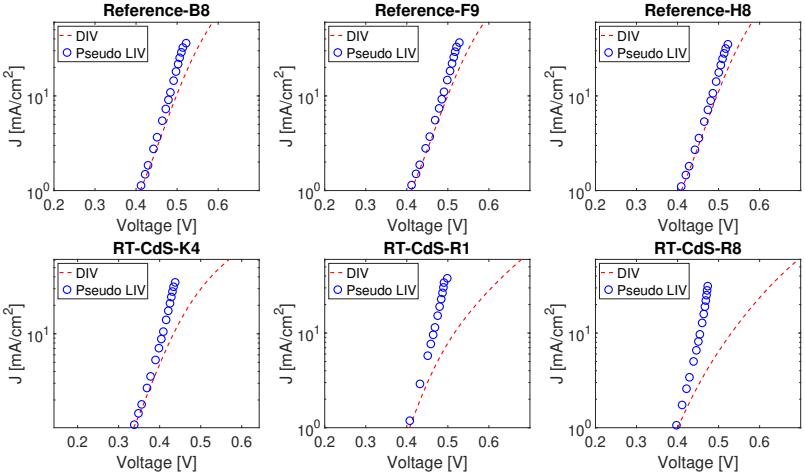

Figure 4.39: DIV and Pseudo LIV curves for reference sample and RT-CdS deposition sample.

Regarding the V_{OC} and η similar trends are observed when compared to the temperature series variation. Although for this sample the slope obtained for the FF is marginally larger, and thus it can be hypothesized that the barrier height is larger. Table 4.20 shows the quantification of the V_{OC} loss for selected cells and unequivocally it is larger, this can be also seen in Figure 4.39 where the difference between the pseudo IV and the DIV curve is significantly wider.

Table 4.20: Buffer layer variation V_{OC} loss and FF slope quantification.

Sample	Cell	J_{SC} [mA/cm^2]	V_{OC} [mV]	V_{OC} loss [mV]	Slope FF	GOF FF
Reference	B8	36.07	522.01	34.23	-1.94×10^{-3}	0.952
Reference	F9	36.57	528.08	30.53	-1.74×10^{-3}	0.925
Reference	H8	35.09	522.67	27.94	-1.19×10^{-3}	0.908
RT-CdS	K4	34.94	437.73	75.35	-5.41×10^{-3}	0.990
RT-CdS	R1	37.89	498.59	130.79	-5.59×10^{-3}	0.976
RT-CdS	R8	31.31	473.52	152.08	-5.37×10^{-3}	0.939

To evaluate the different thickness and rinsing procedures implemented, EQE measurements were performed on the best 2 cells from each of the samples, Figure4.40, and Table 4.21. Starting with the samples deposited using the different rinsing procedures and variation in the CBD, a small change in the blue region can be noted, where thicker (longer CBD) depositions result in a lower absorption namely 210802_1 (4:00 CBD) and 210625_1 (3:30 CBD). Due to low performance, no EQE was performed on the sample which was rinsed with NH_3+H_2O+N_2.

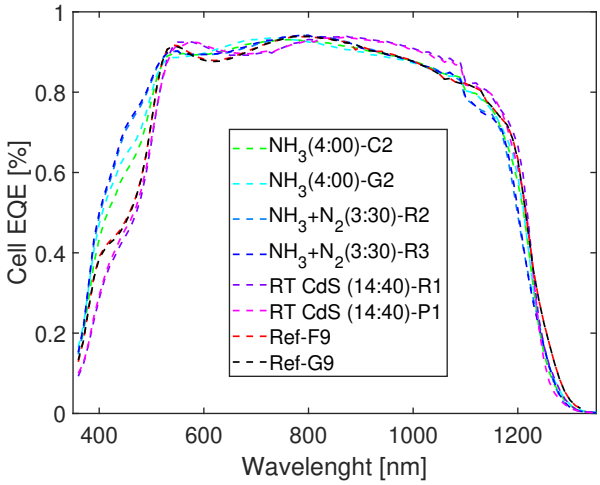

Figure 4.40: EQE results, best two cells from the different rinsing procedures implemented.

On the other hand, the sample in which CdS was deposited starting from RT, behaves similarly to the reference sample in the blue region and even better on the infrared one. Indicating that depositing CdS starting from RT for PDT cells is beneficial and even im-

proved results can be obtained in the NIR, which is important for 2 terminal tandem devices. Additionally, by comparing the different band-gaps and V_{OC} deficit obtained, the best performing sample (210401_1) and RT CdS show a remarkable low V_{OC} deficit thanks to its increased V_{OC}. Considering that the two best samples have a variation in the RbF deposition duration and that the RT CdS one provides greater absorption at the NIR while 210401_1 show more suitable absorption at the blue region and higher V_{OC}, probably the combination of 6.5 RbF deposition with RT CdS deposition will show both an enhanced absorption at the NIR and a superior V_{OC} resulting in the best combination for 2-terminal tandem devices.

Table 4.21: Buffer layer variation EQE results best cells.

Sample	Cell	Band-gap [eV]	V_{OC} [mV]	V_{OC} deficit [mV]	J_{SC} [mA/cm^2]	Projected J_{SC} 2-Terminal [mA/cm^2]
210805_1	R1	1.02	527	489	39.44	24.48
210805_1	P1	1.01	518	490	39.32	24.27
210802_1	C2	1.01	501	507	39.74	23.89
210802_1	G2	1.02	506	510	39.99	23.88
210401_1	R2	1.02	565	460	39.64	23.81
210401_1	R3	1.03	564	469	40.13	23.84
210624_2	F9	1.02	532	484	39.70	24.24
210624_2	G9	1.02	533	483	39.65	24.23

After the different variations of the buffer layer deposition and rinsing techniques were studied, multiple conclusions can be drawn. First, the cleaning of PDT samples using NH_3+H_2O+N_2 results in a large decrease in the performance of the samples mainly by reducing the FF, it is hypothesized that thanks to the presence of OVC in the surface of the CIGS, after rinsing the samples with water, oxygen occupy those vacancies and oxidize the surface of the absorber reducing drastically the performance. Secondly, using a nonoptima rinsing procedure prior to the CdS deposition promotes the creation of a photoactive barrier in the interface between the CIGS and CdS. This barrier can be identified if the samples show a crossover between the LIV and DIV curves and is responsible for creating an extra series resistance which reduces the V_{OC} of the sample by almost 100 mV in some cases. The concentration of Cu in the sample is ruled out for being responsible for the barrier formation since sample 210803_1 quadrant three with CGI>0.90 shows the crossover between the LIV and DIV curves as well as a large FF drop and V_{OC} loss on the VIM measurements.

Finally, the combination of 6.5 minutes RbF deposition and NH_3+N_2 rinsing suppresses the formation of the barrier and maximum V_{OC} can be achieved, but the duration of 3:30 minutes for the CBD only enhances the blue region response in EQE while the NIR is reduced. To overcome this limitation, depositing CdS starting from RT a large increase in the NIR can be observed and the ideal bottom sub-cell for a 2-terminal tandem can be created, achieving increased V_{OC}, J_{SC} and FF.

4.3.4. CONCLUSIONS

During the optimization of a PDT different variables play an important role in the final performance of the solar cell. Not only variables related to the PDT process but also some of them related to the steps prior or after finishing the PDT. After the different electrical characterization techniques were implemented on the produced solar cells notable differences were observed, which generally can be correlated with the CGI of the absorber, duration of the InSe capping layer deposition and RbF deposited layer, rinsing technique prior buffer layer deposition, and duration of the CBD.

Prior starting the PDT the most important variable is the CGI concentration of the absorber, in which it was identified that if the CGI is above 0.90 with the deposited InSe capping layer of 1 minute, not enough Cu vacancies are created thus Rb diffusion is hindered and it starts accumulating in the surface. To prevent this, either a longer deposition of the InSe capping layer needs to be performed (creating more Cu vacancies) or a lower CGI absorber needs to be deposited.

During the PDT two main variables can be modified, the Rb flux and substrate temperature. First, it has been noted that lower substrate temperatures reduce the Rb diffusion and result in lower electrical performance, among the different substrate temperatures used 360°C results in the most optimal one. Second, the duration of the RbF deposition also affects the diffusion. Hence, accumulation of Rb in the surface can be expected if there are not sufficient Cu vacancies for it to attach and later diffuse (related with the InSe capping layer and CGI of the sample).

Finally, after finishing the PDT the deposition of the buffer layer can affect the V_{OC} of the sample substantially, if the sample is not rinsed with the optimum NH_3 procedure, the formation of a photoactive barrier between the CIGS and CdS interface can be expected which can be responsible for reducing the V_{OC} of the solar cell by creating an extra series resistance in the layer stack, this barrier can be identified easily if there is a crossover between the DIV and LIV curves, when this crossover is at lower bias voltages the height of the barrier is larger and thus a major drop in V_{OC} can be expected.

Overall, the best sample results in a combination of CGI of 0.85, 1 minute InSe capping layer deposition, 6.5 minutes RbF deposition at a substrate temperature of 360°C, and 20 minutes annealing. Regarding the CdS buffer layer and rinsing, the use of NH_3+N_2 rinsing procedure with 3:30 CBD gives the best absorption in the blue region of the solar spectra. However, according to the results obtained, a minor modification can be performed in the buffer layer deposition, where starting the CBD from room temperature in combination with an optimum NH_3 rinsing procedure enhanced absorption at the NIR and suppression of the barrier can be achieved.

4.4. SCHEMATICS OF THE PDT

On Figure 4.41 and 4.42 the evolution of the surface and absorber during the different stages of the PDT can be observed, depending on the CGI of the sample. There are 4 important mechanisms happening during the PDT:

1. After finishing the third stage of the CIGS deposition the surface is free of Cu vacancies, the absorber grain boundaries are filled with Na coming from the SLG substrate and in the Mo large accumulation of Na takes place.

2. During the deposition of the InSe capping layer, Cu starts moving towards the surface of the absorber as the InSe is deposited on the absorber and the creation of OVC starts taking place. Meanwhile, accumulation of the deposited InSe layer and moving Cu atoms agglomerate in the surface of the absorber. Nevertheless, if the sample contains a high CGI (CGI>0.91) combined with a thin InSe capping layer (1 minute deposition), the creation of OVC is reduced. Consequently, lower Rb is diffused throughout the absorber and a thicker Rb layer is formed on the surface (Figure 4.42).

3. When the RbF deposition starts, it adheres to the created Cu vacancies and starts diffusing throughout them towards the grain boundaries.

4. Next, the Rb pushes smaller alkali elements such as Na to diffuse inside the grains and Rb replaces them at grain boundaries. In a similar manner, when Rb reaches the Mo it starts accumulating and displacing the Na present at the CIGS/Mo interface. After the Rb deposition is finished a layer with the non diffused Rb atoms is formed on the surface of the CIGS.

5. The last step is the rinsing of the samples, where depending on the method implemented larger amounts of alkali can be present at the surface. Consequently, implementation of an optimum NH_3 rinsing procedure prior to the CBD capable of reducing the amount of alkali is essential. It has been observed that when NH_3+N_2 is performed properly (sample 210401_1 Q3) excellent results can be obtained, but when is not (sample 210802_1 Q3) detrimental effects are expected.

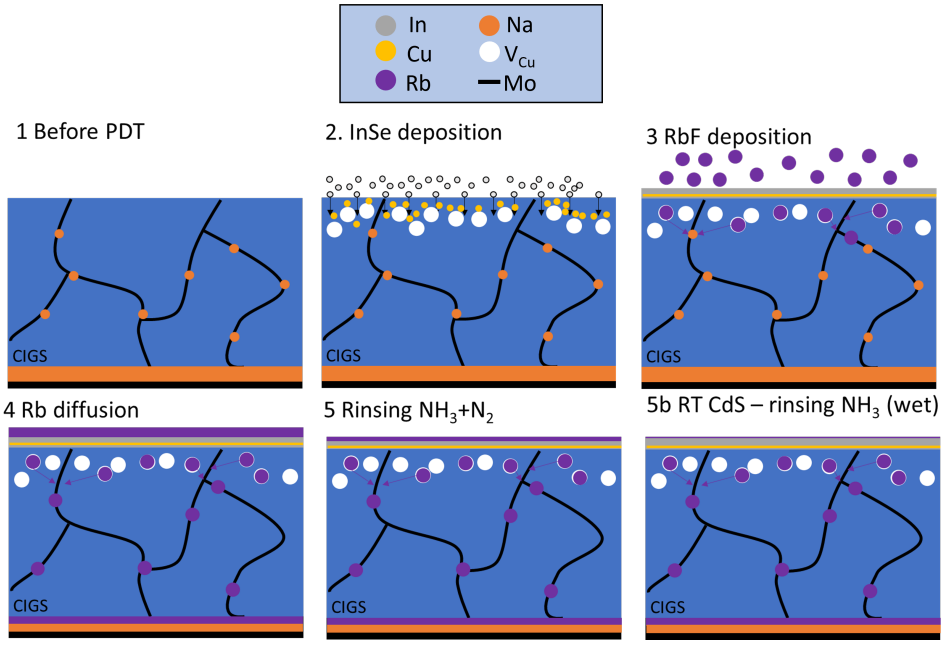

Figure 4.41: Evolution of the CIGS surface during the different stages of the PDT.

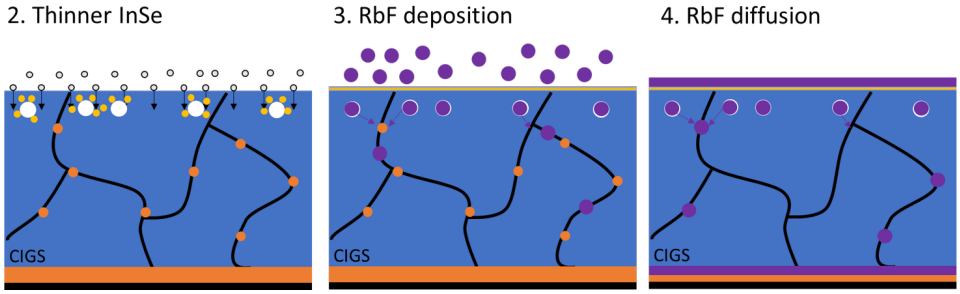

Figure 4.42: Evolution of the CIGS surface during the different stages of the PDT, high CGI sample.

REFERENCES

[1] T. Feurer, F. Fu, T. P. Weiss, E. Avancini, J. Löckinger, S. Buecheler, and A. N. Tiwari, *RbF post deposition treatment for narrow bandgap Cu(In,Ga)Se_2 solar cells,* Thin Solid Films **670**, 34–40 (2019).

[2] T. Kodalle, M. D. Heinemann, D. Greiner, H. A. Yetkin, M. Klupsch, C. Li, P. A. V. Aken, I. Lauermann, R. Schlatmann, C. A. Kaufmann, and et al., *Elucidating the mechanism of an RbF post deposition treatment in CIGS thin film solar cells,* Solar RRL **2**, 1800156 (2018).

[3] T. Kodalle, T. Bertram, R. Schlatmann, and C. A. Kaufmann, *Effectiveness of an RbF post deposition treatment of CIGS solar cells in dependence on the cu content of the absorber layer,* IEEE Journal of Photovoltaics **9**, 1839–1845 (2019).

[4] T. Kato, J.-L. Wu, Y. Hirai, H. Sugimoto, and V. Bermudez, *Record efficiency for thin-film polycrystalline solar cells up to 22.9% achieved by cs-treated Cu(In,Ga)(Se,$S)_2$,* IEEE Journal of Photovoltaics **9**, 325–330 (2018).

[5] *Appendix a: Frequently observed anomalies,* in *Chalcogenide Photovoltaics* (John Wiley Sons, Ltd, 2011) Chap. 7, pp. 305–314, https://onlinelibrary.wiley.com/doi/pdf/10.1002/9783527633708.ch7 .

5

CONCLUSIONS

The different experiments and characterization techniques used to analyze the PDT solar cells helped to understand the role of the different variables of the PDT, material properties observed and obtained electrical performance.

Starting with the material properties of the solar cells, it was identified that prior the PDT the amount of Cu, In, Ga and Na present in the absorber layer of the solar cell have a big impact on the determination of the role of the selected variables to perform the three steps of the RbF PDT. First, the content of Ga must be kept low so that the GGI<0.09, in order to obtain the band-gap between 1.00 and 1.02 eV creating the optimum bottom sub-cell for a tandem device. Alongside Ga, the Cu content of the absorber layer must be such that the CGI is within 0.85 and 0.92, preventing excess of Cu in the surface of the absorber and thus poor addition of Rb (due to the low density of OVC). Finally, the amount of In deposited during the capping layer directly correlates with the formation of the Cu vacancies which are necessary for proper Rb absorption and later diffusion. As observed, at longer capping layer deposition during the first step of the PDT more Cu vacancies are created. However if the Cu content on the surface of the absorber is rather high (CGI>0.90) their creation is limited and results in poor Rb absorption and diffusion. On the other hand, a higher density of Cu vacancies in the surface of the absorber after finishing the Rb deposition affects detrimentally the electrical performance.

Next to the material properties, the different variables of the PDT also impact significantly the final performance of the solar cell. The first important variable of the PDT is the duration of the InSe capping layer deposition. As already stated above it determines the quantity of Cu vacancies at the surface of the CIGS. For this reason, it should be chosen (prior starting the PDT) based on the CGI composition of the absorber, namely, longer for high CGI (CGI>0.92) and shorter for lower CGI (CGI<0.90). The important variables of the second stage of the PDT are the substrate temperature and the duration of the RbF deposition. Regarding the substrate temperature, lower performance was observed for substrate temperatures below 360°C at which the diffusion of Rb is hindered. As a result of the reduced Rb diffusion, significant amounts of OVC is still present in the surface. Yet another important parameter is the RbF flux. It has been calibrated to de-

posit approximately the same amount of material using 6.5 or 10 minutes. The GD-OES intensities reported similar values but different profiles of the Rb distribution, where using 10 minutes showed a more pronounced "U" shaped profile at the surface of the absorber and therefore lower amount of Rb was present at the interface between the CdS and CIGS layer. The final step of the PDT is the annealing, however this parameter was kept constant for all the experiments.

Besides this, it is important to mention that the implementation of the PDT does not modify the Ga content or distribution of it throughout the absorber depth. Hence, no variations in the band-gap are observed which is important for the design of tandem devices.

After the PDT, the optimization of the buffer layer deposition was performed. This step proves to be one of the most important ones, if not optimal a detrimental effect on the CdS/CIGS interface reducing electrical performance of the final cells can be expected particularly for the V_{OC}. The multiple variations in the rinsing prior CdS deposition, coupled with variable irradiance measurements and the observation of crossover effects in the LIV-DIV curves, helped to identify the formation of a photoactive barrier at the interface between the CIGS and the buffer layer. This photoactive barrier is creating an extra series resistance on the mentioned interface, and is responsible of reducing the V_{OC} of the solar cells, in some cases by more than 80 mV. It is suggested that the creation of this barrier is thanks to the improper rinsing of the absorber surface prior CdS deposition. Alternatively, the barrier exist due to a large accumulation of RbF in the surface layer after the PDT due to insufficient diffusion into the bulk of the absorber which can create large accumulation of alkali in the surface of the absorber.

Based on the results obtained, the best solar cells with the electrical parameters presented are described in Table 5.1 and the electrical parameters on Table 5.2. For sample 210401_1 the V_{OC} and J_{SC} improved compared to the reference sample, nevertheless the improvement in J_{SC} is obtained as a result of an increased absorption in the blue region, while for sample 210805_1 the FF is increased and the J_{SC} in the NIR is enhanced compared to baseline cell performance, making it more suitable for tandem devices. Although it was not tested experimentally, the combination of variables for the PDT used with sample 210401_1 and RT CBD might result in the ideal bottom sub-cell for 2T tandem devices, by having the excellent combination of electrical parameters; high V_{OC}, FF and enhanced J_{SC} in the NIR region.

Table 5.1: Optimum combination of variables.

Sample	CGI [-]	GGI [-]	thickness [μm]	Capping layer stage duration [min]	PDT substrate Temperature [°C]	PDT stage duration [min]	Annealing duration [min]	Rinsing technique	CBD deposition time [min]
210401_1	0.87	0.08	1.93	1	360	6.5	20	NH3+N2	3:30
210805_1	0.91	0.05	2.19	1	360	10	20	No rinsing	14:40 RT Deposition

Table 5.2: Electrical parameters best samples.

Sample	η **[%]**	$\mathbf{V}_{OC}$ **[mV]**	$\mathbf{J}_{SC}$ **[mA]**	**FF [%]**
210401_1	16.35	565	40.38	71.6
210805_1	15.15	502	39.37	72.2

To conclude, with the obtained characteristics of the best low band-gap CIGS solar cells, to be coupled with a perovskite top sub-cell, moves us one step closer to the maximum conversion efficiency of photovoltaic devices. Moreover, by understanding the role the different materials and variables play during RbF post deposition treatments, enables the scaling up of this technologies in order to be implemented massively to confront the growing energy demand.

6

RECOMMENDATIONS

Although the performance of the PDT solar cells was increased compared to the reference sample, different recommendations can be proposed for further improvements. As it was discussed on Conclusion chapter, the CGI of the absorber defines the variables to perform the PDT. Along with this variable, the rinsing technique implemented prior the CBD also proves to impact significantly on the final performance of the solar cells, by suppressing the formation of a photoactive barrier. Table 6.1 describes the optimum combination of variables to perform the PDT based on the absorber CGI composition. Based on the intensity OVC peak (obtained by Raman spectroscopy), the duration of the capping layer deposition is chosen in order to create the right amount of OVC on the surface of the absorber, allowing for proper Rb absorption and diffusion.

Table 6.1: Ideal PDT variables based on absorber composition.

CGI [-]	**Capping layer stage duration** [min]	**PDT substrate temperature** [°C]	**PDT stage duration** [min]	**Annealing duration** [min]	**Rinsing technique**	**CBD method and duration**
0.87-0.91	1	360	6.5	20	Opt. NH3	RT-14:40
>0.91	1.5-2	360	6.5	20	Opt. NH3	RT-14:40

In addition, other parameters of the PDT can be modified to evaluate their influence on the final performance of the solar cells. Some of these parameters are:

- The substrate temperature during the InSe capping layer deposition: by modifying this parameter, the Cu, In and Se can have a different distribution on the absorber surface, possibly easing Rb absorption.

- The substrate temperature during RbF deposition; with a maximum temperature of 400°C. Going towards higher temperatures can enhance the Rb diffusion, however other elements such as Ga, In and Cu might become extremely movable inside the CIGS absorber affecting their distribution.

- Duration of the annealing stage: despite of keeping this variable constant for the multiple experiments, it is important to implement variations reducing or extending the duration of this stage, in order to identify the impact it has on the electrical performance and material properties.

- Rinsing of the samples with different chemicals prior CBD. Implementation of stronger chemicals such as KCN or Ammonium possibly help to rinse effectively the excess of alkali present in the surface of the samples, allowing for proper CdS deposition and consequently preventing the formation of barriers at the CIGS/CdS interface.

With respect to the characterization techniques used to analyze the samples, other techniques that give a deeper understanding of the material properties can be implemented. Some of these techniques are:

- Atom probe tomography. Using this technique detailed information of the chemical composition can be obtained. Compared to GD-OES, higher resolution can be obtained (at the scale of grain boundaries). Can be used to detect if Rb is present at GB and is effectively passivating defects.

- Scanning electron microscopy (SEM). By using SEM on the surface of the samples, different morphologies can be identified and correlated with the presence of secondary phases. Moreover, identification of excess of alkali in the surface of the samples can also be detected.

- X-ray photoelectron spectroscopy (XPS). Using XPS, identification of the elemental composition, chemical and electronic state of the elements present in the surface of the absorber is possible. By implementing this technique shortly after performing the rinsing of the samples, modifications to the rinsing procedures can be implemented.

ACKNOWLEDGEMENTS

It all started a year ago when I started my intenrship. First of all, I want to thank my supervisor Dr. Marcel Simor for trusting in me from the first interview, where I had the opportunity to basically choose in which project I wanted to be involved in. Moreover, Marcel always encouraged me to learn from my mistakes, interpret the results in different ways, think outside the box in order to be able to understand the work of a researcher. In addition to this, I also want to thank Maarten var der Vleuten, my second supervisor at the company. Where every week the three of us together discussed the different results of the experiments carried out, we thought about how to improve the process and made important decisions. In the same way, not all discussions were always focused on scientific topics, but there was also room of discussing other topics.

Of course, I also want to especially thank Klaas Bakker and Hero Maneetje for the time they spent teaching and explaining me new things related to the different experiments performed and characterization methods used to evaluate the samples. Finally I also want to thank the entire group of researchers such as Anna, Remi, Aldo and Mirjam for the suggestions and comments, which helped me improve my experiments and my presentation skills.

On the other hand, I also want to thank Professor Dr. Olindo Isabella , who was always willing to listen and comment on the different results obtained and give suggestions on how to steer the project.

Finally, I want to thank my family and my friends from Colombia, Delft and Eindhoven who were always present to support me, listen to me and encourage me to be a better person.

A

PREVIOUS INTERNSHIP RESULTS

The aim of this chapter is to observe the performance and material properties obtained after performing RbF PDT on standard band-gap (E_g>1.1 eV) CIGS. Below, the results of the multiple characterization techniques used for the previous internship can be observed.

Figure A.1shows the different LIV and DIV parameters obtained, where similarly to the low band-gap PDT series with substrate temperatures above 330°C improvements in the J_0 and diode ideality factor are obtained, but in some cases, the V_{OC} is severely affected.

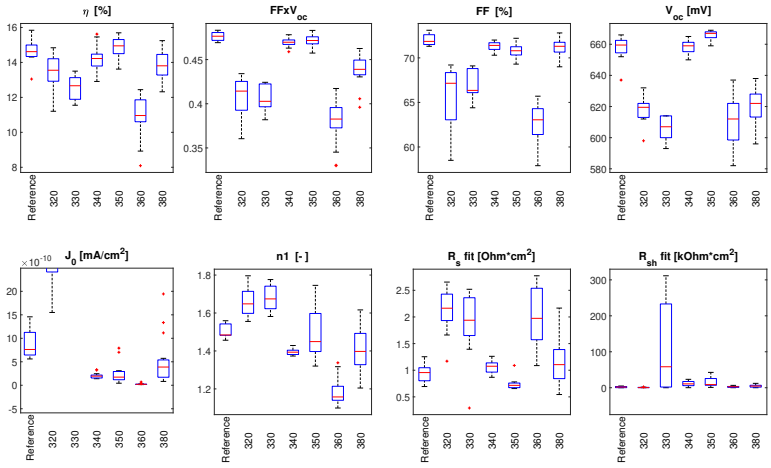

Figure A.1: Electrical performance regular band-gap CIGS.

Now, the material distribution across the depth of the solar cell for four variations of the substrate temperature can be seen in Figure A.2 and A.3 for non alkali and alkali

elements respectively. For this set of samples, peaks of In and Se can be noted at the front of the absorbers depending on the substrate temperature used. On one hand, for low substrate temperatures (320°C and 330°C) the In peak show a high atomic concentration at the front of the absorber and afterward is followed by a secondary plateau, while for substrate temperatures above 340°C, only one plateau is observed. On the other hand, the atomic concentration of Se at the front for higher substrate temperatures (350°C and 380°C) is substantially larger compared to 320°C and 340°C.

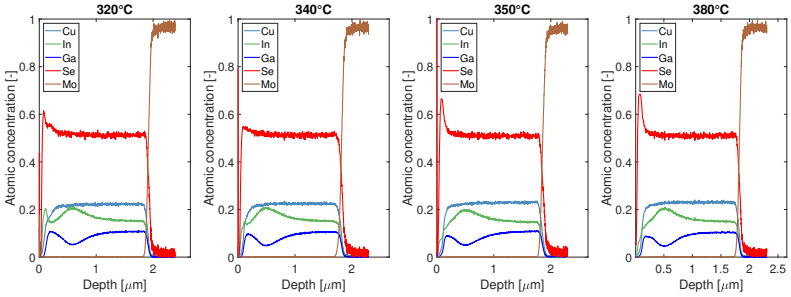

Figure A.2: GD-OES non alkali element distribution across solar cell depth.

In Figure A.3, the distribution of the alkali elements in the first 0.5μm is presented. Similar to what it is observed on the low band-gap PDT series, 330°C and 340°C show a "U" shaped Rb profile inside the CdS buffer layer, together with a depletion of Na and K.

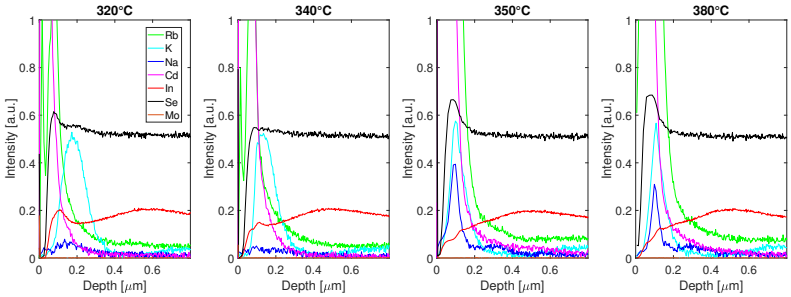

Figure A.3: GD-OES alkali element distribution across solar cell depth.

The last Figure corresponds to the Raman spectra of selected cells for the various substrate temperatures. The principal difference is observed for 320°C and 330°C, where the OVC peak becomes visible and disappears when higher substrate temperatures are used. This can be correlated with the low electrical performance reported on these samples, as well as with the In peak and Cu depletion observed on the GD-OES results at the front of the absorbers.

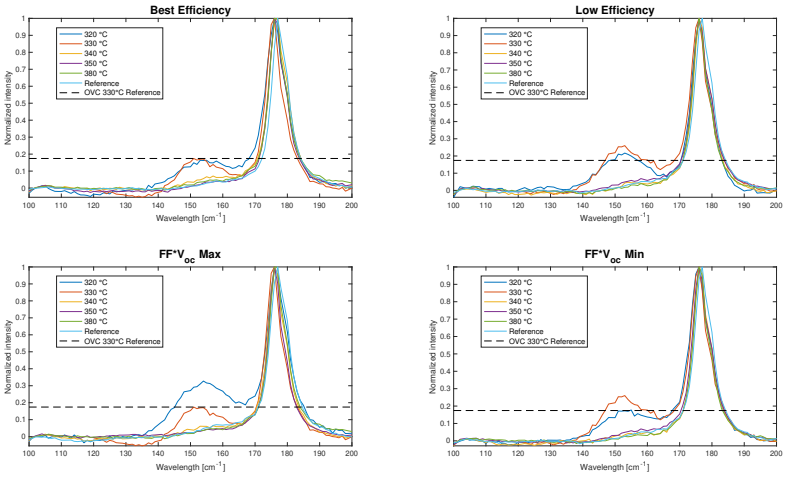

Figure A.4: Raman spectra for different cells at different substrate temperatures.

B

PDT OF AIR EXPOSED ABSORBERS

B.1. PRECONDITIONING FOR AIR EXPOSED ABSORBERS

MOST of the times, the deposition of the PDT is done directly after finishing absorber deposition without breaking the vacuum. Therefore, the samples are never exposed to air. However, with the aim of performing multiple variations on absorbers with different CGI and GGI compositions, the development of a PDT routine that enables to perform effective PDT on CIGS absorbers produced in different runs, and exposed to air is essential.

It is widely known that when bare (without buffer layer and TCO) CIGS absorbers are exposed to air and light they tend to degrade relatively easily and their performance can drop heavily [1]. In addition, the desorption of Se from the substrate also plays a key role when performing the PDT, since the substrate temperature needs to be higher than 300°C, and considering the relatively low enthalpy of vaporization of the Se. At this temperature, without having a Se rich atmosphere in the chamber, Se will start to evaporate and diffuse out from the substrate. As a result, first, a proper cleaning or rinsing procedure must be implemented to remove the oxidized material from the absorber surface (created by the air and light exposure), and along with this, the optimum Se atmosphere or pressure must be present inside the chamber when the substrate temperature is above 280°C.

In Sections B.1.1 and B.1.2 the identification of the optimum Se atmosphere and cleaning procedure for air exposed absorbers is going to be analyzed respectively. With the aim of reducing the number of variables, and being able to compare and reproduce the results, all the samples produced for the experiment are performed using a standard PDT recipe described in Figure B.1. First, an InSe capping layer is applied for a duration of 1 minute (step 1), next the RbF is deposited together with a reduced Se flux for 6.5 minutes (step 2) and finally the sample is annealed for a period of 20 minutes under the same Se reduced flux (step 3).

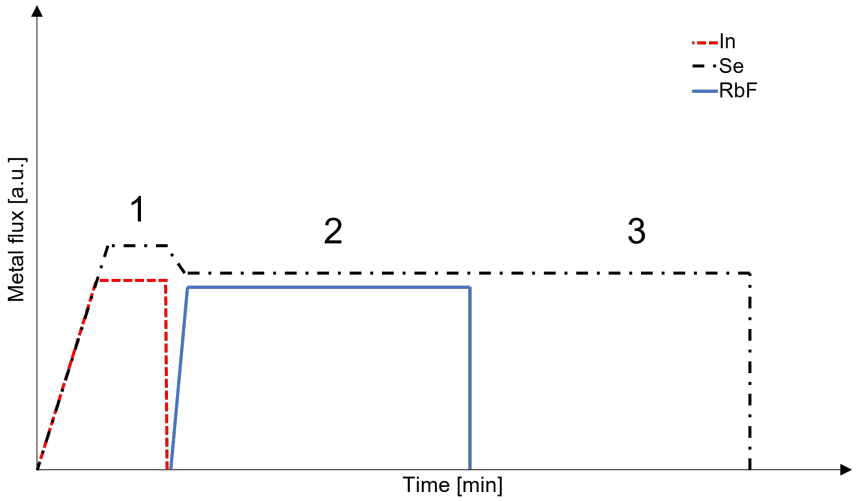

Figure B.1: Standard RbF post deposition recipe for air exposed absorbers.

B.1.1. SE ATMOSPHERE BEFORE STARTING PDT

SUBSTRATE SHUTTER CLOSED

IN order to find the optimum Se atmosphere, such that during the substrate heating the desorption of Se from the sample is prevented, three different heating profiles for the substrate were implemented. Figure B.2 and Table B.1 show the different variations used. The goal is to start the heating of the substrate at different times after the Se crucible is turned on, and therefore obtain different Se pressure inside the chamber.

Table B.1: Substrate heating times for optimum Se atmosphere closed shutter.

Sample	Se crucible start time [min]	Substrate heating start time [min]	PDT substrate temperature [°C]	PDT source temperature [°C]	Capping layer deposition time [min]	PDT duration [min]	Annealing duration [min]
1	-	-	-	-	-	-	-
2	0	25	350	565	1	6.5	20
3	0	35	350	565	1	6.5	20
4	0	45	350	565	1	6.5	20

With the aim of having a reference sample to compare the results, all the absorbers used are deposited on the same run in four substrates of 5x5 cm. One of the absorbers is finished completely (deposition of CdS and TCO) after finishing the deposition, while the other three are used for the Se experiment, bear in mind that air exposed absorbers (2, 3, and 4) have been previously rinsed with ammonia 1M before starting the experiment. Finally, after the PDT is finished on the remaining three absorbers CdS and TCO are deposited on them.

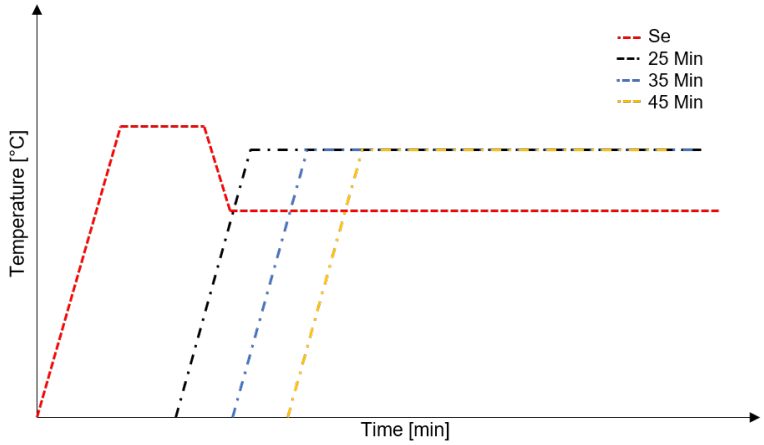

Figure B.2: Selenium and substrate heating profile. Different variations for starting the substrate heating; 25, 35, and 45 minutes after starting Se crucible heating.

Figure B.3 shows the LIV and DIV results from the reference and different heating profiles samples. It can be observed, that the reference sample shows a much higher FF and V_{OC} when compared to the PDT treated samples. On average, the FF for the reference sample is 64.6%, while the 25, 35, and 45 minutes report 61.2%, 63.6%, and 63.5% respectively. Comparing the V_{OC}, the reference sample shows almost 50 mV higher average V_{OC}. This directly correlates with the recombination current J_0, which is also lower for the reference sample. However, when comparing the diode ideality factor (n1), series, and shunt resistance of the different samples, it can be noted that the PDT treated samples with heating profiles of 35 and 45 minutes show improved parameters with respect to the reference sample.

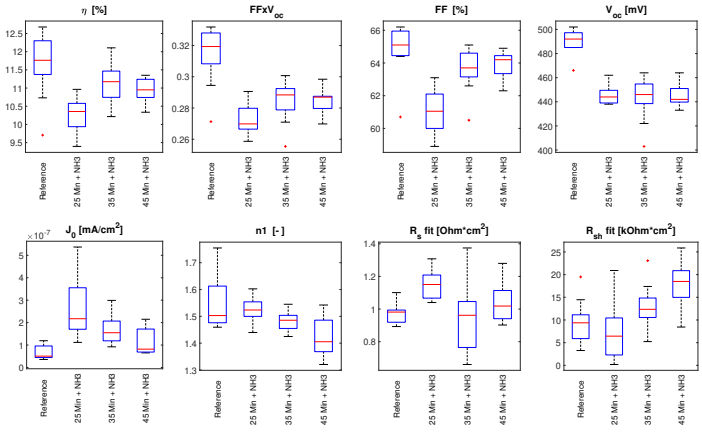

Figure B.3: LIV and DIV parameters Se experiment closed shutters.

In addition to the electrical characterization, the compositional characterization of the samples before and after the PDT can be found in Figure B.4. The maps show big non-uniformity in the CGI composition, where quadrant 2 (top left, 25 minutes) exhibits a higher intensity of the CGI. In contrast, the remaining 3 quadrants top right (reference), bottom left (35 minutes) and bottom right (45 minutes) show a similar CGI concentration before the PDT. Likewise, after finishing the PDT all the quadrants exhibit a decrease in the CGI concentration, but the nonuniformity is still present.

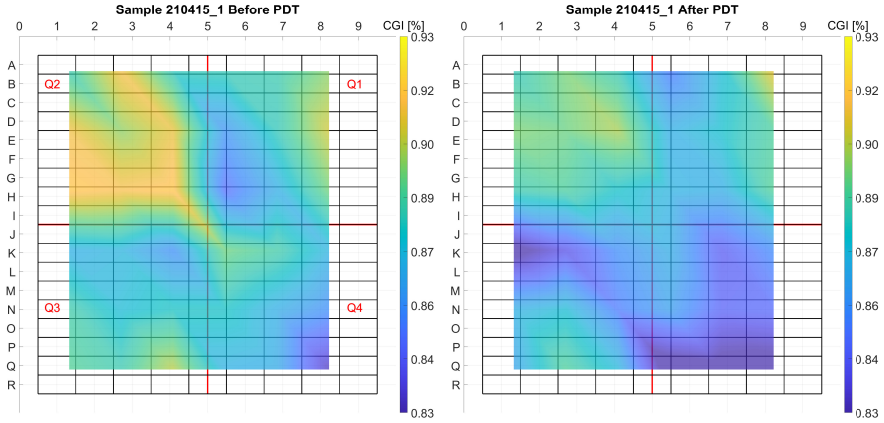

Figure B.4: XRF results **Left.** Before, and **Right.** After PDT.

Furthermore, with the use of Raman spectroscopy, it is possible to observe the different phases and extract important characteristics such as peaks location, intensity, and width to correlate them with the different CGI concentrations observed in the XRF maps. In Table B.2 and Figure B.5 the characteristics and spectra of eight cells with different CGI concentrations from each sample can be observed.

Table B.2: Raman selected cells with different CGI concentrations. Fitted CIGS A1 peak location and width. Se experiment closed shutter.

Sample	Cell	CGI	CIGS A1 peak location [cm-1]	CIGS A1 peak width [cm-1]	OVC [Yes/No]	GOF
Referemce	H7	0.87	174	4	N	0.991
Referemce	H9	0.89	174	4	N	0.994
25 Min	E2	0.90	174	5	N	0.989
25 Min	E4	0.91	174	4	N	0.990
35 Min	K4	0.86	174	5	Y	0.969
35 Min	O4	0.88	174	4	Y	0.989
45 Min	K6	0.89	174	4	Y	0.992
45 Min	R8	0.87	174	5	Y	0.982

The results show that for 35 and 45 minute samples, with lower CGI concentration (CGI<0.9), a clear OVC peak in the region of 150-160 cm^{-1} appears. Conversely, and despite showing lower CGI concentration, the reference sample does not show the presence of this peak. This suggests that a Cu depletion is created mainly in the surface of the absorber with the implementation of the Rb PDT, reported previously [2] [3]. On the other hand, the 25 minute sample that contains the higher CGI concentration does not show the presence of the OVC peak, probably due to the extremely high Cu concentration present in the sample before the PDT.

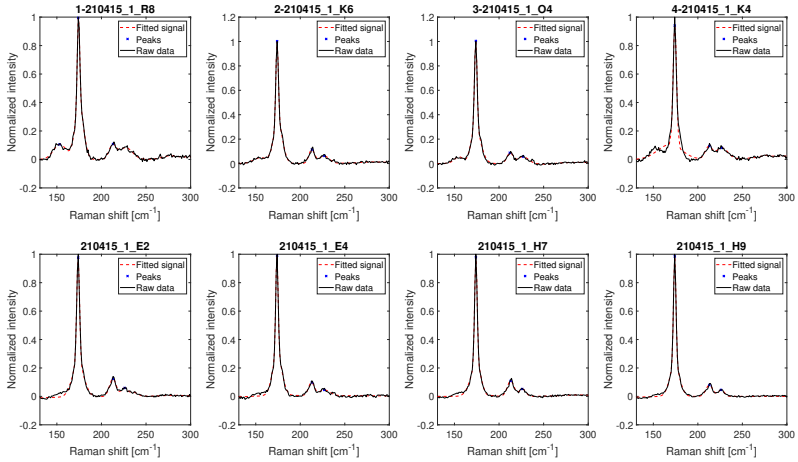

Figure B.5: Raman spectra Se experiment closed shutters, 8 cells with different CGI.

SUBSTRATE SHUTTER OPEN

As discussed in the first part of Section B.1.1, the Se atmosphere proves to be highly relevant for the optimization of the RbF PDT. In an attempt to improve the performance and prevent desportion of Se from the samples, a new experiment was performed. In this variation, the main key is to open the substrate shutter when this one reaches 280°C and thus, allow direct interaction between Se flux and the substrate.

Taking into account the results from the Section B.1.1, the Se atmosphere was only be performed for 35 and 45 minutes. In addition, for the bottom quadrants with similar CGI composition, a variation in the cleaning procedure before the experiment was implemented. Table B.3 shows a detailed description of the preparation of the four different samples, the PDT is performed with the same parameters as described in Table B.1.

Table B.3: Substrate heating times for optimum Se atmosphere, open shutter.

Sample	Se crucible start time [min]	Substrate heating start time [min]	Rinsing prior PDT
1	-	-	Reference
2	0	45	NH_3 [2%]
3	0	35	No
4	0	35	NH_3 [2%]

Figure B.6 presents the LIV and DIV curves for the four different samples. The main difference lies in the DIV curves, where a clear rollover is present at 0.6V for the sample without rinsing with ammonia prior to the PDT. This can indicate the presence of a defect at the interface of one of the multiple layers. Considering that none of the other samples show this behavior, the non rinsed and thus oxidized layer of the CIGS absorber might be creating this barrier and not allowing for the proper deposition of the RbF PDT. As a consequence, rinsing of samples that have been exposed to air prior to the PDT is a key aspect to consider (discussed in Section B.1.2).

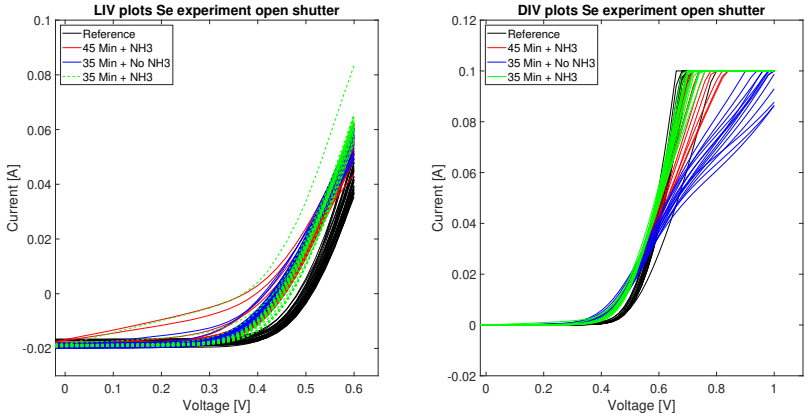

Figure B.6: LIV and DIV curves of the different samples, of the Se experiment with open shutter.

Now, inspecting the LIV and DIV parameters of PDT rinsed samples, shown in Figure B.7 a slight improvement can be observed on the V_{OC}, n1 and J_0 when compared to the results with closed shutters (Section B.1.1). Remarkably, FF for the sample with rinsing and 35 minutes show an evidently increased performance, and thus probably the combination of this procedure together with an improved rinsing might result in better electrical parameters (discussed in Section B.1.2).

Similar to the previous experiment with closed shutters, an evident Cu depletion is observed in the XRF maps (Figure B.8), but this time a stronger depletion is observed especially in quadrant 4, which is the bottom right quadrant. This can be detected in the Raman spectra of selected cells from the different samples, where the intensity of the OVC peak is higher when compared to the sample with closed shutters.

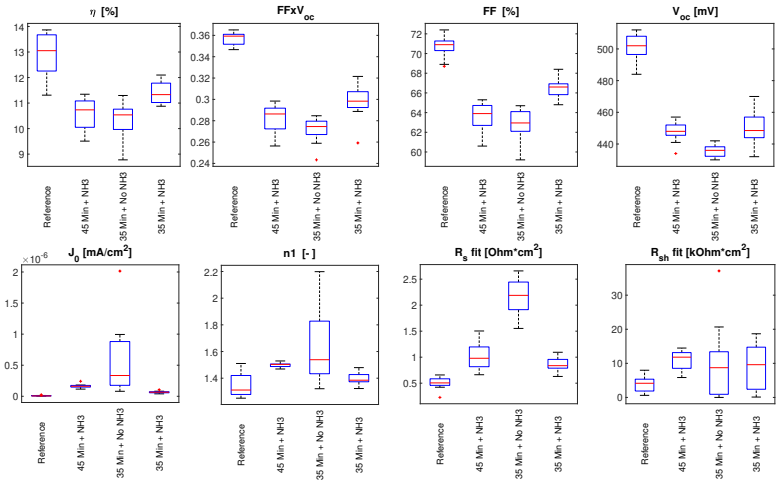

Figure B.7: LIV and DIV parameters Se experiment open shutters.

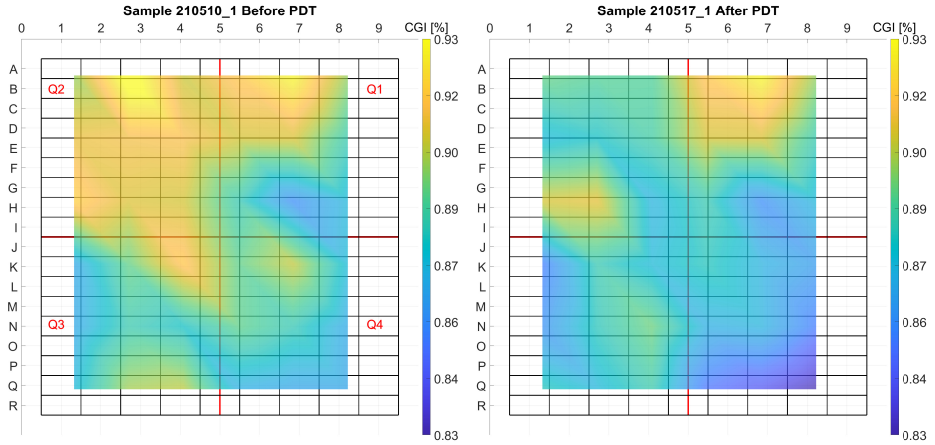

Figure B.8: XRF results **Left.** before, **Right.** after PDT. Open shutter.

Table B.4 and Figure B.9 show the results of 8 selected cells with different CGI concentrations. In parallel to the sample with closed shutters, the location of the CIGS A1 peak did not change since the Ga concentration was kept the same in both samples. However, the width of the A1 peak which can be correlated with the Cu concentration, increased by 1 cm^{-1}, indicating that a stronger Cu depletion is created in the surface of the absorber and thus, a higher intensity for the OVC peak can be observed on cells M6, and Q1. Whereas, cells N4 and Q8 do not show the increase in the width of the A1 mode but still show a clear OVC but with lower intensity. Lastly, cells B6 and H7 do not show

the presence of the OVC thanks to the higher initial CGI concentration before starting the PDT.

Table B.4: Raman selected cells with different CGI concentrations. Fitted CIGS A1 peak location and width. Se experiment open shutter.

Sample	Cell	CGI	CIGS A1 peak location [cm-1]	CIGS A1 peak width [cm-1]	OVC [Yes/No]	GOF
45 Min + NH_3 [2%]	D3	0.91	174	4	N	0.986
45 Min + NH_3 [2%]	H2	0.91	174	4	N	0.985
Reference	B6	0.92	174	4	N	0.985
Reference	H7	0.86	174	4	N	0.994
35 Min + no NH_3	N4	0.88	174	4	Y	0.985
35 Min + no NH_3	Q1	0.87	174	5	Y	0.973
35 Min + NH_3 [2%]	Q8	0.87	174	4	Y	0.988
35 Min + NH_3 [2%]	M6	0.89	174	5	Y	0.982

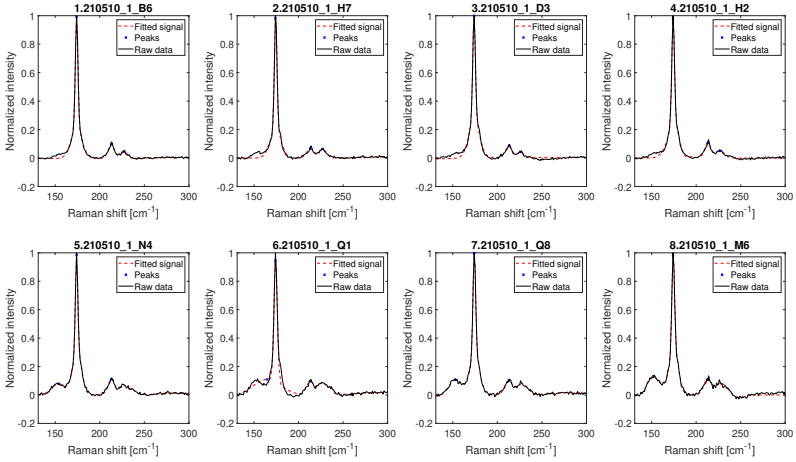

Figure B.9: Raman spectra Se experiment open shutters, 8 cells with different CGI.

With the series of experiments performed to identify the optimum Se atmosphere, two important conclusions can be established. On one hand, the electrical parameters such as V_{OC}, J_0, n1, and FF are heavily affected by exposing the samples to air prior to the PDT. Thus, the Se atmosphere inside the chamber and rinsing procedure prior starting the PDT play an important role to prevent the degradation of these parameters. In order to prevent this, the Se source must be turned on 35 minutes in advance to create the optimum Se atmosphere inside the chamber. Moreover, opening the substrate shutter and enabling the direct interaction between the flux of Se and the substrate is crucial when the substrate temperature is above 280°C.

On the other hand, the identification of an optimum rinsing procedure prior to the PDT is important, since the performance of the PDT samples without rinsing shows a clear barrier seen as a rollover in the dark IV curves. This barrier can be created after the PDT is deposited on the samples or directly after exposing the samples to air.

B.1.2. CLEANING PROCEDURE BEFORE STARING PDT

RINSING of the samples that have been exposed to air, prior to the PDT proves to be critical to obtain good performance. In particular, parameters like FF, V_{OC} are greatly reduced and, J_0 increased. This can be attributed to a degraded or oxidized top surface from the bare CIGS absorbers.

In literature, different rinsing procedures have been carried out with different chemicals to remove the undesired compounds that form on the surface of the CIGS [4]. Among the different chemicals, for simplicity and reproducibility, 4 different chemicals were used: potassium cyanide (KCN), ammonium sulfide (AS), and ammonia (NH_3) solution of 5% instead of the 2% solution used previously. When using KCN, AS and NH_3 5% the samples were dipped completely in the solution while for the NH_3 2% the samples were rinsed on the surface only. After finishing the samples rinsing with KCN and AS, they are cleaned using distilled water and blown dry with Nitrogen while NH_3 ones are only blown dry with Nitrogen.

The different variations for the cleaning procedure of air exposed absorbers prior to the PDT is depicted in Table B.5, sample number 2, and sample number 3 will show the direct effect of KCN etching on high CGI and low CGI samples respectively. Moreover, since AS shows lower etching rates compared to KCN, the etching time for AS is increased by 2 times [4] with respect to KCN.

Table B.5: Cleaning procedure air exposed absorbers prior PDT.

Sample	Se Curcible start time [min]	Substrate heating start time [Min]	Substrate shutter Open [Yes/No]	Rinsing prior PDT	Solution wt [%]	Rinsing time [min]
1	-	-	-	Ref	-	Ref
2	0	35	Yes	KCN	5	5
3	0	35	Yes	KCN	5	5
4	0	35	Yes	AS	20	10
5	0	35	Yes	NH_3	5	5
6	0	35	Yes	NH_3	5	2
7	0	35	Yes	NH_3	5	1

It is important to remark that samples five to seven have a different PDT variation. This variation was performed based on the best results obtained from samples that have not been exposed to air. Table B.6 show the variation of the PDT implemented for the samples etched with KCN and AS and the ones etched with NH_3.

Table B.6: PDT variations for rinsed air exposed absorbers.

Sample	PDT substrate temperature [C]	PDT source temperature [C]	Capping layer deposition time [min]	PDT duration [min]
2-4	350	565	1	6.5
5-7	360	565	2	6.5

Figure B.10 shows the electrical performance of air exposed absorbers under different rinsing procedures. Similar to the previous air exposed absorbers the V_{OC}, FF, and J_0 showed decreased performance when compared to the reference sample, this can be due to poor compatibility between CIGS and the RbF added layer on top of it. However, the compatibility between the added PDT layer and the buffer layer might be also responsible for the lower performance.

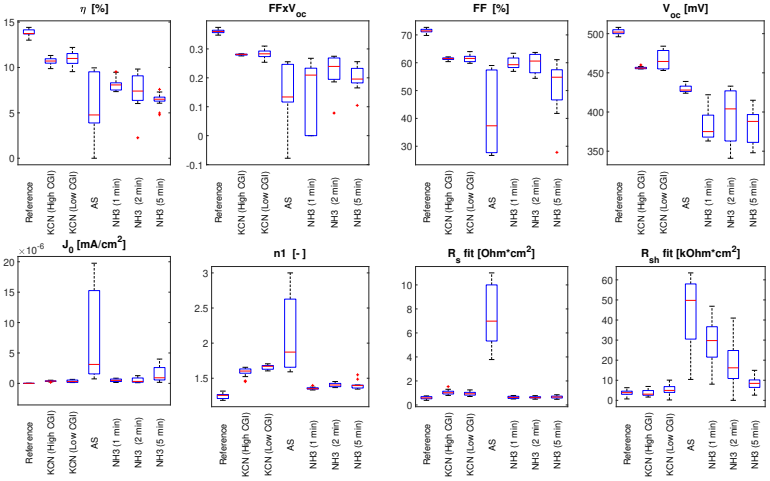

Figure B.10: Different rinsing procedures for air exposed absorbers.

Among the different rinsing techniques used to clean the samples, AS showed the worst results in FF and J_0. FF is decreased by almost 50% on average compared to the other samples and J_0 is increased by 2 orders of magnitude. This can be explained by the extremely low CGI observed on the XRF maps Figure B.13 and the presence of a barrier observed in the DIV curves Figure B.11. On the other side, samples rinsed with NH_3 show better J_0 and FF but the loss in V_{OC} compared to the reference sample is more than 100 mV. This loss in V_{OC} can be explained by the different PDT variations or incomplete coverage of the CdS buffer layer. It is important to remark that in contrast to the AS rinsed samples the NH_3 ones do not show the s-shape anomaly in the DIV curves (Figure B.12). Lastly, the performance of KCN etched samples despite the CGI of the sample show similar trends in all the electrical parameters along with the LIV and DIV curves being the closest to reference performance.

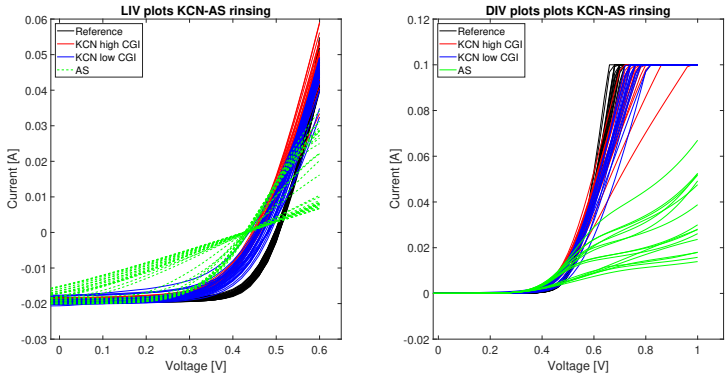

Figure B.11: LIV and DIV plots for the KCN and AS rinsed samples.

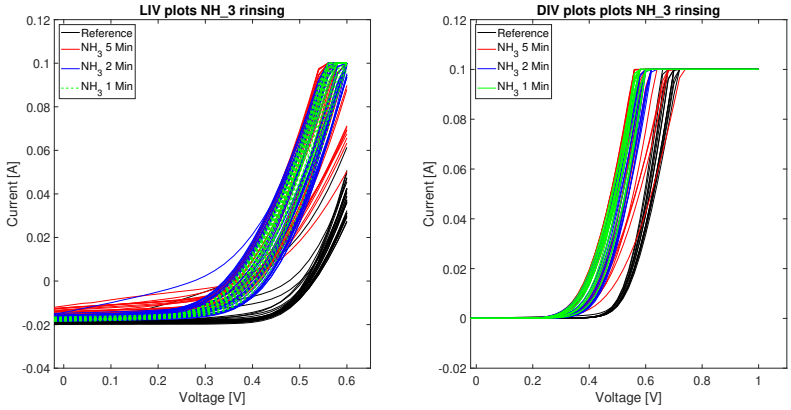

Figure B.12: LIV and DIV plots for the NH_3 rinsed samples.

Figures B.13 and B.14 show the CGI concentration before and after the PDT for the different rinsing procedures. It can be observed that the AS etched sample shows a large decrease in the CGI compared to the KCN and NH_3 ones. This might be related to the long exposure time to the chemical, nevertheless, sample number 4 show initially had a lower CGI concentration even before the PDT.

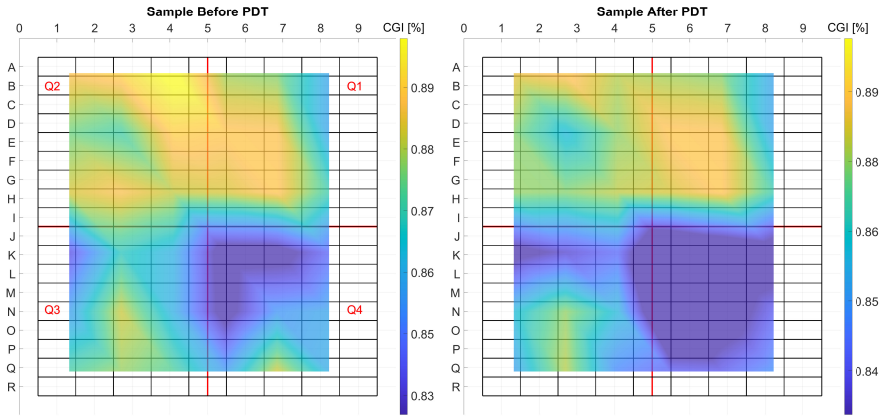

Figure B.13: XRF results **Left.** After, **Right.** Before PDT and KCN-AS etch.

On the contrary, samples etched with NH_3 (Figure B.14) show a much lower decrease in the CGI concentration. It is worth motioning that the substrate temperature and the capping layer thickness during the PDT for samples five to seven is different.

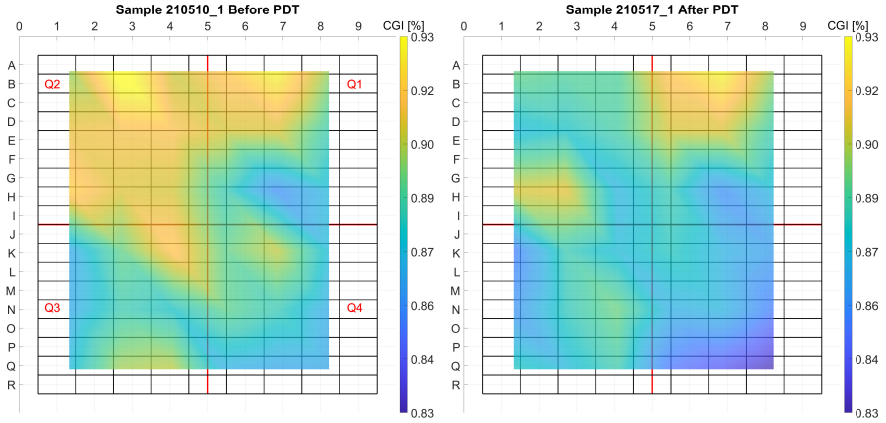

Figure B.14: XRF results **Left.** After, **Right.** Before PDT and NH_3 [5%] etch.

Figure B.15 and Table B.7 show the different Raman spectra for 8 cells with different CGI compositions. Similar to previous samples, the width of the CIGS A1 mode decreased for the lower CGI cells, and a clear OVC peak appear.

Table B.7: Raman selected cells with different CGI concentrations. Fitted CIGS A1 peak location and width. AS and KCN rinsed samples.

Sample	Cell	CGI	CIGS A1 peak location [cm-1]	CIGS A1 peak width [cm-1]	OVC [Yes/No]	GOF
Reference	E6	0.89	174	4	N	0.992
Reference	C9	0.85	174	4	N	0.993
KCN (High CGI)	D3	0.87	174	4	N	0.996
KCN (High CGI)	A1	0.89	174	4	N	0.995
KCN (Low CGI)	K2	0.87	174	4	Y	0.995
KCN (Low CGI)	K4	0.86	174	5	Y	0.994
AS	N7	0.85	174	5	Y	0.971
AS	Q8	0.88	174	5	Y	0.977

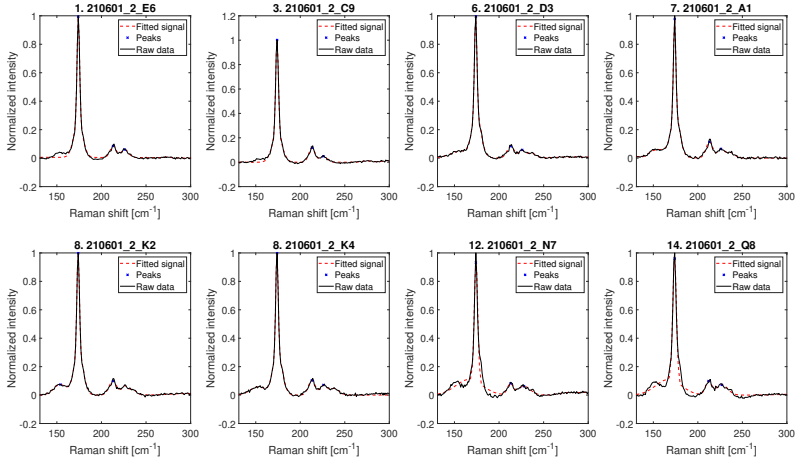

Figure B.15: Raman spectra KCN and AS rinsed samples.

In contrast to previous air exposed absorbers analyzed by Raman spectroscopy, the samples etched with NH_3 and with a different variation of the PDT (longer capping layer and higher substrate temperature for RbF deposition) showed intensities in the OVC three to four times to what it is observed in previous results. Figure B.16 and Table B.8 show that despite having a larger CGI concentration than KCN and AS etched samples the intensity of the OVC peak is sometimes on the same magnitude as the CIGS A1 mode.

Table B.8: Raman selected cells with different CGI concentrations. Fitted CIGS A1 peak location and width. NH_3 [5%] rinsed sample.

Sample	Cell	CGI	CIGS A1 peak location [cm-1]	CIGS A1 peak width [cm-1]	OVC [Yes/No]	GOF
Referemce	D8	0.91	174	4	N	0.993
Referemce	B6	0.92	174	4	N	0.996
5 Min NH_3	D3	0.92	174	5	Y	0.995
5 Min NH_3	A1	0.93	174	5	Y	0.994
2 Min NH_3	N3	0.88	174	5	Y	0.993
2 Min NH_3	Q4	0.89	174	4	Y	0.992
1 Min NH_3	N7	0.85	174	5	Y	0.993
1 Min NH_3	K6	0.83	174	5	Y	0.992

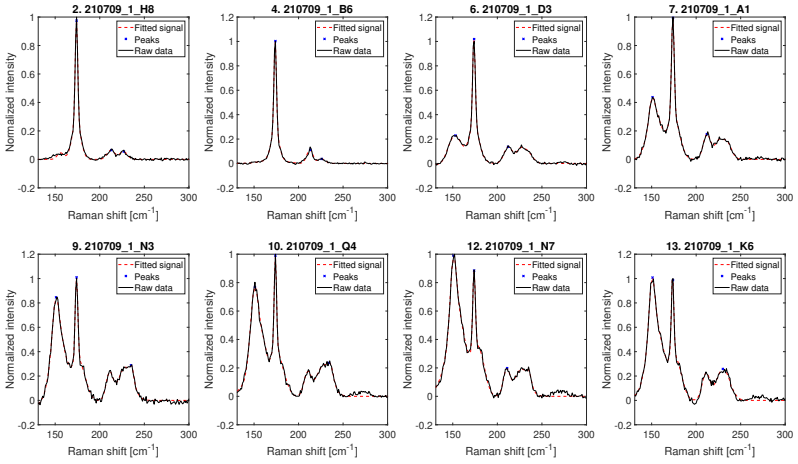

Figure B.16: Raman spectra, NH_3 rinsed sample.

B.2. CONCLUSIONS

AFTER the multiple experiments performed on exposed to air samples it was noticed that the Se atmosphere before starting the PDT can affect the FF of the solar cells when it is not present the FF is heavily reduced by almost 6-7%. Along with this, it can be concluded that the most important parameter to prevent the formation of barriers, observed as distortions in the IV curves is the rinsing of the samples prior starting the PDT. On one side, if a prolonged rinsing is performed (especially with AS) S-shapes appear in both dark and light IV measurements. On the other side, if no rinsing is performed S-shapes appear only in dark IV measurements suggesting that a possible barrier is still present at one of the front interfaces.

Furthermore, with the use of Raman spectroscopy the appearance of the OVC peak in the samples with PDT and CGI concentrations below 0.90 was identified. This indicates that a Cu depletion is been created by the implementation of the RbF PDT and the InSe capping layer. In some cases, this Cu depletion can also be observed as a widening in the CIGS A1 mode, probably suggesting a stronger Cu depletion in the surface and in the bulk. With the preceding internship, it has been observed that the OVC peak intensity can be reduced by tuning the substrate temperature during the deposition of the RbF. Nevertheless, this was performed on the sample etched with NH_3 [5%] and the intensity of the OVC peak increased considerably, however, this can be a consequence of the prolonged InSe capping layer deposited.

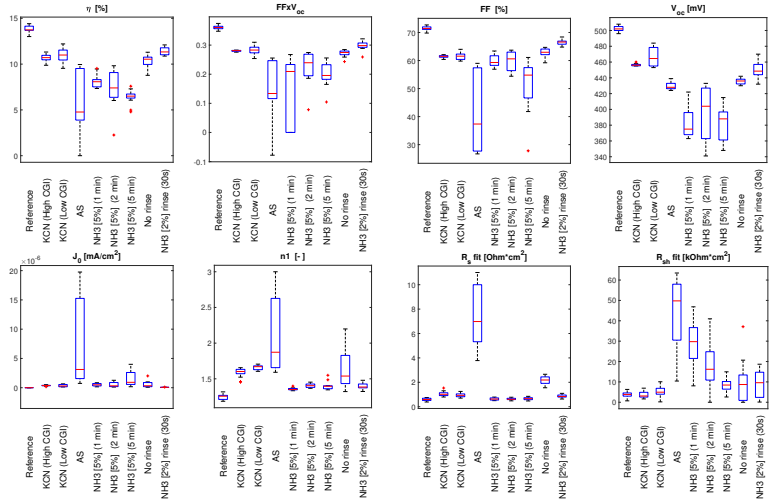

Figure B.17: Electrical performance of the different rinsing procedures implemented for air exposed absorbers. All samples have 35 min Se atmosphere before the PDT is started, and the shutter is open.

Noticing the low electrical performance of the samples when compared to the baseline (Figure B.17), regardless of the different preconditioning techniques performed on them, it was decided to stop the processing and switch to the development of the PDT on non-exposed to air samples.

REFERENCES

[1] M. Theelen, C. Foster, H. Steijvers, N. Barreau, Z. Vroon, and M. Zeman, *The impact of atmospheric species on the degradation of cigs solar cells,* Solar Energy Materials and Solar Cells **141**, 49 (2015).

[2] A. Vilalta-Clemente, M. Raghuwanshi, S. Duguay, C. Castro, E. Cadel, P. Pareige, P. Jackson, R. Wuerz, D. Hariskos, W. Witte, and et al., *Rubidium distribution at atomic scale in high efficient Cu(In,Ga)Se_2 thin-film solar cells,* Applied Physics Letters **112**, 103105 (2018).

[3] N. Maticiuc, T. Kodalle, B. Ümsür, T. Bertram, R. Wenisch, Y. Wang, I. Majumdar, H. A. Yetkin, D. Abou-Ras, N. Schäfer, C. A. Kaufmann, R. Schlatmann, and I. Lauermann, *Depth-resolved analysis of the effect of rbf post deposition treatment on cigse with two different cu concentrations,* Solar Energy Materials and Solar Cells **226**, 111071 (2021).

[4] M. Buffière, A.-A. E. Mel, N. Lenaers, G. Brammertz, A. E. Zaghi, M. Meuris, and J. Poortmans, *Surface cleaning and passivation using (nh4)2s treatment for cu(in,ga)se2 solar cells: A safe alternative to kcn,* Advanced Energy Materials **5**, 1401689 (2015), https://onlinelibrary.wiley.com/doi/pdf/10.1002/aenm.201401689 .

C

CORRELATION BETWEEN ELECTRICAL PARAMETERS AND MATERIAL COMPOSITION

To be able to understand and correlate the material properties of the solar cell with the electrical performance, various graphs were plotted from the different sets of experiments performed. It is important to point out that in the following graphs all the cells (good and bad performing) that were measured by Raman spectroscopy are shown, which explains the big spread in CGI and electrical parameters.

C.0.1. TEMPERATURE SERIES

Figure C.1 shows the correlation of the light IV parameters with the CGI and OVC peak intensity. Regarding V_{OC} and OVC intensity, a correlation of 0.56 between these parameters can be obtained, which can be observed in the graph where as the OVC intensity increases so does V_{OC}. On the other hand, FF and OVC show a negative correlation of -0.32, which is not as strong as the preceding one but can be slightly noticed on the graph. With respect to efficiency and OVC, the spread in the measured point is large and no correlation can be detected. Similarly, the non-uniformity in the CGI of the samples makes it difficult to correlate the electrical performance with the material properties, however, η tends to increase as the CGI of the samples increases, this explains the decision of going towards higher CGI content discussed on Section 4.3.2.

In the same way, the correlation of the DIV parameters with the CGI and OVC intensities is displayed in Figure C.2. Two relevant things can be observed, the first one is that the number of measured points is reduced, this is a result of the DIV measurements in which not all the cells are measured and some of the results are excluded. Alongside this, the spread of the points is big and no clear relationship can be established.

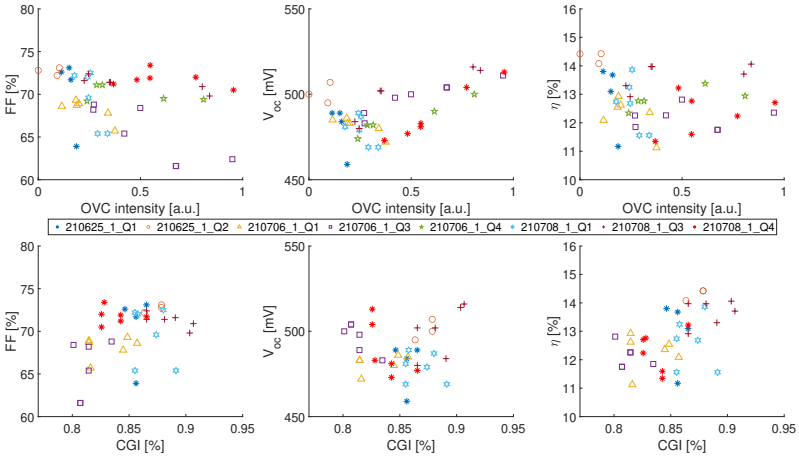

Figure C.1: Temperature series LIV electrical parameters correlation with material properties

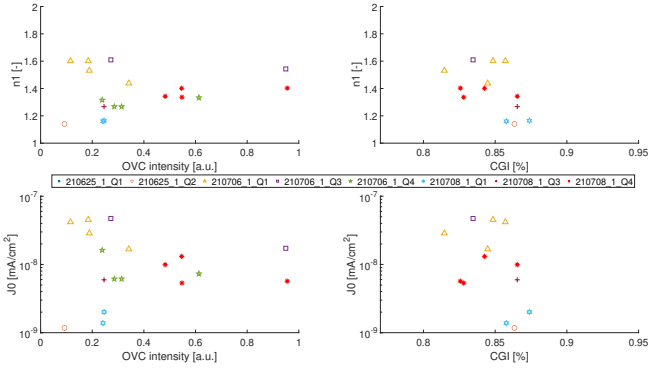

Figure C.2: Temperature series DIV electrical parameters correlation with material properties

C.0.2. CGI VARIATIONS

On Figure C.3 shows the different electrical parameters and material properties obtained for the high CGI sample. Remarkably, only one of the cells measured reveals the presence of OVC, this goes in accordance with what was expected after reducing the capping layer thickness and increasing the CGI of the sample.

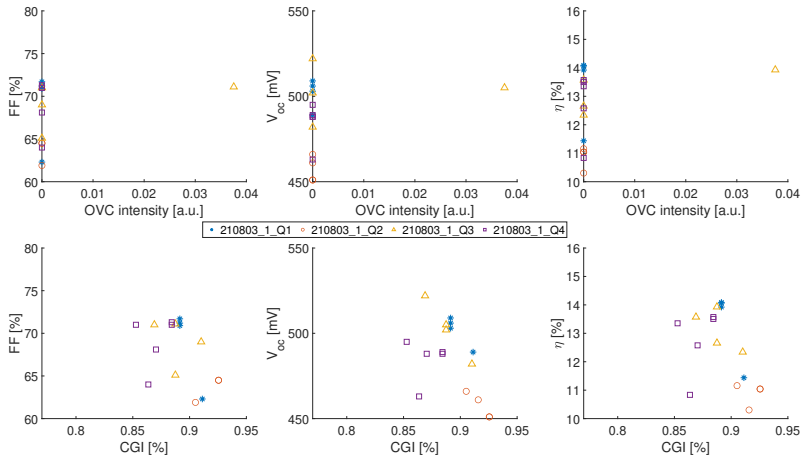

Figure C.3: CGI variation series LIV electrical parameters correlation with material properties

Clearly, no correlation can be established from the OVC intensities. But concerning the CGI, when it is greater than 0.90 the V_{OC} and FF of the samples is extremely reduced. This observation can be correlated whit the DIV parameters shown in Figure C.4, where the J_0 and n1 of the samples increase with CGI with a correlation coefficient of 0.40.

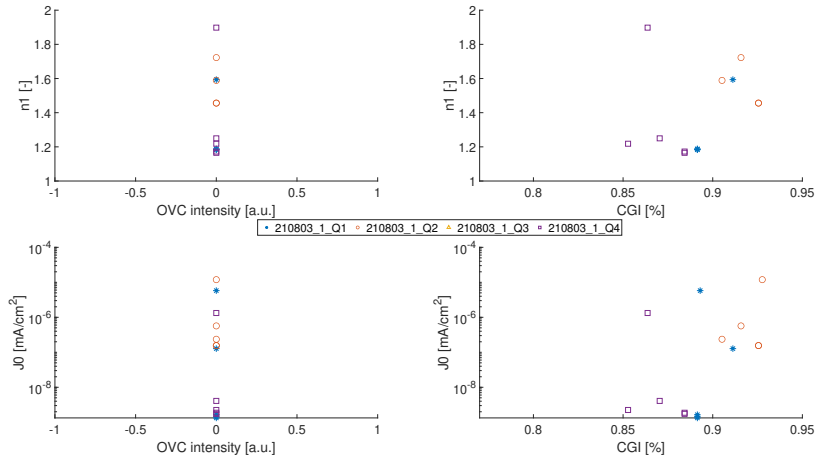

Figure C.4: CGI variation series DIV electrical parameters correlation with material properties

C.0.3. Buffer layer variations

The last set of samples analyzed is the buffer layer variation set, in which different rinsing techniques and CBD were implemented with the optimized variables of the

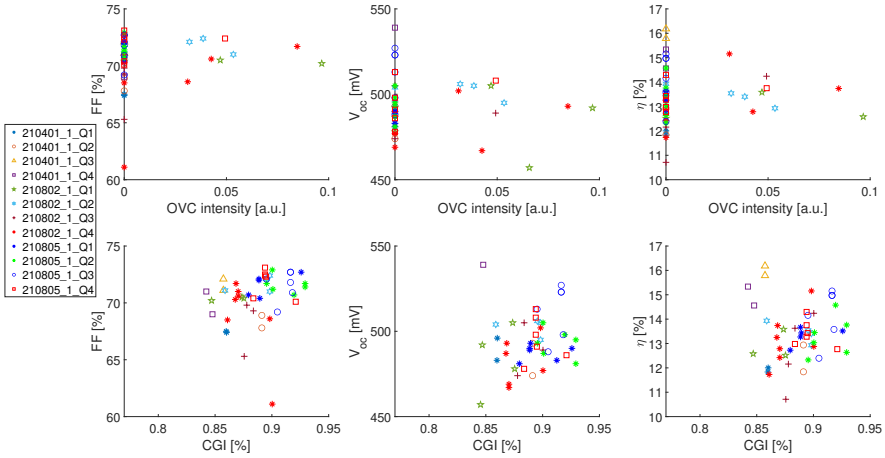

Figure C.5: Buffer layer variation series LIV electrical parameters correlation with material properties

PDT expecting to get the best performance. Figure C.5 shows the compilation of the results obtained, looking into the specified range for the CGI (0.85<0.90) the best cells are obtained (210401_1 Q3), displaying no OVC intensity and significantly better V_{OC} and FF. Close to these cells characteristics, sample 210805_1 Q3 with CGI above 0.90 and no OVC intensity exhibits even better FF but marginally lower V_{OC}, in the same manner, but with a CGI of 0.89, OVC intensity of 0.03 and thus smaller FF, yet similar V_{OC} sample 210802_1 Q2 demonstrate similar performance.

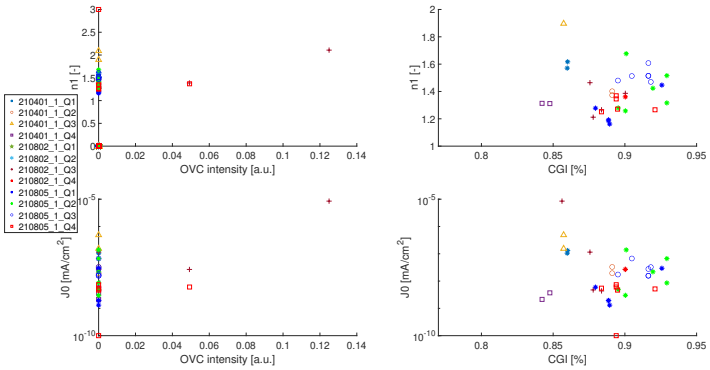

Figure C.6: Buffer layer variation series LIV electrical parameters correlation with material properties

Once again, thanks to the big spread in the data and the insufficient data points in the DIV data, in Figure C.6 no correlation can be established between the DIV parameters and material properties.

D

RAMAN BASELINE SUBTRACTION AND FITTING PROCEDURE

D.1. RAMAN BASELINE REMOVAL

To remove the baseline from the spectrum obtained, MATLAB software is used. To do so, an n-degree polynomial spline is calculated by interpolating selected points on the spectrum. The advantage of this method is that n points can be selected on the spectrum to get the most accurate fitting result. First, as it can be seen in Figure D.1 left, the software makes it possible to select the different points with the cursor, then based on the selected points a spline is calculated (red). The final spectrum (blue) is the difference between the original spectrum signal and the spline line, as it can be seen in Figure D.1 right. As an example, Figures D.2 left and right shows different results that can be obtained by varying the number of selected points on the reference spectrum.

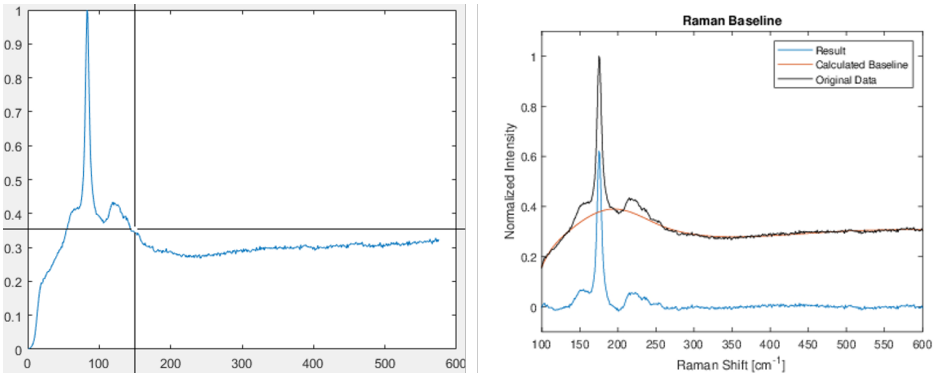

Figure D.1: **Left.** Point selection for line interpolation. **Right.** Result with the calculated baseline

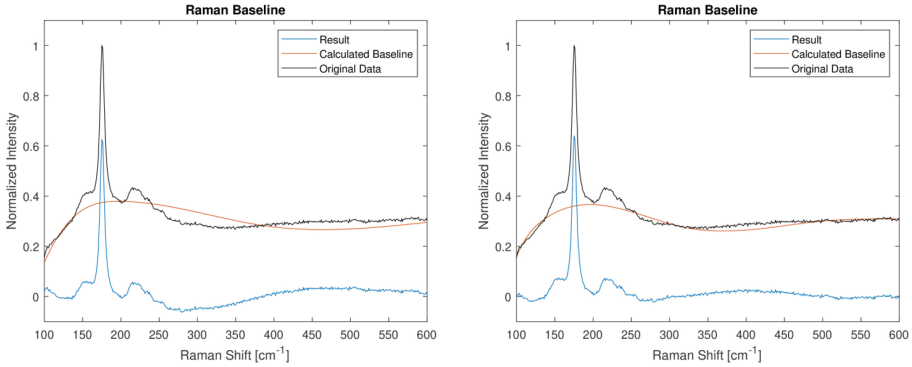

Figure D.2: **Left.** Raman baseline result using 4 and **Right.** 6 points

D.2. RAMAN FITTING PROCEDURE

Once the baseline is subtracted from the reference spectrum, the results are fitted into an eight term Gauss model. By making this, it is possible to identify and calculate easier the location, area, height, and width of the peaks at half maximum height. Figure D.3, compare multiple Gaussian models with the different number of terms. Distinctly,

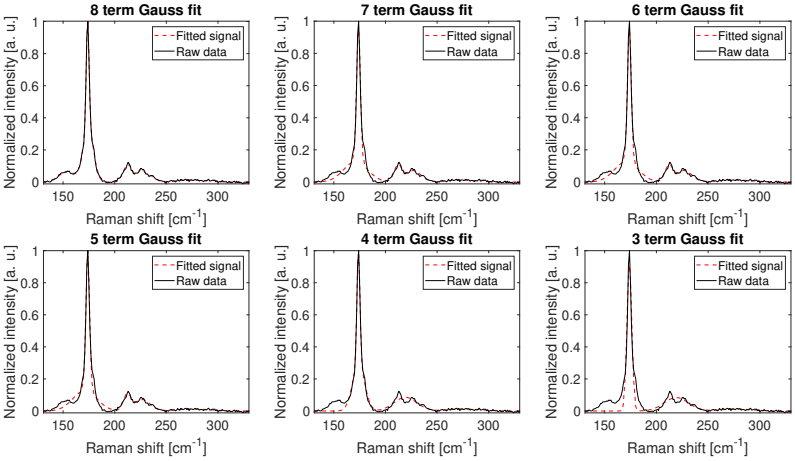

Figure D.3: Different Gauss fitting for Raman results

seven and eight terms fitting show the most accurate results but if 7 terms are used the OVC peak is not clearly detected by the 7-term fit, in contrast with the 8-term model all the peaks are clearly identified. In Table D.1, different values of the R-square are shown changing the number of Gaussian terms used to fit the Raman spectra. Assessing this parameter, it can be inferred that the 8 terms Gauss fitting shows the best fitting among the others.

Table D.1: Goodness of fit for different Gauss fitting terms equation.

Number of terms Gauss fitting	Goodness of fit
3	0.929
4	0.971
5	0.973
6	0.974
7	0.974
8	0.988

E

VARIABLE IRRADIANCE MEASUREMENTS DATA PROCESSING

E.1. VIM V_{OC} LOSS QUANTIFICATION

One approach to investigate the loss in V_{OC} created by the barrier is to calculate the pseudo IV curve in which the effect of the series resistance is neglected. This can be done by comparing the DIV curve of the solar cell and LIV curve recreated with the V_{OC} and J_{SC} with the different irradiance levels. The deviation of the reconstructed curve from the DIV curve at 1000W/m^2 can give an approximate quantification of the voltage loss. In order to do this, the J_{SC} obtained at 1000 Wm^{-2} is interpolated linearly using the data of the DIV curve to extract the ideal V_{OC} of the solar cell. Once this value is obtained, the difference between the calculated value and the V_{OC} at 1000 Wm^{-2} is performed. Figure E.1 shows with an arrow the approximate loss observed in one reference cell.

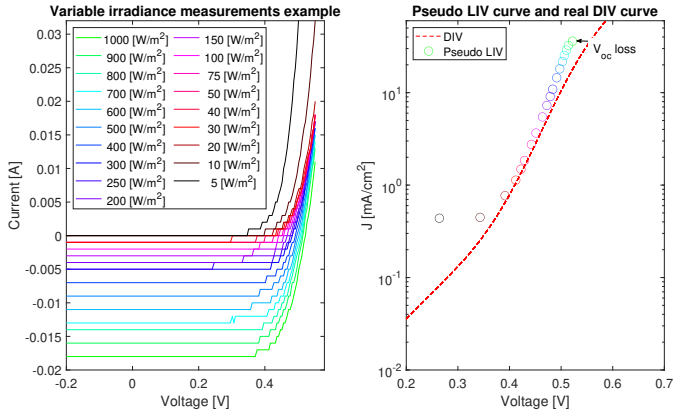

Figure E.1: Left. Different IV curves were obtained for different irradiance levels. Right. DIV-Pseudo LIV curve comparison.

E.2. VIM FF SLOPE QUANTIFICATION

As discussed in Chapter 4.3.1 and 4.3.3, it was observed that the PDT solar cells show a slight decrease in FF when exposed to higher irradiance levels. In order to assess this FF decrease quantitatively, the values were fitted to a linear model. The slope and the R-squared values of the fitted equation were calculated to evaluate the goodness of the fit (GOF) and select the best fitting range.

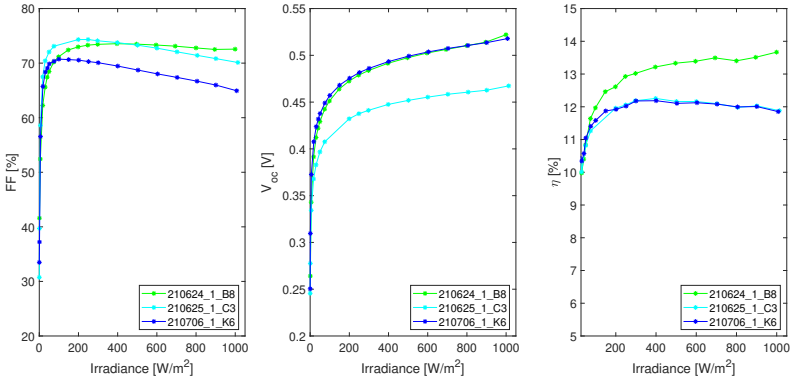

Figure E.2: FF dependence on the irradiance level example.

Table E.1: Results of the fitted cells.

Fitted range/ Name	400-1000 [Wm^{-2}]		200-1000 [Wm^{-2}]		300-1000 [Wm^{-2}]	
	Slope [a. u.]	GOF	Slope [a. u.]	GOF	Slope [a. u.]	GOF
210624_1_B8	-1.94×10^{-3}	95.2	-9.9×10^{-4}	53.4	-1.63×10^{-3}	89.1
210805_1_C3	-6.03×10^{-3}	99.8	-5.31×10^{-3}	98.5	-5.72×10^{-3}	99.2
210706_1_K6	-7.24×10^{-4}	99.6	-6.84×10^{-3}	99.5	-7.11×10^{-3}	99.6

Figure E.2 shows the variation of the FF, V_{OC} and η with the irradiance level. It can be observed that the FF and V_{OC} show a linear trend between 200 and 1000 Wm^{-2}. Consequently, a first degree polynomial is fitted with the use of MATLAB. In case the GOF is below 90% the cell is excluded and not fitted. Table E.1, shows the different slopes and GOF values obtained for some cells changing the range of the fitting. After evaluation, it was concluded that the best range to perform the fitting is between 400-1000 Wm^{-2}.

F

CAPPING LAYER THICKNESS

To be able to establish the optimum capping layer substrate temperature and thickness, first, a characterization of it was performed. During this characterization, In and Se were co-evaporated in a Mo substrate at a temperature 380°Cfor a period of 10 minutes. Afterward, with the use of a profilometer, the thickness of the evaporated layer was measured. Figure F.1 shows the evaporated layer on the sample, and figure F.2 shows the thickness profile of the six different measurement points. The first step, present before 50µm corresponds to the edge of the capping layer (Figure F.1, right), therefore, the average thickness calculated corresponds to the points that are present right after the second step.

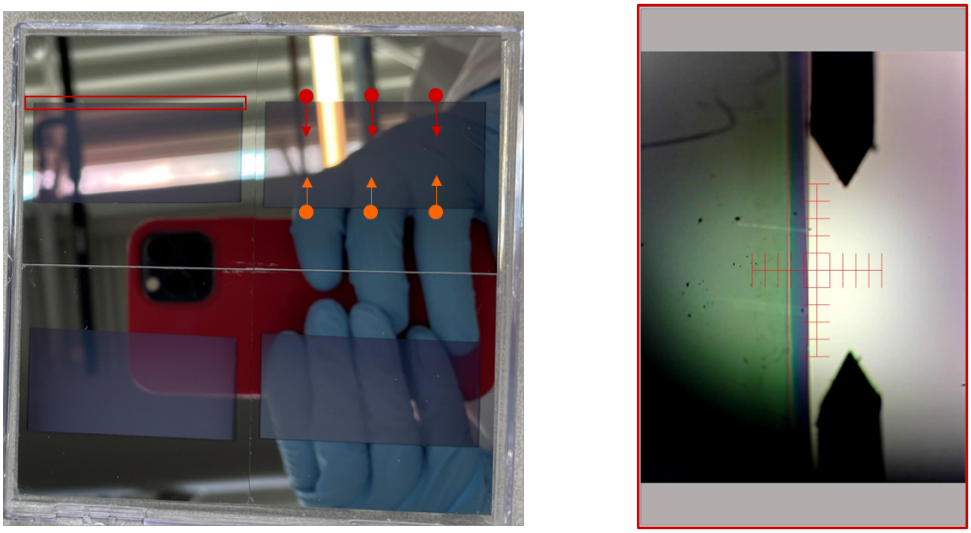

Figure F.1: InSe capping layer on Mo substrate. **Left** 4 quadrants evaporated InSe layer, with the 6 different measurement points. **Right** close up with the profilometer to the edge of the layer, edge step.

After analyzing the results, the deposition rate was calculated based on the average thickness obtained for each of the quadrants. Table F.1 shows that on average the deposition rate is uniform for all the quadrants and on average 24nm of InSe are deposited per minute.

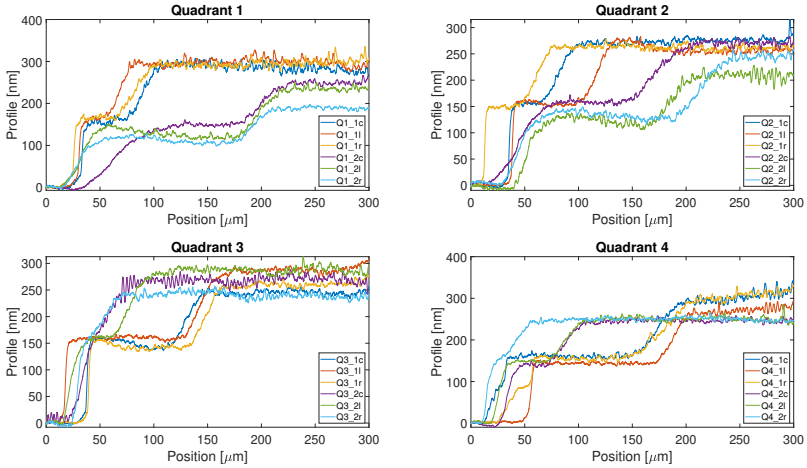

Figure F.2: Capping layer thickness on the 4 different quadrants.

Table F.1: Average capping layer thickness.

Quadrant	Average Thickness [nm]	Deposition rate [nm/min]
1	238.9	23.8
2	230.27	23
3	255.43	25.5
4	245.62	24.6

G

RbF DEPOSITION RATE CALIBRATION

BASED on the literature review and partners suggestions, the optimum amount of Rb that needs to be deposited in the sample is 12.6nm. This is achieved using a deposition rate of 0.074 Å/s at a temperature of 565°C. Intending to optimize the Rb incorporation to the surface of the sample and as suggested by the literature, 2 different deposition rates were implemented, 0.074 Å/s and 0.05 Å/s for either 6.5 or 10 minutes deposition respectively.

To be able to deposit the optimum amount of Rb, a characterization of the deposition rate of RbF at different temperatures was performed. Table G.1 shows the different variations of temperatures used and the estimated deposition rate. The deposition rate is calculated by using a quartz microbalance crystal (QCM) that is present on the inside left of the tool.

Table G.1: RbF deposition rates at different temperatures. *The deposition rate was not stable at this temperature, fluctuating constantly between the reported values, probably thanks to the PID controller.

RbF Temperature [°C]	**Deposition rate [Å/s]**
565	**0.074**
560	0.06
555	0.051
554	**0.05**
553.7	0.044-0.046*
553	0.046
552	0.04

H

XRF MAPS OF THE DIFFERENT SAMPLES

The non-uniformity present in the composition of the absorbers can be observed in the multiple XRF maps shown below. This nonuniformity is present in all Solliance co-evaporation samples and it develops mainly on the top right quadrant (Q2), where the composition of CGI is higher compared to the remaining quadrants. Figure H.1shows the non-uniformity especially for the CGI of the sample, in which the Cu is the cause of the big non-uniformity for the CGI of the samples (Figure H.2). Typically, the CGI of the baseline samples is between 0.87 and 0.89.

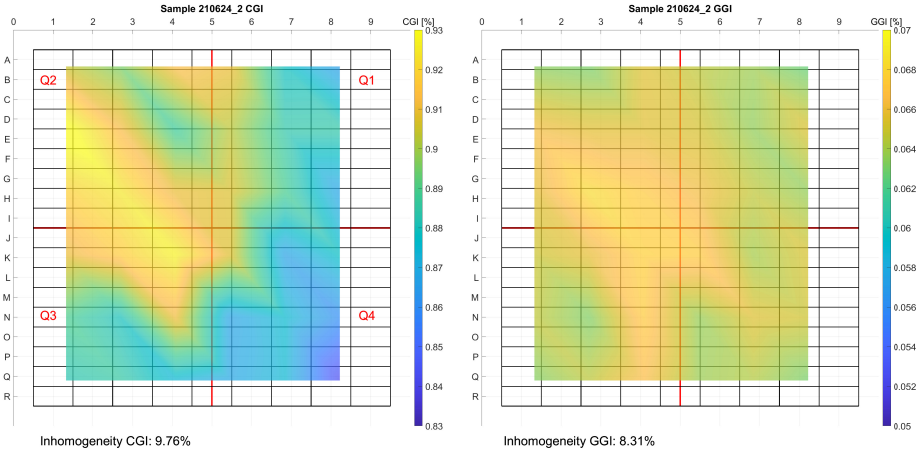

Figure H.1: XRF map reference sample.

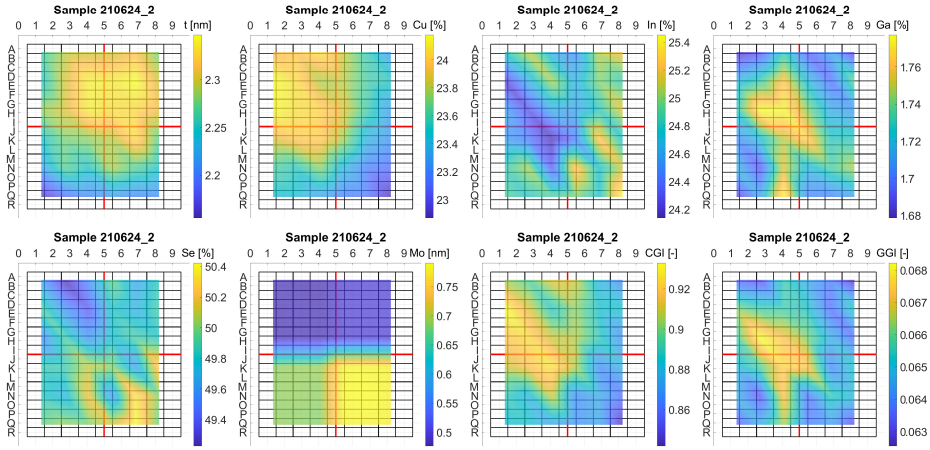

Figure H.2: XRF reported material concentrations for the reference sample

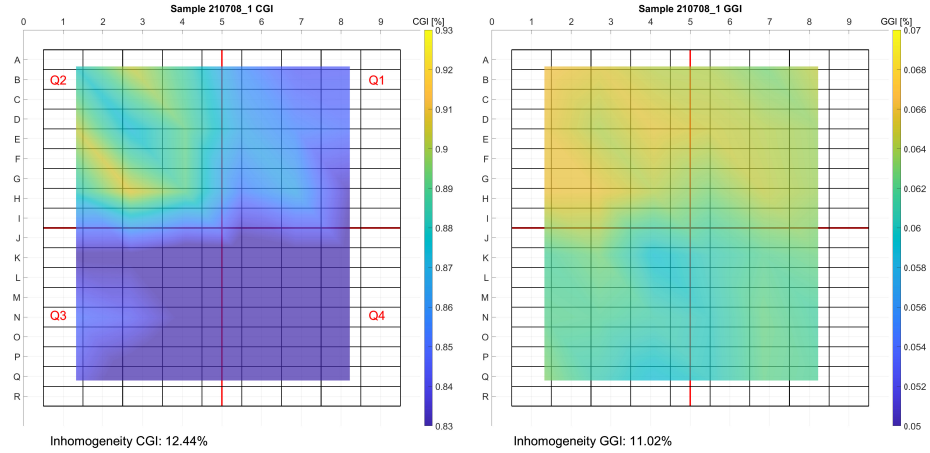

Figure H.3: XRF map 340°C sample.

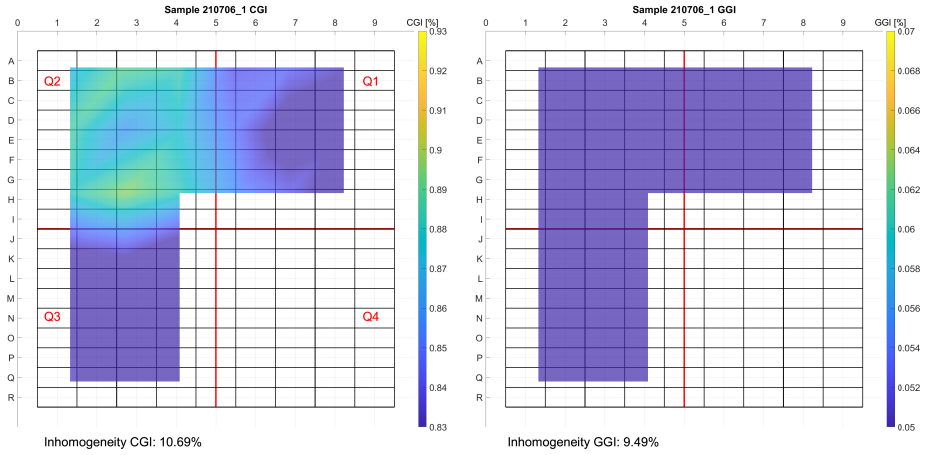

Figure H.4: XRF map 350°C sample. (Quadrant 4 XRF data was not measured, sample processing mistake)

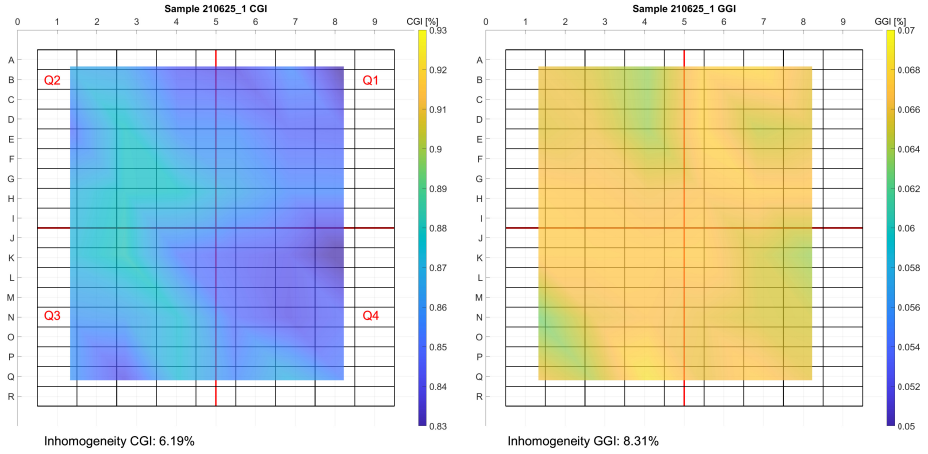

Figure H.5: XRF map 360°C sample.

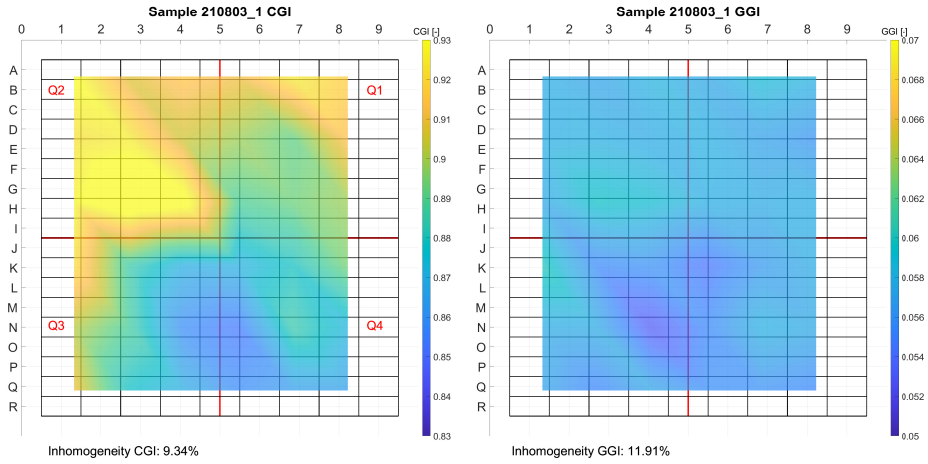

Figure H.6: XRF CGI maps capping layer variations

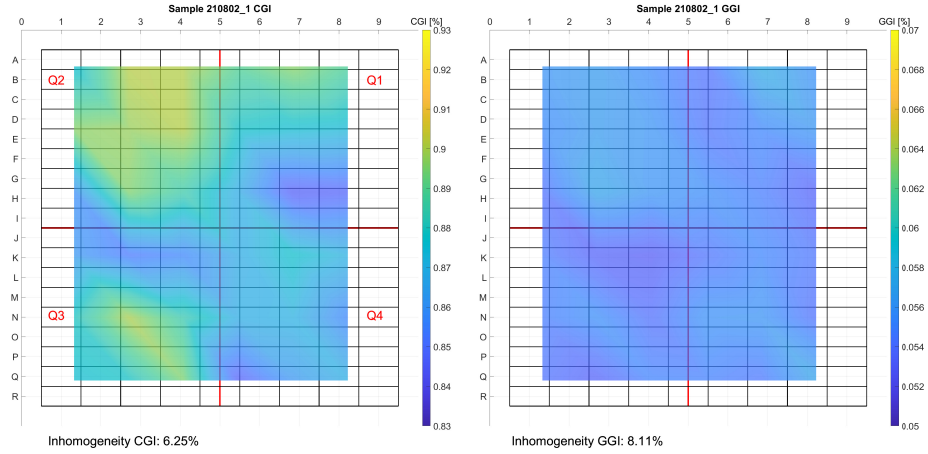

Figure H.7: XRF map, buffer layer variations. Q1 and Q2 NH_3 (Wet), Q3 and Q4 NH_3+N_2